

Experimental Characterization of Sample Tubing Dynamics for the Improvement of Droplet Microfluidic Feedback Control Systems

by

Dylan Hahn

A thesis
presented to the University of Waterloo
in fulfillment of the
thesis requirement for the degree of
Master of Applied Science
in
Mechanical and Mechatronics Engineering

Waterloo, Ontario, Canada, 2024

© Dylan Hahn 2024

Author's Declaration

I hereby declare that I am the sole author of this thesis. This is a true copy of the thesis, including any required final revisions, as accepted by my examiners.

I understand that my thesis may be made electronically available to the public.

Abstract

This thesis presents the development of an experimental methodology to characterize pressure transient dynamics across liquid sample tubing in the plant of a pressure-driven droplet microfluidic feedback control system (PDMFCS). To progress the PDMFCS towards being a widely adopted fluidic analysis tool for non-expert end-users in various biochemical fields, i.e. progressing the PDMFCS towards modularity, will require utilization of an accurate plant model to establish informed and robust control system design procedures. Increased accuracy in the plant model can be obtained through development of experimental methods to characterize the dynamics associated with the plant components. Previous PDMFCS implementations have approximated the sample tubing dynamics using a hydrodynamic equivalent circuit model (HECM), but did not experimentally validate this model. As well, pressure transient studies performed for other fluid applications do not model a flow scenario physically similar to that occurring through the sample tubing during PDMFCS operation, further justifying the need for this present study.

Pressure transient dynamics across the sample tubing of the PDMFCS plant were found to be characterized as an approximately linear first-order system with transport lag through estimation of a transfer function (TF), with 95% confidence in uncertainty in the estimated parameters, from an experimental frequency response obtained by simultaneously measuring pressure waves at the inlet and outlet of the sample tubing. Decreasing the average inlet pressure, increasing the tubing length to inner diameter ratio, or increasing the fluid viscosity, resulted in a decrease of the corner frequency (an increase in the time constant) of the frequency (step) response of the experimentally estimated TF. Comparing experimentally estimated TF dynamics to those predicted by the HECM showed that, due to the assumption of hydrodynamic steady-state flow inherent to its derivation, the HECM fails to quantitatively approximate the pressure transient dynamics across the sample tubing. The primary conclusion of this study is that the experimentally estimated TF should be used, instead of the HECM, to approximate the sample tubing dynamics within the PDMFCS plant model. Using the experimentally estimated TF to approximate the pressure transient dynamics across the sample tubing should improve the plant model accuracy, such that informed and robust control system design methodologies can be developed for the PDMFCS, which will enhance the modular potential of the system.

Acknowledgements

Firstly, I would like to thank my two supervisors Prof. Carolyn Ren and Prof. Kaan Erkorkmaz, whose kindness, guidance, and support must not go unnoticed. Dr. Ren, you gave me the trust and support necessary to enhance my research skills, and for that I will be forever thankful. Dr. Erkorkmaz, our discussions both advanced my ability to critically evaluate my work and widened my perspective on research, for this I am grateful.

I would also like to thank all of my fellow lab members, past and present. Without the work of David Wong and Marie Hébert, the foundation from which my research was developed would not exist. Kevin Chen, Noura Ezzo, and Weijia Cui were more than supportive in familiarizing me with the lab and the various procedures, while also providing an avenue for fun and interesting conversations. Alice Mao, Oscar Manuel Carreno-Molina, Alex Kropp, Andrew Katz, Katie DiCola, Yiqi Zhang, Maziar ShafieiDarabi, Nikhil Venkata Giri, Matt Courtney, Run Ze Gao, Jun Li, and Fong Chenananporn, thank you for providing me an outlet to discuss things both unrelated and related to research. Sujith Santharuban, thank you for being a great co-op student and assisting in running the model simulations for this work.

Ryley, Adam, and Cedric, I am happy we got to experience this part of our lives together. In time, I probably will not remember the specifics of my research, but I will definitely remember the food, late nights, camping trips, and joy shared with you three. So, thank you for making this a time I will look back on fondly.

Most importantly, I must thank my parents and Lauryn. Without your love, support, and encouragement, I would not be who or where I am today.

Last, but certainly not least, I must also thank Hazy for keeping me company during the writing process.

Dedication

For Mom and Dad,
until the next one, maybe.

Table of Contents

Author's Declaration	ii
Abstract	iii
Acknowledgements	iv
Dedication	v
List of Figures	x
List of Tables	xvii
List of Abbreviations	xix
List of Symbols	xx
1 Introduction	1
1.1 Background and Motivation	1
1.1.1 Essence of Microfluidics	1
1.1.2 Droplet Microfluidics	3
1.1.3 Droplet Control Strategies	4
1.1.4 Overview of the PDMFCS	8
1.1.5 Summary of Research on the PDMFCS	12

1.1.6	Towards a Modular PDMFCS	14
1.2	Objectives of This Study	16
1.3	Thesis Outline	17
2	Literature Review	18
2.1	Modelled Dynamics in the PDMFCS	18
2.1.1	Overview	18
2.1.2	Critical Evaluation of Past Microfluidic Tubing Characterizations	19
2.2	HECM of Sample Tubing	20
2.2.1	HECM in the PDMFCS	20
2.2.2	HECM Outside of the PDMFCS	22
2.2.3	Critical Evaluation of the HECM	23
2.3	Pressure Transient Models in Other Contexts	23
2.4	Summary	24
3	Methodology	25
3.1	Experimental Plan	25
3.1.1	Dynamic Characterization With a Transfer Function	25
3.1.2	Experimental Determination of the Transfer Function	26
3.1.3	Parameters Affecting Pressure Transient Response	27
3.1.4	Dimensional Analysis	29
3.2	Experimental Setup	31
3.2.1	General Apparatus	31
3.2.2	Experimental Parameters	33
3.2.3	Other Practical Considerations	39
3.3	Data Analysis	43
3.3.1	Pressure Wave Amplitude and Phase Estimation	44
3.3.2	Determination of Magnitude and Phase Frequency Response	45

3.3.3	Estimation of Transfer Function From Experimental Frequency Response	46
3.3.4	Uncertainty	47
3.4	HECM Model Analysis	48
3.4.1	HECM Primary Model Form	48
3.4.2	Transfer Function Determination	49
3.4.3	Comparison of Experimental and HECM Dynamic Response	50
3.4.4	Lower Order HECM Model Forms	52
3.4.5	Modelling Considerations and Assumptions	54
4	Results and Discussion	56
4.1	Experimental Pressure Waves and OLS Fit	56
4.2	Experimental Frequency Response and Simulated Transient	60
4.2.1	General Form	60
4.2.2	Increasing Pressure Amplitude	62
4.2.3	Increasing Pressure Offset	64
4.2.4	Increasing Length-Diameter Ratio	67
4.2.5	Increasing Fluid Viscosity	70
4.2.6	Increasing Tubing Material Stiffness	73
4.2.7	Summary	75
4.3	Hydrodynamic Equivalent Circuit Model	76
4.3.1	Comparison to Experimentally Estimated TF	76
4.3.2	Effect of Varying Tubing/Fluid Parameters	84
4.3.3	Summary	92
5	Conclusion & Recommendations	94
5.1	Conclusion	94
5.2	Recommendations	96

Letters of Copyright Permission	97
References	106
APPENDICES	118
A Dimensional Analysis	119
B Measurement System Characterization	122
B.1 Pressure Sensor Static Calibration	122
B.2 Dynamic Characterization of Pressure Sensor Setup	125
C Pressure Junction Drawings	129
D Data Analysis Code	132
E Hydrodynamic Equivalent Circuit Model Transfer Function Derivation	133
E.1 Symmetric HECM	133
E.2 Second-Order HECM	137
E.3 First-Order HECM	139
E.3.1 RC Circuit	139
E.3.2 RL Circuit	140
F Supplementary Results	141
F.1 Increasing Pressure Offset	142
F.2 Increasing Length-Diameter Ratio	144
F.3 Increasing Fluid Viscosity	146
F.4 Increasing Tubing Material Stiffness	148

List of Figures

1.1	Miniature integrated DNA analysis device. From M. A. Burns, B. N. Johnson, S. N. Brahma-sandra, K. Handique, J. R. Webster, M. Krishnan, T. S. Sammarco, P. M. Man, D. Jones, D. Heldsinger, C. H. Mastrangelo, and D. T. Burke, “An integrated nanoliter dna analysis device,” <i>Science</i> , vol. 282, no. 5388, pp. 484–487, 1998. [Online]. Available: https://www.science.org/doi/abs/10.1126/science.282.5388.484 . Reprinted with permission from AAAS.	2
1.2	Visualization of droplet microfluidics in a T-junction chip. Pressures at the chip inlets p_{c_1} , p_{c_2} , and p_d are actuated to manipulate the disperse phase. .	3
1.3	Schematic and operating principle of passive flow focusing droplet generation. Reprinted from Z. Che, N.-T. Nguyen, and T. N. Wong, “Hydrodynamically mediated breakup of droplets in microchannels,” <i>Applied Physics Letters</i> , vol. 98, no. 5, p. 054102, 02 2011. [Online]. Available: https://doi.org/10.1063/1.3552680 , with permission from AIP publishing. .	5
1.4	Schematic and operating principle of passive droplet merging chip design. Droplet enters merging chamber of decreasing width, second droplet enters causing coalescence of droplets and release of merged droplet from chamber. Reproduced from X. Niu, S. Gulati, J. B. Edel, and A. J. deMello, “Pillar-induced droplet merging in microfluidic circuits,” <i>Lab Chip</i> , vol. 8, pp. 1837–1841, 2008. [Online]. Available: http://dx.doi.org/10.1039/B813325E , with permission from the Royal Society of Chemistry.	6
1.5	Active selective droplet splitting device with external valve. Actuation of valve by airflow creates pressure on the chip channel resulting in deformation and splitting of the disperse phase. Reprinted from <i>Sensors and Actuators B: Chemical</i> , vol. 292, Selective droplet splitting using single layer microfluidic valves, pp. 233–240, Copyright (2019), with permission from Elsevier. . . .	7

1.6	Finger actuated electrowetting on dielectric digital microfluidic device. User applies pressure to piezoelectric material, converting mechanical energy to electrical energy to actuate droplets. Reproduced from C. Peng, Z. Zhang, C.-J. im, and Y. S. Ju, “Ewod (electrowetting on dielectric) digital microfluidics powered by finger actuation,” <i>Lab Chip</i> , vol. 14, pp. 1117–1122, 2014. [Online]. Available: http://dx.doi.org/10.1039/C3LC51223A , with permission from the Royal Society of Chemistry.	7
1.7	Actuation for the pressure-driven droplet microfluidic feedback control system. Pump pressure channels (p_{p1} , p_{p2} , p_{p3} , p_{p4}) are controlled independently, and hooked up to separate reservoirs in the reservoir holder. Each reservoir contains either continuous or disperse phase fluid. Air at requested pressure is sent from a pump channel, through the air tubing, to the specific reservoir, where sample fluid then flows from the reservoir, through the sample tubing, and into the specific inlet of a chip channel. The common case of a T-junction chip is illustrated in this figure. Notice that the pressure’s at the inlet of the chip (p_{c1} , p_{c2} , p_d , i.e pressure for continuous phase channel 1, continuous phase channel 2, and disperse phase channel respectively) are different than the pressures output by the pump. The hookups for p_{c2} and p_d are not shown for clarity. Further, the hookups between a given pressure channel and the corresponding chip channel are not unique, e.g. in the figure p_{p3} is connected to p_{c1} , but in practice p_{p1} , p_{p2} , p_{p3} or p_{p4} could be hooked up to p_{c1}	9
1.8	Visualizations of various types of position requests possible with the PDM-FCS: a) Interface displacement of unbroken disperse phase, b) displacement of droplet interface, c) sequence of displacements of unbroken disperse phase to generate a droplet, d) displacements of two separate droplet interfaces to merge droplets into a larger droplet, e) displacement of separate interfaces of the same droplet to split it into two smaller droplets.	10
1.9	High-level visualization of PDMFCS operation for a standard T-junction chip: 1) User requests a specific position (displacement) for a given interface, 2) computer intakes reference position and measured actual position of interface, software implementation of controller sends optimized control signal (request for pressure output) to the pump, 3) pump actuates the pressures at the chip inlets (p_{c1} , p_{c2} , p_d), 4) droplet interface displaces from initial position, 5) new droplet position is measured by a high-speed camera and microscope setup and sent to the computer. Process repeats until there is no error between the requested and actual position.	11

1.10	Modular platform with stacking representation. Modularity allows user to select a droplet manipulation they want to perform, stacking abstracts the physics and engineering involved in said droplet manipulation so the user only has to understand what they want to do, not how. From M. Hébert, J. Huissoon, and C. L. Ren, “A perspective of active microfluidic platforms as an enabling tool for applications in other fields,” <i>Journal of Micromechanics and Microengineering</i> , vol. 32, no. 4, p. 043001, mar 2022. [Online]. Available: https://dx.doi.org/10.1088/1361-6439/ac545f , reprinted under the CC BY license (link: https://creativecommons.org/licenses/by/4.0/).	13
1.11	PDMFCS plant SISO block diagram representation of single-pressure channel with pressure request as input and displacement of interface as output. a) Plant, pressure request signal from computer $p_0(t)$ not shown, b) subsystem block diagram representation, c) combined system block diagram representation.	15
2.1	HECM considered for sample tubing.	21
3.1	High level schematic of experimentally measuring the FR for the pressure dynamics across the sample tubing at a given frequency. Constant frequency sinewave requested from pump, $p_0(t)$. Sinewave propagates through pressure channel components to the sample tubing inlet, $p_3(t)$, and outlet, $p_4(t)$. Simultaneous measurements of $p_3(t)$ and $p_4(t)$ are obtained using pressure sensors PS_1 and PS_2 respectively. Outlet of tubing connected to microfluidic chip to accurately model internal pressure dynamics present in sample tubing in real operation of PDMFCS.	27
3.2	Apparatus used to measure transient pressure waves across sample tubing. Note that the grey box under each pressure sensor is a junction that was machined to integrate the pressure sensors into the microfluidic setup. . . .	32
3.3	Measurement, continuous, and disperse channel of microfluidic chip in context of experiments. Sample tubing with pressure sensor shown upstream of chip. Note that the grey box under the pressure sensor is a junction that was machined to integrate the pressure sensor into the microfluidic setup.	33
3.4	Visualization of lengths of tubing in experimental apparatus for measurement channel. Pressure sensor connections to sample tubing shown. Note that the grey box under each pressure sensor is a junction that was machined to integrate the pressure sensors into the microfluidic setup.	34

3.5	Microfluidic chip designs used in experiments. a) Chip design used for experimental cases evaluating effect of varying P_A , P_{off} , $\frac{L}{D_i}$, and μ . b) Chip design used for experimental case evaluating effect of varying E . MC, DC, CC, stand for Measurement Channel, Disperse Channel, and Continuous Channel respectively, see Section 3.2.1 and Figure 3.3. All chips have a channel depth (into the page) of $50 \mu\text{m}$ and a channel width of $100 \mu\text{m}$	39
3.6	Sketch of cross-section of junction used to implement pressure sensors. Flow channel is the channel through which the working fluid is transported through the measurement setup.	40
3.7	a) Visualization of lengths of tubing in experimental apparatus for continuous and disperse channel. b) Orientation of continuous, disperse, and measured channels in experimental setup, air tubing connection not shown. Note that the red box represents the set containing the continuous and disperse channel tubing.	43
3.8	Symmetric HECM of sample tubing used for comparison to experimental results.	49
3.9	Second-order HECM of sample tubing used for comparison to experimental results	53
3.10	First-order RC HECM of sample tubing used for comparison to experimental results	53
3.11	First-order RL HECM of sample tubing used for comparison to experimental results	54
4.1	Beginning portion of input and output pressure wave measurements with $P_{\text{off}} = 150 \text{ mbar}$, $P_A = 0.25P_{\text{off}}$, and $f = 0.01 \text{ Hz}$. Steady-state measurement regions were used for OLS fitting and FR analysis. $p_{3\text{m}}$ and $p_{4\text{m}}$ represent the pressure wave measurements at the inlet and outlet of the sample tubing respectively. Measurement uncertainties are not shown for the purpose of visual clarity.	57
4.2	Measured and estimated steady-state pressure waves wave measured at the inlet of the sample tubing with $P_{\text{off}} = 150 \text{ mbar}$ and $P_A = 0.25P_{\text{off}}$. a) $f = 0.01 \text{ Hz}$, b) $f = 0.4 \text{ Hz}$. Measurement uncertainties are not shown for the purpose of visual clarity.	59
4.3	Bode plot of FR from experiment and estimated TF for $P_{\text{off}} = 150 \text{ mbar}$ and $P_A = 0.25P_{\text{off}}$	62

4.4	Experimental and estimated FR for increasing P_A	64
4.5	Experimental (points) and estimated (lines) FR for $P_{\text{off}} = 50$ and 250 mbar.	65
4.6	Simulated step response for estimated TF from experimental FR for $P_{\text{off}} = 50$ and 250 mbar.	66
4.7	Dimensionless experimental (points) and estimated (lines) FR for $\frac{L}{D_i} = 90$ and 197.	68
4.8	Simulated step response for estimated TF from experimental FR for $\frac{L}{D_i} = 90$ and 197. Step response was simulated from dimensional estimated TF, not the dimensionless form.	69
4.9	Dimensionless experimental (points) and estimated (lines) FR for $\nu = 5$ and 100 cSt.	71
4.10	Simulated step response for estimated TF from experimental FR for $\nu = 5$ and 100 cSt.	72
4.11	Dimensionless experimental (points) and estimated (lines) FR for $E_{\text{flex}} = 0.590$ (HPPFA) and 4.10 GPa (PEEK).	74
4.12	Comparison of FR of governing TF for symmetric HECM, $G_C(s)$, and experimentally estimated TF, $G_p(s)$, for pressure transient dynamics across sample tubing. For FR of $G_C(s)$, Wong et al.'s (2.3), thin wall (2.4), and thick wall (2.5) compliance models were considered. Uncertainties in experimental FR points are not shown for the purpose of visual clarity.	79
4.13	Comparison of FR of governing TF for second-order HECM, $G_C(s)$, and experimentally estimated TF, $G_p(s)$, for pressure transient dynamics across sample tubing. For FR of $G_C(s)$, Wong et al.'s (2.3), thin wall (2.4), and thick wall (2.5) compliance models were considered. Uncertainties in experimental FR points are not shown for the purpose of visual clarity.	80
4.14	Comparison of FR of governing TF for second-order HECM, $G_L(s)$, and experimentally estimated TF, $G_p(s)$, for pressure transient dynamics across sample tubing. For FR of $G_L(s)$, Wong et al.'s (2.3), thin wall (2.4), and thick wall (2.5) compliance models were considered. Uncertainties in experimental FR points are not shown for the purpose of visual clarity.	81

4.15	Comparison of FR of governing TF for first-order RC HECM, $G_C(s)$, and experimentally estimated TF, $G_p(s)$, for pressure transient dynamics across sample tubing. For FR of $G_C(s)$, Wong et al.'s (2.3), thin wall (2.4), and thick wall (2.5) compliance models were considered. Uncertainties in experimental FR points are not shown for the purpose of visual clarity.	82
4.16	Comparison of FR of governing TF for first-order RL HECM, $G_R(s)$, and experimentally estimated TF, $G_p(s)$, for pressure transient dynamics across sample tubing. For FR of $G_R(s)$, Wong et al.'s (2.3), thin wall (2.4), and thick wall (2.5) compliance models were considered, but have no effect in this case. Uncertainties in experimental FR points are not shown for the purpose of visual clarity.	83
4.17	FR's of governing TF for first-order RC HECM, $G_C(s)$, for increasing tubing L . Wong et al.'s (2.3) compliance model considered.	85
4.18	Simulated step responses for governing TF for first-order RC HECM, $G_C(s)$, for increasing tubing L . Wong et al.'s (2.3) compliance model considered.	86
4.19	FR's of governing TF for first-order RC HECM, $G_C(s)$, for increasing tubing D_i . Wong et al.'s (2.3) compliance model considered.	87
4.20	Simulated step responses for governing TF for first-order RC HECM, $G_C(s)$, for increasing tubing D_i . Wong et al.'s (2.3) compliance model considered.	88
4.21	FR's of governing TF for first-order RC HECM, $G_C(s)$, for increasing fluid ν . Wong et al.'s (2.3) compliance model considered.	89
4.22	Simulated step responses for governing TF for first-order RC HECM, $G_C(s)$, for increasing tubing ν . Wong et al.'s (2.3) compliance model considered.	90
4.23	FR's of governing TF for first-order RC HECM, $G_C(s)$, for increasing E_{tens} . Wong et al.'s (2.3) compliance model considered.	91
4.24	Simulated step responses for governing TF for first-order RC HECM, $G_C(s)$, for increasing tubing E_{tens} . Wong et al.'s (2.3) compliance model considered.	92
B.1	Apparatus used to calibrate pressure sensors.	123
B.2	Calibration plot of PS_1 with OLS fit.	124
B.3	Calibration plot of PS_2 with OLS fit.	125
B.4	Apparatus used to dynamically characterize pressure sensor setup.	126

B.5	a) Response of second-order model overlapped with experimental time-domain step response data for an input pressure of 25 mbar, every 5th point shown for clarity, b) Error between simulated output and measured output at each time step, c) Input step signal.	127
B.6	Estimated FR for pressure measurement setup for increasing pressure, frequency region over which pressure transient dynamics across sample tubing is characterized highlighted in green.	128
E.1	Symmetric HECM.	133
E.2	KVL loops for symmetric HECM.	134
E.3	Second-order HECM.	137
E.4	First-order RC HECM.	139
E.5	First-order RL HECM.	140
F.1	Experimental (points) and estimated (lines) FR for increasing P_{off}	142
F.2	Simulated step responses for estimated TF from experimental FR for increasing P_{off}	143
F.3	Experimental (points) and estimated (lines) FR for increasing $\frac{L}{D_i}$	144
F.4	Simulated step responses for estimated TF from experimental FR for increasing $\frac{L}{D_i}$	145
F.5	Experimental (points) and estimated (lines) FR for increasing ν	146
F.6	Simulated step responses for estimated TF from experimental FR for increasing ν	147
F.7	Experimental (points) and estimated (lines) FR for increasing E_{flex}	148

List of Tables

3.1	Lengths of tubing considered to vary $\frac{L}{D_i}$	34
3.2	Lengths of other tubing segments.	35
3.3	Investigated tubing materials, E_{flex} data from IDEX [78] measured at 23 °C.	35
3.4	Properties of silicone oil used in experiments, all properties measured by the manufacturer [87] at 25°C.	36
3.5	Input pressure amplitudes considered with constant $P_{\text{off}} = 200$ mbar.	37
3.6	Input pressure offsets considered with constant $P_A = 0.25P_{\text{off}}$	38
3.7	Lengths of tubing used for continuous and disperse channels.	43
3.8	Estimated values of E_{tens} for tubing materials considered in experiments from other manufacturers/suppliers. Used in HECM parameter calculations.	50
4.1	Estimated parameters of (3.7) from OLS estimation of input pressure wave for 0.01 and 0.4 Hz frequency cases, with $P_{\text{off}} = 150$ mbar and $P_A = 0.25P_{\text{off}}$. Relative uncertainties shown.	60
4.2	Parameters for estimated TF from experimental FR for $P_{\text{off}} = 150$ mbar and $P_A = 0.25P_{\text{off}}$. Relative uncertainties given.	62
4.3	Parameters for estimated TF from experimental FR's investigating the effect of varying P_A . Relative uncertainties given.	64
4.4	Parameters and associated time constants for estimated TF's from experimental FR's investigating the effect of varying P_{off} . Note that absolute uncertainties are given to show that the increase (decrease) in corner frequency (time constant) for an increase in P_{off} is statistically significant.	66

4.5	Parameters and associated time constants for estimated TF's from dimensional experimental FR's investigating the effect of varying $\frac{L}{D_i}$. Note that absolute uncertainties are given to show that the decrease (increase) in corner frequency (time constant) for an increase in $\frac{L}{D_i}$ is statistically significant.	69
4.6	Parameters and associated time constants for estimated TF's from experimental FR's investigating the effect of varying viscosity. Note that absolute uncertainties are given to show that the decrease (increase) in corner frequency (time constant) for an increase in viscosity is statistically significant.	72
4.7	Parameters and associated time constants for estimated TF's from experimental FR's investigating the effect of varying tubing material stiffness. Note that absolute uncertainties are given to show that the effect of varying material stiffness on the corner frequency and time constant cannot be verified statistically due to the overlapping uncertainty bounds.	75
4.8	Comparison of governing simulated step response characteristic for HECM forms and experimentally estimated TF.	78
A.1	Primary dimensions of variables	119
B.1	Natural frequency, ω_n , and damping ratio, ζ , of pressure sensor setup second-order model with increasing pressure.	128
F.1	Parameters for estimated TF's from dimensionless experimental FR's investigating the effect of varying $\frac{L}{D_i}$. Note that absolute uncertainties are given.	145

List of Abbreviations

μ TAS Micro Total Analysis System 1, 2

DAQ data acquisition system 31, 39, 40, 122, 126

FR frequency response 26–30, 35, 37, 38, 40, 41, 43, 45–48, 51, 52, 56, 58, 60, 61, 63, 65, 67, 70, 72–77, 94–96, 125, 127, 141

GLM general linear model 44, 47

HECM hydrodynamic equivalent circuit model 16–20, 22–25, 48–52, 54–56, 76, 77, 83, 84, 92–96, 133–140

ID inner diameter 31, 33, 35–37, 41, 67, 73, 93, 122, 125

LTI linear time-invariant 25, 26, 43

MIMO multi-input multi-output 12, 15, 26, 55

OD outer diameter 33, 35, 36, 40, 41, 129

OLS ordinary least squares 45, 56, 57, 61, 123

PDMFCS pressure-driven droplet microfluidic feedback control system 8, 12–20, 22–29, 32, 36, 42, 48, 52, 56, 61, 65, 67, 70, 73, 75–77, 92–96, 125

SISO single-input single-output 15, 18, 25, 26

TF transfer function 15, 16, 25, 26, 29, 38, 41, 42, 46, 48–54, 56, 60, 61, 63, 65, 69, 70, 72–77, 84, 93–95, 135–140

List of Symbols

Roman Symbols

A	cross-sectional area of tubing flow channel
A_p	amplitude of assumed pressure sinewave model
A_{p_3}	amplitude of assumed pressure sinewave model at inlet of sample tubing
A_{p_4}	amplitude of assumed pressure sinewave model at outlet of sample tubing
A_{tube}	cross-sectional area of tubing
a	estimated numerator parameter of pressure transient transfer function
b	estimated denominator parameter of pressure transient transfer function
C	hydrodynamic capacitance
$C_{w_{\text{thin}}}$	thin tubing wall hydrodynamic capacitance
$C_{w_{\text{thick}}}$	thick tubing wall hydrodynamic capacitance
D_i	inner diameter
d	estimated delay parameter of pressure transient transfer function
d_d	disperse phase interface displacement
d_h	hydraulic diameter
E	material elasticity
E_{flex}	flexural modulus
E_{tens}	tensile (Young's) modulus
f	frequency (cycles per second)
G_C	transfer function for hydrodynamic capacitance component
G_L	transfer function for hydrodynamic inductance component
G_R	transfer function for hydrodynamic resistance component
G_p	estimated transfer function for pressure transient dynamics across sample tubing
I	current
$\mathbf{I}_{\text{ident}}$	identity matrix
L_{hyd}	hydrodynamic inductance

L	length of sample tubing
L_{dim}	fundamental dimension of length
L_1	first hydrodynamic inductance component (relative to flow inlet) in symmetric HECM ($= \frac{L_{\text{hyd}}}{2}$)
L_2	second hydrodynamic inductance component (relative to flow inlet) in symmetric HECM ($= \frac{L_{\text{hyd}}}{2}$)
l_c	length of sample tubing from reservoir to continuous channel inlet
l_d	length of sample tubing from reservoir to disperse channel inlet
l_0	length of air tubing between the pump and the reservoir
l_1	length of sample tubing between the reservoir and the inlet pressure sensor
l_2	length of sample tubing between the inlet and outlet pressure sensor ($= L$)
l_3	length of sample tubing between the outlet pressure sensor and microfluidic chip
M	fundamental dimension of mass
m	general sinewave model offset
n	number of measurements in measured pressure vector for GLM representation of pressure measurements
P_A	amplitude of requested pressure wave
P_{atm}	atmospheric pressure
P_{cal_1}	calibrated pressure output for inlet pressure sensor
P_{cal_2}	calibrated pressure output for outlet pressure sensor
P_{off}	offset of requested pressure wave
P_{step}	pressure requested from pump for dynamic characterization of pressure sensor junctions
P_3	Laplace transform of pressure signal output from the reservoir (input to the sample tubing) in a single pressure channel of the plant of the PDMFCS
P_4	Laplace transform of pressure signal output from the sample tubing (input to the microfluidic chip) in a single pressure channel of the plant of the PDMFCS
PS_1	pressure sensor located at inlet of sample tubing
PS_2	pressure sensor located at outlet of sample tubing
$\mathbf{P}_{\mathbf{x}_{pm}}$	orthogonal projection of model matrix ($= \mathbf{X}_{pm}(\mathbf{X}_{pm}^T \mathbf{X}_{pm})^{-1} \mathbf{X}_{pm}^T$)
p	pressure from a general sinewave model

p_{c_i}	pressure at the i th continuous phase inlet of a T-junction microfluidic chip
p_d	pressure at the disperse phase inlet of a T-junction microfluidic chip
p_m	general measured pressure
\mathbf{p}_m	measured pressure vector for GLM representation of pressure measurements
p_{p_i}	pressure output at the i th channel of the microfluidic pressure pump
p_0	pressure signal request sent from the controller to the pump in a single pressure channel of the plant of the PDMFCS
p_1	pressure signal output from the pump (input to the air tubing) in a single pressure channel of the plant of the PDMFCS
p_2	pressure signal output from the air tubing (input to the reservoir) in a single pressure channel of the plant of the PDMFCS
p_3	pressure signal output from the reservoir (input to the sample tubing) in a single pressure channel of the plant of the PDMFCS
p_4	pressure signal output from the sample tubing (input to the microfluidic chip) in a single pressure channel of the plant of the PDMFCS
p_{3_m}	pressure measured at inlet of sample tubing
p_{4_m}	pressure measured at outlet of sample tubing
Q	volume flow rate
R	hydrodynamic resistance
R_c^2	coefficient of determination
R_e	Reynolds number
R_1	first hydrodynamic resistance component (relative to flow inlet) in HECM ($= \frac{R}{2}$)
R_2	second hydrodynamic resistance component (relative to flow inlet) in HECM ($= \frac{R}{2}$)
r	rank of general sinewave model matrix for GLM representation of pressure measurements
r_i	tubing inner radius
s	complex frequency-domain variable
T	fundamental dimension of time
T_r	rise time
T_s	settling time
t	time
t_{val}	t-value
V	voltage drop
V_C	voltage drop across capacitive component of HECM

V_L	voltage drop across inductive component of HECM
V_R	voltage drop across resistive component of HECM
w_t	tubing wall thickness
\mathbf{X}_{p_m}	general sinewave model matrix for GLM representation of pressure measurements
x_i	i th independent variable of a general function
y	a general function of independent variables

Greek Symbols

α_i	i th general sinewave model parameter
$\boldsymbol{\alpha}$	general sinewave model parameter vector for GLM representation of pressure measurements
β_a	adiabatic bulk modulus
ΔP	pressure drop
Δu_{x_i}	uncertainty in calculated or measured value x_i
$\frac{\delta y}{\delta x_i}$	partial derivative of y with respect to x_i
ϵ_i	measurement error at some time t_i
$\boldsymbol{\epsilon}$	measurement error vector for GLM representation of pressure measurements
κ	tubing material stiffness ($= A_{\text{tube}} \frac{E_{\text{tens}}}{L}$)
μ	dynamic viscosity
ν	kinematic viscosity ($= \frac{\mu}{\rho}$)
ν_p	Poisson's ratio of tubing
ω	frequency ($= 2\pi f$)
ω_n	natural frequency
ϕ_p	phase of assumed pressure sinewave model
ϕ_{p_3}	phase of assumed pressure sinewave model at inlet of sample tubing
ϕ_{p_4}	phase of assumed pressure sinewave model at outlet of sample tubing
Π	dimensionless group
ρ	fluid density
σ^2	variance of the measurement error
τ	time constant for first-order system step response
ζ	damping ratio

Mathematical Symbols

\cdot^+	upper uncertainty bound
\cdot^-	lower uncertainty bound
$ \cdot $	magnitude of complex function
$\angle \cdot$	phase of complex function
$j(\cdot)$	imaginary number
$N(0, \sigma^2)$	Gaussian (normal) distribution
$\mathbf{N}(\mathbf{0}, \sigma^2 \mathbf{I}_{\text{ident}})$	normally distributed vector
$\hat{\cdot}$	estimate of random variable/vector
$\text{var}(\cdot)$	variance of random variable
$\text{cov}(\cdot)$	covariance of random vector

Chapter 1

Introduction

1.1 Background and Motivation

1.1.1 Essence of Microfluidics

Microfluidics can be described as the study of the physics, control, and applications of fluid flows through channels at the micrometer scale [1, 2]. An early, yet still prevalent, motivator for microfluidic study has been towards the development of a Micro Total Analysis System (μ TAS), alternatively described as a "Lab-on-a-Chip". First proposed in the analytical chemistry field by Manz et al. [3], a μ TAS is described by Sun and Kwok [4] as "an integrated miniaturized chemical analysis system that includes sample preparation, separation, and detection system[s] on a small, single chip". An early example of such a device is that of a miniature integrated DNA analysis device developed by Burns et al. [5], illustrated in Figure 1.1 below

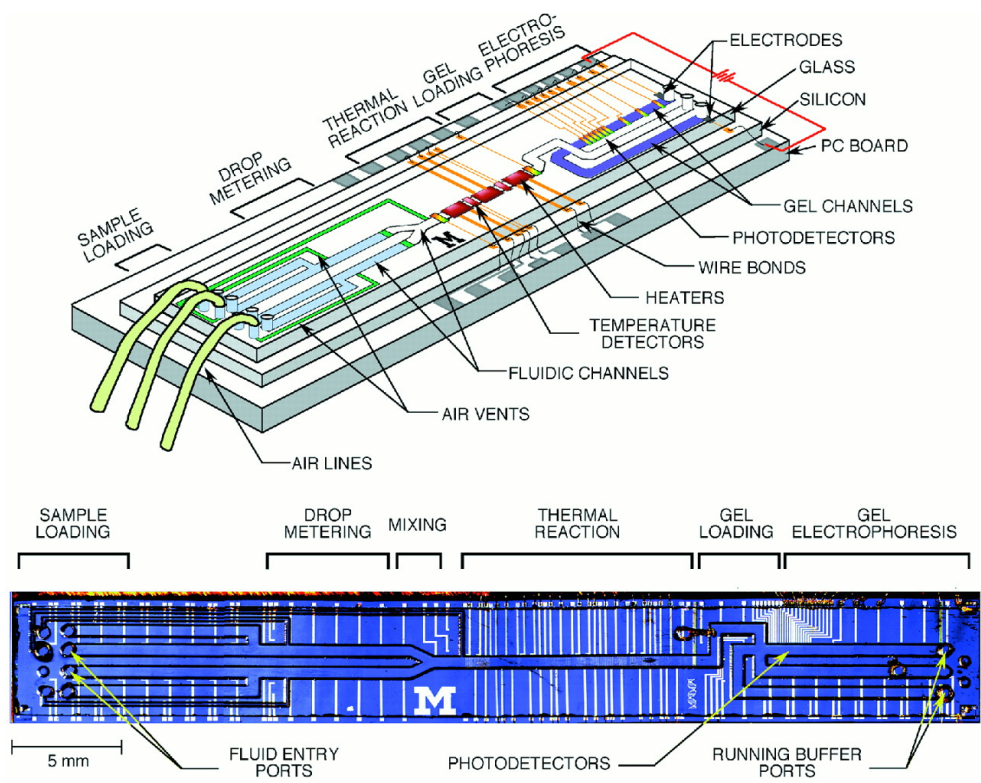


Figure 1.1: Miniature integrated DNA analysis device. From M. A. Burns, B. N. Johnson, S. N. Brahma-sandra, K. Handique, J. R. Webster, M. Krishnan, T. S. Sammarco, P. M. Man, D. Jones, D. Heldsinger, C. H. Mastrangelo, and D. T. Burke, “An integrated nano-liter dna analysis device,” *Science*, vol. 282, no. 5388, pp. 484–487, 1998. [Online]. Available: <https://www.science.org/doi/abs/10.1126/science.282.5388.484>. Reprinted with permission from AAAS.

As seen from the above biochemical example, the μ TAS concept is not unique to the chemistry field, rather research and implementation of this concept can be found in separate, as well as intersections, of many areas [6] that utilize the properties of fluids for analysis including, but not limited to, chemistry, life science, and biology [7, 8, 9].

While the notion of a μ TAS is intriguing, one may question why an analysis device on the microscale is useful. Speaking in a general sense, microfluidic analysis systems are advantageous over macroscale systems in that they reduce sample size and analysis time, increase throughput with a small device footprint, and automate easily [10]. Despite microfluidics many advantages, the wide adoption of microfluidics by non-expert end-users,

e.g. users in chemistry, life science, and biology fields with little to no microfluidic knowledge, is yet to occur. This is primarily due to the extensive amount of knowledge needed to operate, design, and select microfluidic devices for specific applications, due to the complexity of the flow physics at the microscale. This problem is pervasive throughout the microfluidics field, but recent research directions in droplet microfluidics, a subfield of microfluidics, show a possible solution to the adoption problem [11].

1.1.2 Droplet Microfluidics

Droplet microfluidics focuses on the study, control, and applications of immiscible two-phase flows within microchannels [12], as such it is a subfield of the overarching microfluidic field. Physically, droplet microfluidics is governed by the dynamics of two-phase immiscible flow, where droplets are formed from one fluid, the disperse phase, and carried through the chip by the other fluid, the continuous phase. The physical mechanisms for forming and manipulating droplets is extensively studied and tested in the field [13]. A visualization of this general description of droplet microfluidics, using a droplet microfluidic T-junction system as an example, is presented in Figure 1.2 below.

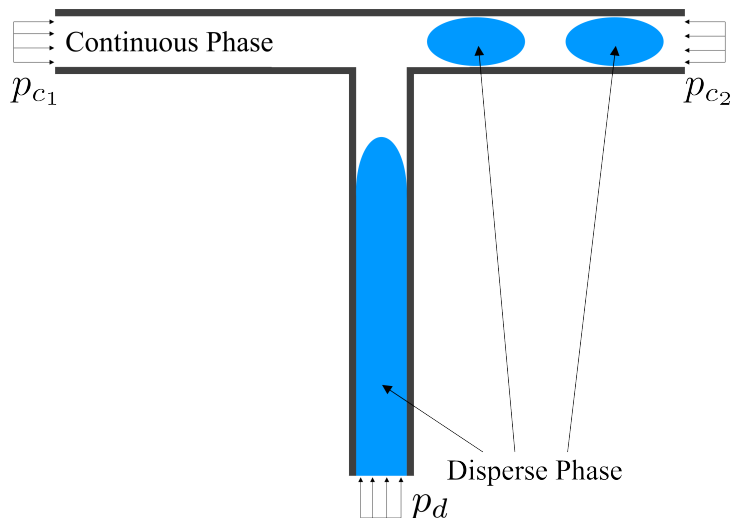


Figure 1.2: Visualization of droplet microfluidics in a T-junction chip. Pressures at the chip inlets p_{c1} , p_{c2} , and p_d are actuated to manipulate the disperse phase.

In comparison to single-phase microfluidic systems, droplet microfluidics operating prin-

ciple results in each reaction taking place in a self-contained droplet carried by the continuous phase. This is advantageous for its further reduction in sample consumption and reaction time, the segregation of reactions/processes to individual droplets (prevents cross-contamination and allows each reaction to be routed to a different area of the device), no contact between the droplet and the channel walls (due to the continuous phase wetting, prevents sample adsorption into the walls), and improved mixing due to the recirculating flow present in moving droplets [14, 15, 16, 17, 18]. Furthermore, the self-contained nature of the droplets allows for the implementation and study of various methods to control droplets.

1.1.3 Droplet Control Strategies

Throughout this thesis, droplet "control", or "manipulation" will refer to the act of manipulating the disperse phase in a two-phase droplet microfluidic system. Manipulations include any desired action the user forces the disperse phase to take. Examples of manipulation include droplet generation, splitting, merging, moving, mixing, sorting, and storage [19]. Droplet control strategies can be generalized to two categories: passive and active control [11, 15, 18, 20, 21, 22], a brief description of each is presented below. Many of the ideas discussed in this section are summarised from [11] and [22], these sources should be viewed for a more detailed discussion.

Passive Control

Passive control strategies rely on specific chip geometries and/or flow rate variations to control the disperse phase. The flow focusing system used for droplet generation developed by Che et al. [23] and the droplet merging device produced by Niu et al. [24] are examples of such device, see Figures 1.3 and 1.4 below.

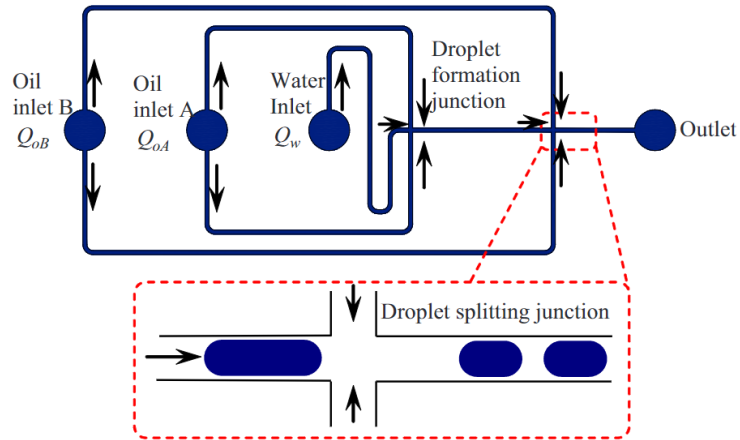


Figure 1.3: Schematic and operating principle of passive flow focusing droplet generation. Reprinted from Z. Che, N.-T. Nguyen, and T. N. Wong, “Hydrodynamically mediated breakup of droplets in microchannels,” *Applied Physics Letters*, vol. 98, no. 5, p. 054102, 02 2011. [Online]. Available: <https://doi.org/10.1063/1.3552680>, with permission from AIP publishing.

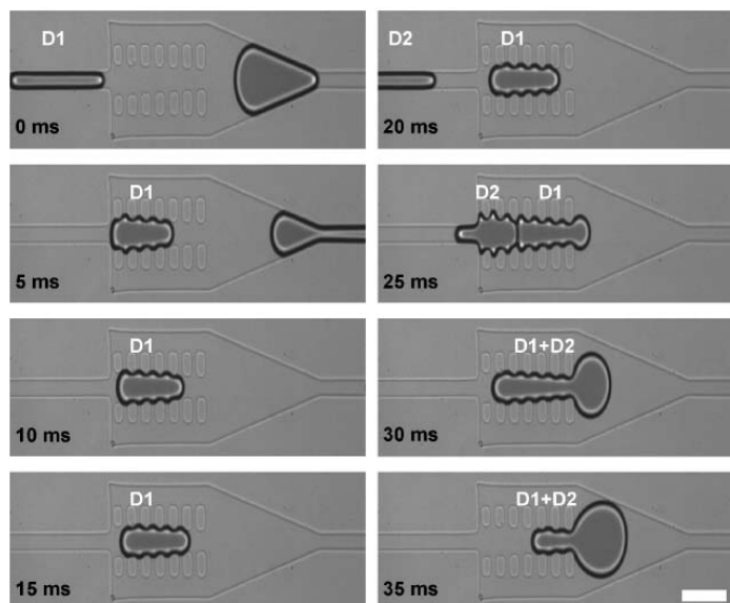


Figure 1.4: Schematic and operating principle of passive droplet merging chip design. Droplet enters merging chamber of decreasing width, second droplet enters causing coalescence of droplets and release of merged droplet from chamber. Reproduced from X. Niu, S. Gulati, J. B. Edel, and A. J. deMello, “Pillar-induced droplet merging in microfluidic circuits,” *Lab Chip*, vol. 8, pp. 1837–1841, 2008. [Online]. Available: <http://dx.doi.org/10.1039/B813325E>, with permission from the Royal Society of Chemistry.

Passive devices are suited for a single manipulation at a high throughput, where multiple manipulations are difficult due to the coupling of the flow field when passive devices are implemented in sequence. Further, passive methods do not help to solve the adoption problem as a microfluidic expert is typically required to use these passive devices to deal with the aforementioned flow field coupling, as well as the implementation, manufacturing, and complexity of the chip geometries for a given manipulation.

Active Control

Active control strategies utilize a force/actuation, typically external to the channel, to manipulate the disperse phase. Some examples of external actuation include valves [25], electric and magnetic fields (digital microfluidics) [26, 27], acoustic waves [28], and lasers

[29]. See Figures 1.5 and 1.6 for examples of an active droplet splitting method using a valve [25], as well as a electrowetting on dielectric digital microfluidic device with finger actuation [30], respectively.

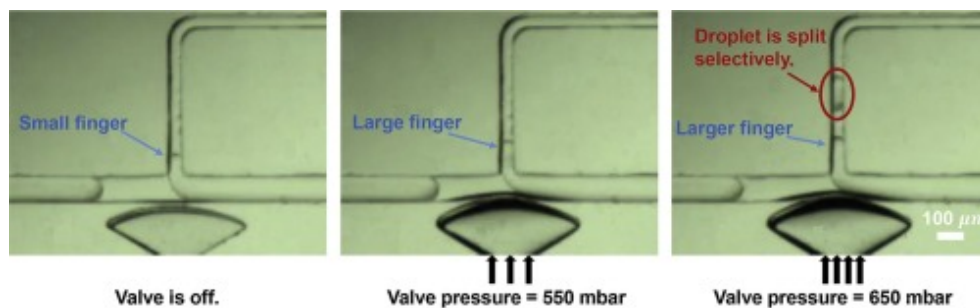


Figure 1.5: Active selective droplet splitting device with external valve. Actuation of valve by airflow creates pressure on the chip channel resulting in deformation and splitting of the disperse phase. Reprinted from Sensors and Actuators B: Chemical, vol. 292, Selective droplet splitting using single layer microfluidic valves, pp. 233–240, Copyright (2019), with permission from Elsevier.

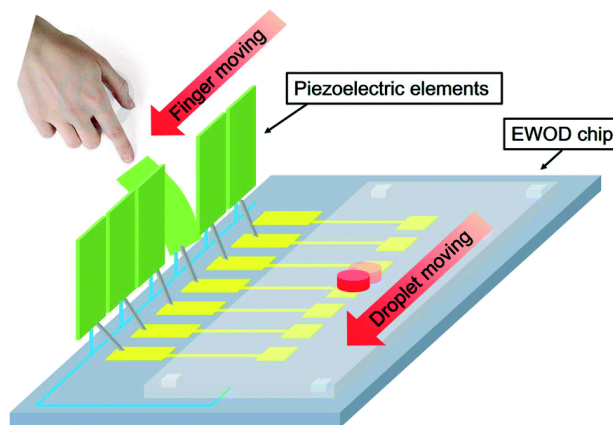


Figure 1.6: Finger actuated electrowetting on dielectric digital microfluidic device. User applies pressure to piezoelectric material, converting mechanical energy to electrical energy to actuate droplets. Reproduced from C. Peng, Z. Zhang, C.-J. im, and Y. S. Ju, “Ewod (electrowetting on dielectric) digital microfluidics powered by finger actuation,” Lab Chip, vol. 14, pp. 1117–1122, 2014. [Online]. Available: <http://dx.doi.org/10.1039/C3LC51223A>, with permission from the Royal Society of Chemistry.

For active platforms with external actuation, their implementation can be difficult due to the complexity of the manufacturing and setup of both the microfluidic carrier device and the external actuator. Further, for devices whose actuation depends on an additive to the droplet, e.g magnetic droplet control requires added ferromagnetic particles [31], the presence of the additive may limit the platform’s breadth of applications. This is due to the possibility that the additive in the droplet may destroy the cells it is carrying in a biological experiment [32], or modify the reaction occurring in a chemistry application. Active devices tend to have lower throughput than passive devices, but are able to perform sequential manipulations on the same device. Although, it should be noted that there are active devices that only target a single manipulation [25, 33, 34], but these are typically layered with a passive automation method increasing their throughput. However, the biggest advantage of active platforms, at least in the general sense, is that they can be developed to be end-user friendly. In other words, there is potential to develop active droplet control platforms that can solve the adoption problem inhibiting microfluidics from being used by non-experts in other disciplines. This is possible due to the inherent ability of these platforms to be developed such that the complexity of the flow physics and disperse phase manipulations is abstracted away with the use of appropriate sensing, actuation, and algorithms. With this development, the end-user only has to input what sort of manipulation they want the disperse phase to take, and the platform takes care of the rest. The pressure-driven droplet microfluidic feedback control system (PDMFCS) developed by Wong et al. [35, 36, 37] is an active platform that does not require external actuation, with the potential to solve the adoption problem.

1.1.4 Overview of the PDMFCS

The PDMFCS developed by Wong et al. [35, 36, 37] is an active droplet control platform that does not rely on external actuation, an advantageous feature for an easily adoptable active droplet control system. Instead actuation is internal to the system, utilizing a common pressure driven droplet microfluidic setup (Figure 1.7), with a pressure pump connected to a reservoir holder, containing individual reservoirs of the continuous and disperse phase fluid, where each reservoir is connected to its own inlet of the microfluidic chip. The pressure pump has individual channels that control the fluid pressure at the separate inlets of the microfluidic chip independently. It does this by outputting airflow through air tubing, at a set pressure, to the separate reservoirs in the holder. The fluid in the reservoir is then pushed through the sample tubing, due to hydrostatic pressure from the upstream airflow, and into the microfluidic chip.

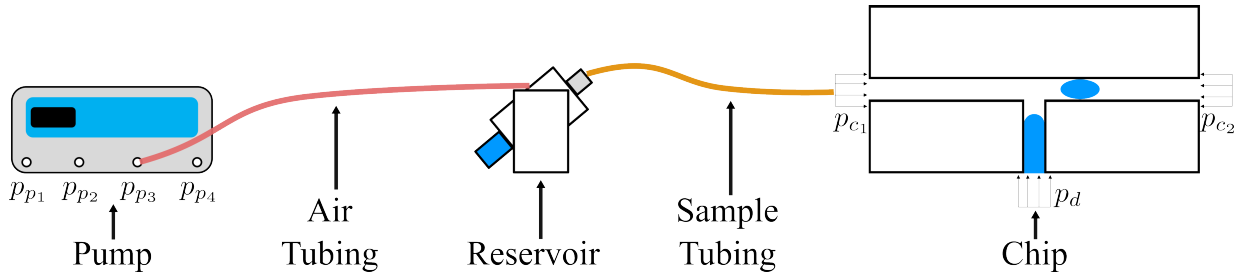


Figure 1.7: Actuation for the pressure-driven droplet microfluidic feedback control system. Pump pressure channels (p_{p_1} , p_{p_2} , p_{p_3} , p_{p_4}) are controlled independently, and hooked up to separate reservoirs in the reservoir holder. Each reservoir contains either continuous or disperse phase fluid. Air at requested pressure is sent from a pump channel, through the air tubing, to the specific reservoir, where sample fluid then flows from the reservoir, through the sample tubing, and into the specific inlet of a chip channel. The common case of a T-junction chip is illustrated in this figure. Notice that the pressure's at the inlet of the chip (p_{c_1} , p_{c_2} , p_d , i.e pressure for continuous phase channel 1, continuous phase channel 2, and disperse phase channel respectively) are different than the pressures output by the pump. The hookups for p_{c_2} and p_d are not shown for clarity. Further, the hookups between a given pressure channel and the corresponding chip channel are not unique, e.g. in the figure p_{p_3} is connected to p_{c_1} , but in practice p_{p_1} , p_{p_2} , p_{p_3} or p_{p_4} could be hooked up to p_{c_1} .

The operational objective of the system, ignoring the intricate details for now, is simply to allow the user to specify a position (displacement), or sequence of positions (displacements), for a disperse phase interface in the channel, the interface being the boundary between the continuous and disperse phase [38], and for the pressures at the chip inlets to be actuated such that the measured position(s) (displacement(s)) of the interface is equivalent to the interface position(s) (displacement(s)) requested by the user. Visualizations of the various types of position (displacement)/sequence of positions (displacements) requests to perform droplet manipulations are shown in Figure 1.8 below.

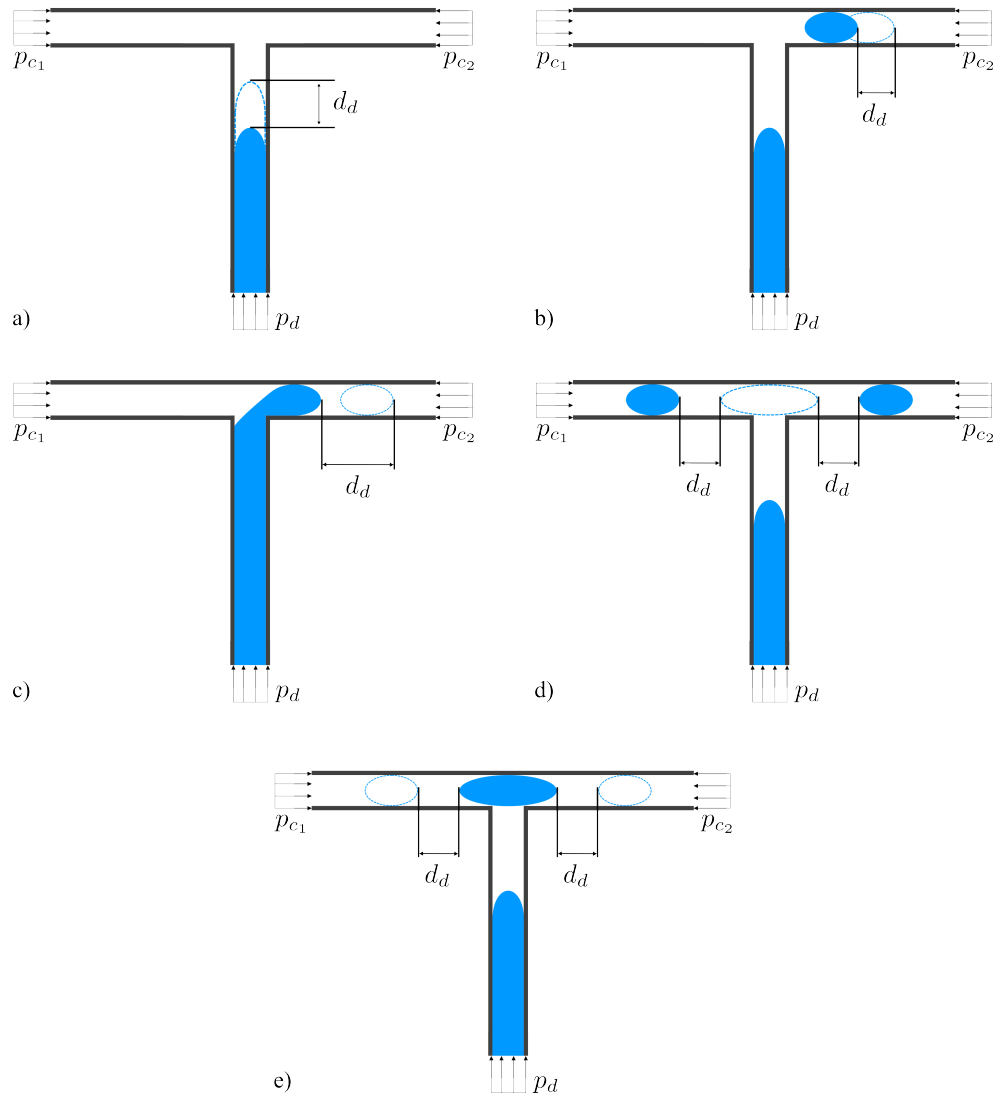


Figure 1.8: Visualizations of various types of position requests possible with the PDMFCS: a) Interface displacement of unbroken disperse phase, b) displacement of droplet interface, c) sequence of displacements of unbroken disperse phase to generate a droplet, d) displacements of two separate droplet interfaces to merge droplets into a larger droplet, e) displacement of separate interfaces of the same droplet to split it into two smaller droplets.

Control of the interface position is accomplished using a tracking feedback control system, tracking meaning that the control system ensures the measured output position

(output signal) matches the user-requested position (reference signal) [39]. The physical implementation of the system is outlined in Figure 1.9 below. From a high-level, an interface position (displacement), or sequence of positions (displacements), is requested by the user using a computer containing the software implementation of the controller for the system. A high speed camera (Andor Zyla 5.5 [40]) and microscope (Nikon Eclipse Ti-E [41]) setup is used to sense the current position of the droplet for use as measurement feedback then, assuming that the requested position is different than the initial position, the controller sends an optimized control signal to the pump (MFCS-EZ [42]) (request for the pump to set the pressure at a given channel(s) to a certain level), the pump then changes the pressures at the inlet of each chip channel, and the interface displaces from its previous position. The new position of the interface is then sensed, and the process repeats until there is no error between the requested and actual position.

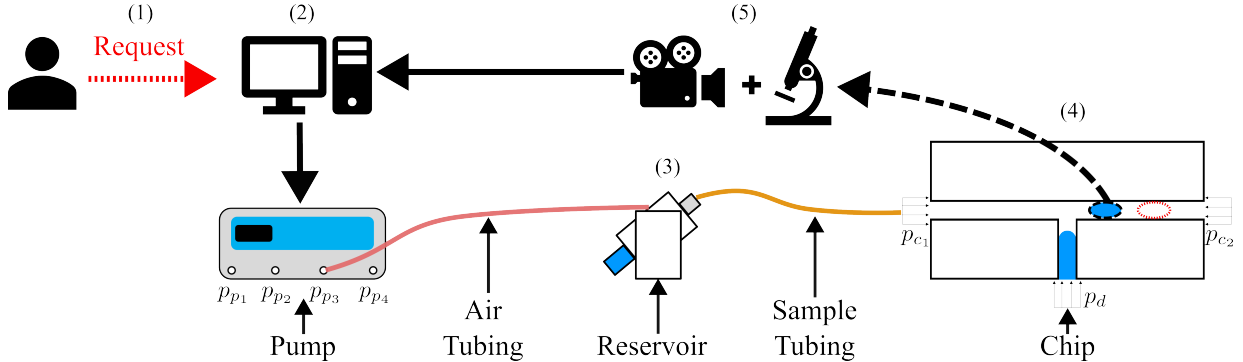


Figure 1.9: High-level visualization of PDMFCS operation for a standard T-junction chip: 1) User requests a specific position (displacement) for a given interface, 2) computer intakes reference position and measured actual position of interface, software implementation of controller sends optimized control signal (request for pressure output) to the pump, 3) pump actuates the pressures at the chip inlets (p_{c_1} , p_{c_2} , p_d), 4) droplet interface displaces from initial position, 5) new droplet position is measured by a high-speed camera and microscope setup and sent to the computer. Process repeats until there is no error between the requested and actual position.

With a high-level understanding of the system now established, it is necessary to summarize the main takeaways of past research on the platform to evaluate its current state.

1.1.5 Summary of Research on the PDMFCS

Proof of Concept

The initial development of the PDMFCS by Wong et al. [35, 36, 37] was motivated by a desire to develop a proof of concept active droplet control system that could arbitrarily manipulate droplets using a standard microfluidic setup without the need for an external actuator. The removal of the external actuator eliminates one of the fundamental limitations of active droplet control systems in solving the adoption problem [11], see Section 1.1.3. In this development, the system was not applied to a specific problem, but rather the system was developed solely to prove that such a device could be developed. The controller relies on a multi-input multi-output (MIMO) state-space description, a Linear Quadratic Regulator with integral action, and a full state observer.

Modularity and Component Level Breakdown

Following the development of the proof of concept PDMFCS, Hébert et al. [11, 22] contextualized the PDMFCS in terms of its application to the greater microfluidic community, by stressing the the PDMFCS should be developed to be a modular platform so it can be widely adoptable. A modular platform meaning that the system is easily implementable, and allows users to select different modules that follow a stacking principle, see Figure 1.10 below.

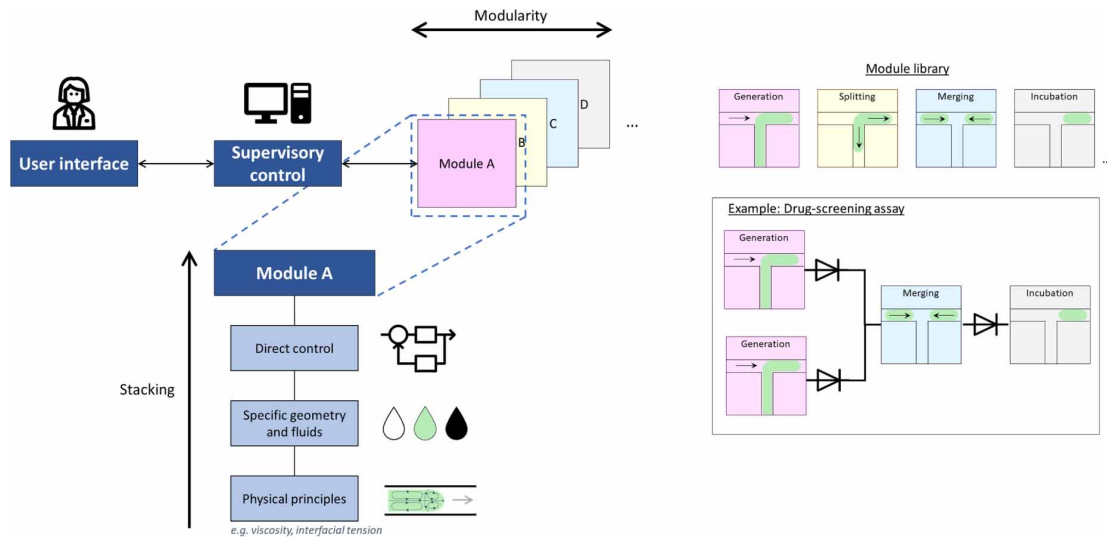


Figure 1.10: Modular platform with stacking representation. Modularity allows user to select a droplet manipulation they want to perform, stacking abstracts the physics and engineering involved in said droplet manipulation so the user only has to understand what they want to do, not how. From M. Hébert, J. Huissoon, and C. L. Ren, “A perspective of active microfluidic platforms as an enabling tool for applications in other fields,” *Journal of Micromechanics and Microengineering*, vol. 32, no. 4, p. 043001, mar 2022. [Online]. Available: <https://dx.doi.org/10.1088/1361-6439/ac545f>, reprinted under the CC BY license (link: <https://creativecommons.org/licenses/by/4.0/>).

Modularity and stacking imply that a user can perform a given droplet manipulation by simply choosing what type of manipulation they want to perform, without having to understand the physics/engineering that went into performing that manipulation. Following this contextualization, she also applied the system, with slight modifications to the modelling and control algorithm, to a real application [43]. As well, she critically evaluated the system components to determine the physical limitations of the PDMFCS and began experimentally investigating the dynamics of specific components of the system [44].

System Improvement and Controller Design

Recent research on the PDMFCS has been to bring the PDMFCS towards a realization of a modular platform. Thus far, advancement in this direction has been accomplished through improvements in the ease of implementation of the system such as developing

an open-source affordable precision pressure pump [45], designing a cost-effective lensless imaging sensor to replace the expensive microscope/camera [46], and redeveloping the software using various software organization/architecture practices and tools [47]. Zablony [48] and Chen [47] also simplified the model of the system and advanced the controller architecture, by implementing a model-predictive-controller and an adaptive controller respectively. However, since these new control schemes were not implemented for a real application nor was their performance quantitatively compared to past schemes, these model/controller redesigns have not yet proven to be an improvement in the modularity of the PDMFCS.

Summary

Collectively, the past research has brought the PDMFCS to a state in which there is a set of working systems, plant models, and controllers, as well as a baseline understanding of the limitations of the physical components. However, accurate methods of dynamically characterizing each plant component, an understanding of how the dynamics of a given plant component may change with variance of its physical properties, and the use of the system in independent studies/applications, outside of the in-lab study by Hébert et al. [43], is yet to be accomplished.

1.1.6 Towards a Modular PDMFCS

The main objectives of control system design are to ensure stability, output a suitable transient-response, minimize steady-state error and to be robust [49, 50]. Metrics to evaluate these objectives are designated on a case by case basis dependent on the application of the control system. If a control system satisfies the design objectives, it is deemed suitable for the application. In the context of a modular system, a suitable version of the PDMFCS is 1) the most general control system architecture that provides satisfactory droplet manipulations, i.e. satisfies the control system design objectives, for a wide array of microfluidic applications, and 2) acts as a foundational system from which advancements are easily implemented for microfluidic applications that the general system provides unsatisfactory control for. To realize the modular potential of the PDMFCS, it is hypothesised that it is critical to first develop experimental methods to dynamically characterize plant components and use these methods to understand how the dynamics of a given plant component may vary, before solely focusing on pushing the PDMFCS to general applications. In the PDMFCS's current state, it can not be reliably used for general applications due to insuf-

efficient knowledge of the true dynamic characteristics of the system hindering an informed and robust control system design process.

There are multiple benefits to developing experimental methods for characterization of the dynamics of each component of the plant. For example, consider a single-input single-output (SISO) system representation of a single pressure channel of the plant in the PDMFCS, see Figure 1.11 below.

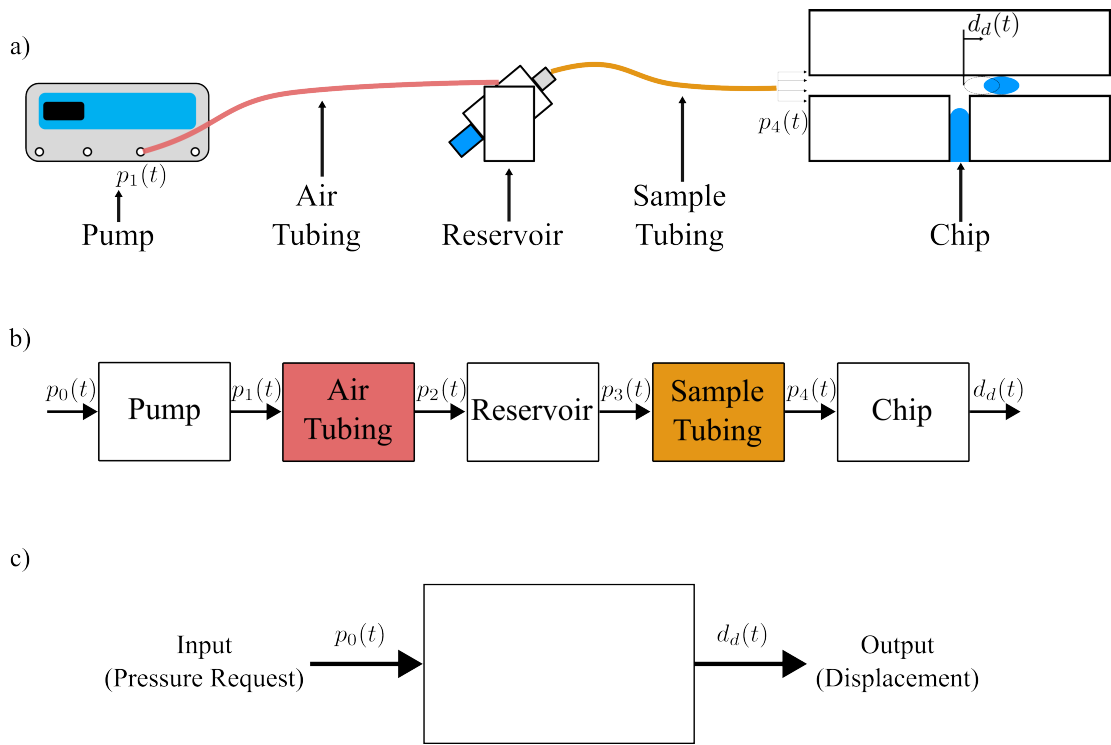


Figure 1.11: PDMFCS plant SISO block diagram representation of single-pressure channel with pressure request as input and displacement of interface as output. a) Plant, pressure request signal from computer $p_0(t)$ not shown, b) subsystem block diagram representation, c) combined system block diagram representation.

Developing a SISO transfer function (TF) for each subsystem of the individual pressure channels of the plant allows the cumulative dynamics of each pressure channel to be characterized in the model-based control system design. This is accomplished by incorporating each TF into the overall MIMO state-space model of the system through TF matrix realizations and concatenations as was done for some components by Wong et al.

[35, 36]. State-space controller designs rely on both the measured output and the accuracy of the system model to determine optimal control signals and accurate state estimation for desired system performance [51, 52]. Also, from a robust control system design perspective, accurate models are necessary to safely ensure that the system is robust and that stability is maintained in meeting frequency domain performance requirements [53]. Despite these positives, the designer may also choose to not incorporate these dynamics due to them being negligible, increasing model order, making the state-space description unobservable/uncontrollable/unstable, increasing computation time, or making the model numerically ill conditioned [51, 54, 55]. Regardless, it is essential that an understanding, and ideally a model, of the dynamics for each subsystem in the PDMFCS is developed so that in developing/advancing the system for a specific application, the control system designer understands the dynamics that most greatly affect the performance. Such an understanding allows the designer to make informed decisions about modelling and controller designs, while ensuring stability in the system. Further, by investigating how the dynamics of the plant vary with changes in its physical characteristics, there is potential to quantify the uncertainty of a given plant model for use in a robust control scheme [53].

1.2 Objectives of This Study

The primary plant model used in the PDMFCS models the microfluidic chip channels and sample tubing as a hydrodynamic equivalent circuit model (HECM) where an input pressure signal results in a interface displacement [36, 43]. However, the degree of accuracy of these models to the true dynamics of the subsystems they are representing, in the context of the PDMFCS, is yet to be thoroughly explored. Thus, to enhance the understanding of the dynamics of the components of the PDMFCS plant such that future studies can work to develop an improved and robust control system design methodology to bring the PDMFCS towards modularity, the objectives of this study are as follows:

1. Develop an experimental methodology to estimate a TF representing the pressure transient dynamics across the sample tubing in the PDMFCS, with 95% confidence in parameter values.
2. Determine the effect of varying the geometric, material, and fluidic properties of the sample tubing system on the experimentally estimated TF.
3. Compare the dynamic response of the sample tubing system determined experimentally to that predicted by the HECM of the sample tubing system used by previous iterations of the PDMFCS.

1.3 Thesis Outline

This thesis is organized as follows: A critical review on the prior modelling/characterization performed on the PDMFCS plant components, the HECM used to approximate the sample tubing dynamics, and pressure transient models developed for other fluid mechanics applications is presented in Chapter 2. Chapter 3 outlines the experimental methodology and data analysis procedures. The experimental results and discussions are detailed in Chapter 4. Conclusions and recommendations are summarised in Chapter 5

Chapter 2

Literature Review

Thus far, the pressure transient dynamics across the sample tubing in the PDMFCS have not been properly experimentally characterized. Yet, proper experimental characterization and modelling of the dynamics of the plant components within the PDMFCS is essential to improve the modularity and design methodology for the system, see Section 1.1.6. As such, this chapter begins with an overview of previously modelled dynamics in the PDMFCS, followed by a critical evaluation of past experimental characterizations of the dynamics across microfluidic tubing in Section 2.1. Section 2.2 discusses and critiques the HECM of the sample tubing used in prior PDMFCS implementations, while Section 2.3 details pressure transient models developed for other fluid applications and why they are, as of yet, not useful. The outcomes of this review are summarised in Section 2.4.

2.1 Modelled Dynamics in the PDMFCS

2.1.1 Overview

Considering the SISO subsystem representation of a single pressure channel in the PDMFCS (Figure 1.11 b)), the dynamics of each subsystem have been explored to varying degrees of thoroughness using both experimental and analytical methods. Wong et al. developed models of the sample tubing and chip analytically, and estimated a model of the pump experimentally [35, 37]. A similar, but contextually different, pump characterization was also performed by Recktenwald et al. [56] for the purpose of optimizing pressure signals at the inlet of a microfluidic chip. Hébert et al. experimentally characterised the pressure

transient dynamics across the air tubing [44]. As well, Hébert et al. briefly explored the dynamic relationship between the input pressure and output flow rate in the sample tubing in the context of an experimental dynamic chip compliance study [22, 57]. Another related study is that of Zeng et al. who characterized the pressure transient dynamics across fluidic reservoirs (outlet of air tubing to inlet of sample tubing) for the purpose of controlling pressure ratios for droplet generation [58].

2.1.2 Critical Evaluation of Past Microfluidic Tubing Characterizations

An evaluation of the HECM will be presented in Section 2.2, the present discussion is primarily concerned with the prior experimental characterizations of the tubing dynamics.

Air Tubing

In the context of the sample tubing pressure transient dynamics, the air tubing study by Hébert et al. [44] is not directly translatable, due to the fact that the outlet flow of the air tubing is essentially stopped by the fluid in the reservoir, and does not flow to the downstream components of the PDMFCS. Conversely, within the sample tubing, the sample fluid is not stopped at the outlet, but instead flows through the downstream chip. Therefore, it is clear that the air tubing characterization is modelling a different flow scenario than that physically occurring in the sample tubing during PDMFCS operation.

Dynamics Across the Fluid Reservoir

Clearly, the flow scenario through the reservoir is different than that occurring through the sample tubing. Since the reservoir is dealing with an inflow of air and an outflow of sample fluid at different flow speeds and entrance/exit regions, while the flow through the sample tubing will generally be single-phase through a constant geometric region. As such, the experimental characterization of the reservoir performed by Zeng et al. only captures the pressure transient from the outlet of the air tubing to the inlet of the sample tubing [58], so it is not suitable for characterizing the pressure transient dynamics across the sample tubing.

Sample Tubing

Hébert et al.'s characterization of the dynamic relationship between the input pressure and output flow rate of the sample tubing [22] relied on the outlet of the tubing being open to atmosphere as opposed to connected to an upstream chip, which is not conducive to experimentally characterizing the pressure-input flow-output sample tubing dynamics within actual operation of the PDMFCS. In actual PDMFCS operation the sample tubing is connected to a downstream microfluidic chip. Further, the present operation and modelling of the plant in the PDMFCS relies on an input pressure signal resulting in an output interface displacement, thus the sample tubing dynamics within the plant would be best characterized using pressure transients. Therefore, these results would not be suitable for evaluating the accuracy of the HECM of the sample tubing in the PDMFCS plant model.

2.2 HECM of Sample Tubing

2.2.1 HECM in the PDMFCS

In the PDMFCS, a HECM was derived by Wong et al. [35] to model the dynamics of both the sample tubing and the microfluidic chip channels. In this description, pressure is equated to voltage and flow rate is analogous to current. The symmetric circuit representation is shown in Figure 2.1 below. Note that in Wong et al.'s implementation [35, 36], a non-symmetric case was used to decrease model order. However, the symmetric case is theorized to be more accurate as it maintains the symmetry of the response in the practical implementation of the sample tubing and chip system where flow arbitrarily moves from input to output and vice versa [22], and it models the continuous nature of the losses as the fluid moves through the sample tubing [59].

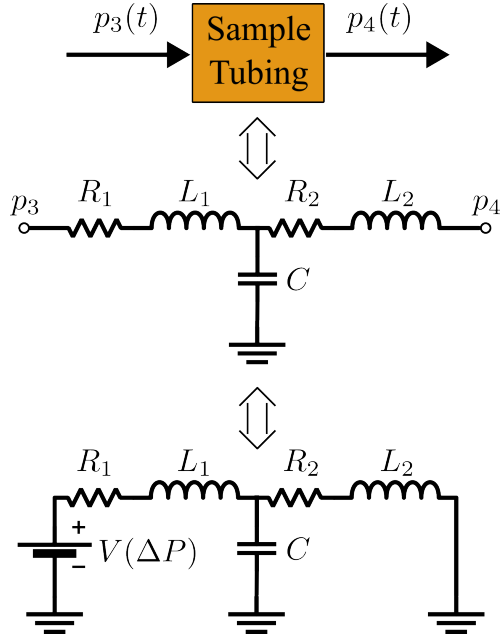


Figure 2.1: HECM considered for sample tubing.

The derivation of the circuit parameters is based off a control volume (CV) analysis of both a rigid and axially flexible CV of a fluid element, hinging on the assumptions of steady-state flow and fluid incompressibility. From the analysis, hydrodynamic equivalents to resistance,

$$R = \frac{32\mu L}{d_h^2} \quad (2.1)$$

inductance,

$$L_{\text{hyd}} = \rho L \quad (2.2)$$

and capacitance

$$C = \frac{A}{\kappa} + \frac{L}{\beta_a} \quad (2.3)$$

are found, representing hydraulic resistance (conversion of kinetic energy into heat from viscosity effects [60]), fluid inertia, and material compliance respectively. Note that μ is

dynamic viscosity $[\text{Pa} \cdot \text{s}]$, L is sample tubing length $[\text{m}]$, d_h is hydraulic diameter $[\text{m}]$, ρ is fluid density $[\frac{\text{kg}}{\text{m}^3}]$, A is the cross-sectional area of the tubing channel $[\text{m}^2]$, $\kappa = A_{\text{tube}} \frac{E_{\text{tens}}}{L}$ [57] is tubing material stiffness $[\text{Pa} \cdot \text{m}]$, β_a is fluid adiabatic bulk modulus $[\text{Pa}]$, and in the symmetric model $R_1 = R_2 = \frac{R}{2}$ and $L_1 = L_2 = \frac{L_{\text{hyd}}}{2}$. Also, capacitance is the superposition of the compliance of the tubing/chip material and the compliance of the fluid.

2.2.2 HECM Outside of the PDMFCS

The HECM has been used in other microfluidic studies outside of the PDMFCS, with different derivations and use cases [61]. Notably, the study by Vedel [59] attempted microfluidic system modelling with an HECM, even including an experimental investigation of pressure transients within the sample tubing and comparison to a HECM. The only noticeable difference in their HECM derivation was how they modeled the tubing compliance considering thin and thick wall assumptions, where the thin and thick wall tubing compliance equations are given by

$$C_{w_{\text{thin}}} = \frac{2\pi r_i^3 L}{E_{\text{tens}} w_t} \quad (2.4)$$

and

$$C_{w_{\text{thick}}} = \frac{2\pi r_i^3 L}{E_{\text{tens}}} (1 + \nu_p) \quad (2.5)$$

Where, r_i is the inner radius of the tubing $[\text{m}]$, L is the length of the tubing $[\text{m}]$, E_{tens} is the Young's modulus of the tubing $[\text{Pa}]$, w_t is the wall thickness of the tubing $[\text{m}]$, and ν_p is the Poisson's ratio of the tubing respectively. Vedel's results showed similar qualitative behaviour between the HECM model and the experimental measurements, but the model output was clearly out of phase and failed to accurately capture the low frequency behaviour of the pressure response. Further, Vedel's experimental design was flawed and not useful in the context of obtaining results relevant to the PDMFCS. As their experimental setup modelled a water hammer scenario [62], with fluid filled tubing capped at both ends by pressure sensors and a weight dropped at its center to initiate a sudden pressure pulse, as opposed to a flow through scenario with a downstream chip which is more realistic to the operation of the PDMFCS.

2.2.3 Critical Evaluation of the HECM

In critically evaluating the HECM from the context of physical operation of the PDMFCS, the steady-state flow assumption is concerning. This assumption physically implies that the pressure drop, and therefore the flow rate, across the tubing is changed, and reaches steady-state, almost instantaneously. Where, the small transient time is due to the time it takes for the fluid energy to overcome the inertial (inductance) and compliance (capacitance) effects. At steady-state, the pressure (velocity) field is no longer changing with respect to time (inductor acts as short circuit) and no more flow energy is used to expand the walls of the tubing (capacitor acts as an open circuit). Given that the PDMFCS operation relies on continual change of the pressure at the inlets of the chip resulting in an interface displacement, it is necessary to assess the true nature of the pressure transient dynamics across the sample tubing experimentally, and compare it to that assumed by the HECM model.

2.3 Pressure Transient Models in Other Contexts

As summarised by Hébert et al.'s [44] experimental study characterizing the pressure transient dynamics across the air tubing of the PDMFCS, the pressure transient/unsteady flow problem is not unique to microfluidic systems, and is prevalent in the greater fluid mechanics literature. In fact, similar studies and models have popped up in the context of pressure transients in fluid measurement lines [63, 64, 65], blood flow through arteries [66], thick walled tubing deformation [67], and water hammer applications [62]. However, as Hébert et al. concluded, these scenarios either differ significantly enough from the context of the pressure transient across the tubing of the PDMFCS, or the resulting models are not useful from a control system perspective, that specific experimental investigation is warranted. Further to this point, in Doebelin's discussion of the well-studied problem of dynamic effects of connecting tubing in fluid measurement lines, he notes that experimental testing must be performed in order to determine regions of accuracy of models and/or accurate system dynamic characteristics [68]. Thus, experimental characterization of the sample tubing pressure transient dynamics is necessary to assess if any of these prior models are suitable for approximating the sample tubing dynamics in the PDMFCS. Although this study is only concerned with testing the validity of the HECM due to its consistent use in the PDMFCS, a future research direction is to systematically test contextually different pressure transient models against the experimental characterization of the sample tubing pressure transients. This would determine if any models of the prior pressure transient

models, although different in the context of which they were developed, approximate the pressure transient dynamics experimentally characterized within this work, an abstract application of the system identification process [69].

2.4 Summary

Prior system dynamic studies have failed to experimentally model the pressure transients across the sample tubing in the plant of the PDMFCS in a physically realistic setup, and the present HECM for the sample tubing relies on physically unrealistic assumptions. As well, pressure transient models and experiments outside of the microfluidic context do not approximate a similar flow scenario to that occurring over the sample tubing in the PDMFCS. Further to this, in order to assess whether any of these models may be suitable for approximating the sample tubing dynamics, a comparison must be made to experimentally characterized dynamics. Thus, development of an experimental methodology to characterize the pressure transient dynamics across the sample tubing, along with an assessment of the change in dynamics with variation in the tubing/fluid properties and a comparison of the experimentally determined pressure transient response to that predicted by the HECM, is necessary to improve the understanding of, and develop a more accurate model for, the PDMFCS plant dynamics. An improved understanding of the plant dynamics, and/or a more accurate plant model, will assist in the development of an informed and robust control system design procedure, such that a modular PDMFCS can be achieved.

Chapter 3

Methodology

Presented in this study is an experimental characterization of the pressure transient dynamics across the sample tubing subsystem in the plant of the PDMFCS, so as to improve the accuracy of the plant dynamic model such that informed and robust control system design methodologies can be developed for the PDMFCS, to enhance its modular capabilities. Changes of the dynamics with variation in the tubing and fluid properties, as well as a comparison to the pressure transient dynamics predicted by the present HECM were also evaluated. To perform this study, development of an appropriate experimental plan, measurement setup, and data analysis scheme was essential. Further, derivation of the mathematical representation of pressure transients in the HECM for comparison to experimental results was necessary. Thus, this chapter is concerned with first presenting the experimental plan in Section 3.1, followed by the measurement setup in Section 3.2, then the data analysis scheme in Section 3.3, and finally the HECM analogies to sample tubing pressure transients in Section 3.4.

3.1 Experimental Plan

3.1.1 Dynamic Characterization With a Transfer Function

For a SISO system modelled as linear time-invariant (LTI), the TF provides a complete dynamic characterization of the model, i.e. a complete mathematical model of the systems response to arbitrary inputs [39, 49, 51, 70]. As discussed in Section 1.1.6, each component of a single-pressure channel of the plant in the PDMFCS can be modelled as a SISO system,

see Figure 1.11. So, if the system is assumed to be LTI, each pressure channel component can be modelled as a SISO TF, considered in the overall TF of a single-pressure channel, and each pressure channel TF can be considered and implemented into the MIMO state-space representation of the plant [51, 54]. Therefore, given that the PDMFCS plant has been primarily modelled as LTI [35, 36], it was practical to characterize the pressure transient dynamics of the sample tubing in TF form using experimental input-output pressure data.

3.1.2 Experimental Determination of the Transfer Function

The TF model of a LTI system can be determined from either time or frequency domain input-output data, considering either a set of parameterized models (parametric system identification) or without assuming a model form (non-parametric system identification) [69]. A non-parametric identification method was ideal for characterizing the pressure transient dynamics due to the inherent complexity of modelling, and the lack of literature providing a suitable model for, the pressure transient dynamics across tubing in the PDM-FCS plant. Further, non-parametric modelling helps to negate any bias in perceived model form for the dynamic data. From the possible non-parametric identification methods, the frequency response (FR) method was chosen. The FR identification method was selected as it can result in a more accurate TF estimation than time-domain methods [49]. Further, the physical implementation of the plant allowed for a simple procedure to send sinusoidal pressure inputs to the sample tubing component.

Experimentally determining the FR of the pressure transient dynamics across the sample tubing component in the PDMFCS plant involved a request for the pump to output a sinusoidal pressure signal at a constant frequency of the form

$$p_0(t) = P_{\text{off}} + P_A \sin(\omega t) \quad (3.1)$$

Where, P_{off} is the offset pressure about which the pressure wave oscillates [mbar], P_A is the amplitude of the pressure sinewave relative to P_{off} [mbar], ω is the frequency of oscillation [rad/s], and t is time [s]. This signal was propagated through the components of the plant to the sample tubing, where the pressure waves at the inlet and outlet of the tubing were measured simultaneously, see Figure 3.1 below. Note that in order to accurately model the internal pressure dynamics occurring in the plant during operation of the PDMFCS, it was imperative that the outlet of the sample tubing be connected to a downstream microfluidic chip.

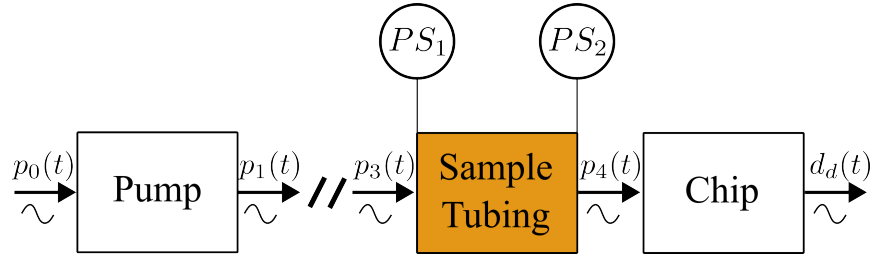


Figure 3.1: High level schematic of experimentally measuring the FR for the pressure dynamics across the sample tubing at a given frequency. Constant frequency sinewave requested from pump, $p_0(t)$. Sinewave propagates through pressure channel components to the sample tubing inlet, $p_3(t)$, and outlet, $p_4(t)$. Simultaneous measurements of $p_3(t)$ and $p_4(t)$ are obtained using pressure sensors PS_1 and PS_2 respectively. Outlet of tubing connected to microfluidic chip to accurately model internal pressure dynamics present in sample tubing in real operation of PDMFCS.

From simultaneous measurements of the steady-state pressure waves at the inlet and outlet of the sample tubing, the magnitude and phase FR at the frequency of interest was determined. Note that steady-state in this case refers to the portion of the wave at which any transient effects due to poles present in the system response to a sinusoidal input signal have dissipated [51]. This process was repeated over the frequency range necessary to completely characterize the FR of the sample tubing pressure dynamics. For the sample tubing considered in this study, the appropriate frequency range for dynamic characterization was determined from a preliminary qualitative assessment [64] to be from 0.01 to 0.4 Hz inclusive. However, one should note, that using different tubing/fluid outside of that considered in this study may influence this range. So an appropriate frequency range for different tubing/fluids should be determined experimentally on a case by case basis.

3.1.3 Parameters Affecting Pressure Transient Response

Within microfluidic applications, the selection of the sample tubing is based on meeting specific geometric and material requirements to ensure a microfluidic device operates as intended. Further, applications will use specific continuous/disperse phase fluid and flow properties to reach operation objectives. Given that it is intended for the PDMFCS to be modular for different applications, it was deemed pertinent that the variation of pressure transient dynamics of the sample tubing with change in these sample tubing, fluid, and flow properties be experimentally investigated. Difference in microfluidic chip design may also affect the dynamics, but investigation of this was neglected in this study.

Properties of the Sample Tubing

For a given set of applications, the sample tubing may vary in both geometric and material properties. Sample tubing varies predominantly in its inner diameter, D_i , length, L , wall thickness, w_t , and tubing material elasticity, E . Due to the tubing available for purchase (Section 3.2.2) and practical limitations of the experimental setup (Section 3.2.3) the effect of w_t was not explored.

Fluid Properties

Microfluidic flow is predominantly governed by viscous forces, $Re \ll 1$, due to the small flow diameter and low flow velocity. So, fluid inertia and the effect of density, ρ , is typically negligible [1, 71]. Further, the PDMFCS is typically operated in a lower flow rate regime to enhance the precision of the control [35, 36, 43]. Thus, in the context of these experiments only the viscosity, μ , of the fluid was varied. However, it should be mentioned that there are inertial microfluidic systems [72] which operate in a regime where inertia is no longer negligible. In this case, the effect of density would be useful to investigate, but this is outside the scope of this study.

Pressure Wave Properties

Hébert et al.'s previous study of the air tubing pressure dynamics noted the pressure transient dynamics of the air tubing in the PDMFCS plant were dependent on the input pressure [44]. Notably, some models of pressure transients in measurement lines also show a dependency on the input pressure [68]. These observations, coupled with the input pressure sinewave requested from the pump depending on an offset pressure and corresponding amplitude (3.1), necessitated investigation of the effect of varying P_{off} and P_A on the pressure transient dynamics across the sample tubing. Clearly, the use of FR also necessitated variation of the frequency of oscillation of the pressure wave, ω , as discussed in Section 3.1.2.

Effect of the Downstream Microfluidic Chip

The effect of varying the design of the downstream microfluidic chip on the pressure transient dynamics of the sample tubing was not investigated in this study. Microfluidic chip design's affect on the upstream pressure transient across the sample tubing is unknown.

The amount of parameters and complexity involved in microfluidic chip design makes investigation of this effect more suitable for a separate study. In order to make any effect of the downstream chip negligible, the same chip design was used when varying a given parameter and pressure transients were measured far away from the inlet of the chip.

Summary

Experimental parameters varied in this investigation were determined based off their likelihood of affecting the pressure transient dynamics across the sample tubing in the PDMFCS plant, as well as their necessity for experimental determination of the TF using FR. These parameters were selected by considering the envisioned outcome of this study to bring the PDMFCS towards modularity, the breadth of different sample tubing and fluid used in microfluidic applications, fundamental microfluidic knowledge, prior pressure transient studies, and practical limitations of the experiments. These parameters were the geometric and material sample tubing properties (D_i , L , E), the viscosity of the sample fluid (μ), and the amplitude pressure, offset pressure, and frequency of the requested pressure wave from the pump (P_{off} , P_A , ω), specified by (3.1). The effect on the pressure dynamics of varying the tubing wall thickness, w_t , was not explored due to practical limitations. Further, the effect of the design of the downstream microfluidic chip on the pressure transient dynamics was not investigated, as this phenomena would be best treated as a separate experimental study.

3.1.4 Dimensional Analysis

Given that there were seven experimental parameters to vary, ignoring w_t for reasons given in Section 3.1.3, dimensional analysis [73] was performed to try and reduce this number. Considering the analytical representation of the FR of the pressure transient dynamics across the sample tubing in polar form as

$$G_p(j\omega) = \frac{P_4(j\omega)}{P_3(j\omega)} = |G_p(j\omega)|\angle G_p(j\omega) \quad (3.2)$$

where, $|G_p(j\omega)|$ is the magnitude FR and $\angle G_p(j\omega)$ is the phase FR, both considered dimensionless variables. Then from the experimental parameters to vary described in Section 3.1.3, it was concluded that

$$G_p(j\omega) \sim f(D_i, L, E, \mu, P_{\text{off}}, P_A, \omega) \quad (3.3)$$

Where clearly for a FR, ω is the variable which $G_p(j\omega)$ is plotted against. Selecting the scaling parameters to be D_i , μ , and P_{off} , due to these parameters being unable to form a dimensionless group and being the easiest to practically keep constant for a given experimental run, results in the dimensionless presentation

$$G_p(j\omega) \sim f\left(\frac{\omega\mu}{P_{\text{off}}}, \frac{P_A}{P_{\text{off}}}, \frac{L}{D_i}, \frac{E}{P_{\text{off}}}\right) \quad (3.4)$$

While this form does reduce the number of parameter variations, in practice it was not used for every parameter variation in this investigation. The reason for this is primarily due to the fact that in dimensionless form the effect of the scaling parameters cannot be explicitly shown due to these parameters also appearing in the abscissa (dimensionless frequency) of the FR plot. Where, within this study the specific effect of varying D_i , μ , and P_{off} was pertinent to explore. However, the dimensionless form was useful in exploring the effect of L and D_i , in dimensionless form $\frac{L}{D_i}$, as this form states that an increase in L is equivalent to a decrease in D_i and vice versa. If one considers the steady-state laminar pipe flow equation [73] given by

$$Q = \frac{\Delta P \pi D_i^4}{128 \mu L} \quad (3.5)$$

it is clearly seen that an increase in L is equivalent to a decrease in D_i or a decrease in the pressure drop ΔP , all of which result in a lower flow rate. The converse of this is also true. So, it was assumed that the relationship presented by $\frac{L}{D_i}$ could accurately model the qualitative effect of varying either L or D_i on $G_p(j\omega)$. Checking this assumption experimentally proved it to be reasonable. Thus the total number of experimental parameters varied in the investigation was brought down to five, those being P_A , P_{off} , $\frac{L}{D_i}$, E , and ω . Note that for every parameter $G_p(j\omega)$ was plotted against ω , except for $\frac{L}{D_i}$ where it was plotted non-dimensionally against $\frac{\omega\mu}{P_{\text{off}}}$. For a detailed derivation of these dimensionless parameters see Appendix A.

As an extension to this discussion, it is important to point out that it is also feasible to explore the effect of the dimensionless parameters $\frac{P_A}{P_{\text{off}}}$ and $\frac{E}{P_{\text{off}}}$, much like $\frac{L}{D_i}$. However, as previously discussed, the specific effect of P_{off} cannot be evaluated due to its coupling with the dimensionless frequency (abscissa) of the dimensionless FR plot. So, evaluation of $\frac{P_A}{P_{\text{off}}}$ and $\frac{E}{P_{\text{off}}}$ can only be done by varying the values of P_A and E respectively, which does not provide any experimental or analytical advantage in using the dimensionless forms of P_A and E .

3.2 Experimental Setup

3.2.1 General Apparatus

The experimental apparatus used to measure the pressure transient waves across the sample tubing is shown in Figure 3.2 below. A computer controlled a microfluidic air pressure pump (MFCS-EZ [0-1 bar] [74]) to send a sinusoidal pressure signal with a specific P_{off} , P_A , and ω as specified by (3.1). The pressure signal was transported by air tubing (SG-Tygon LMT-55, 1.30 mm inner diameter (ID) [75]) through a reservoir holder (Fluwell 4-Channel 2 mL Low Pressure [76]), containing reservoirs filled with silicone oil (viscosity varied). Oscillatory flow of silicone oil was then carried through sample tubing (properties varied). Pressure sensors (TE Connectivity U536D-H000015-001BG, gauge, 0-1 bar input range, 0-5 V F.S. output, 0.1% F.S. accuracy, rise time < 2 ms [77]) were placed at two points along the sample tubing, using specifically designed junctions, to measure the incoming and outgoing pressure waves. Analog voltage signals output from the sensors were sampled approximately simultaneously using a data acquisition system (DAQ) (NI USB-6003 [78]) at a rate of 1 kHz per channel with a 16-bit resolution. The DAQ was connected to a computer with a LabVIEW program to control analog signal sampling and data acquisition. The outlet of the sample tubing was connected to an inlet of the continuous phase channel (measurement channel) of a downstream microfluidic T-junction chip (polydimethylsiloxane (PDMS)). Remaining inlets of the chip had connecting sample tubing filled with silicone oil pressurised by the pump, with the other continuous phase channel (continuous channel) inlet being set to P_{off} , and what would be the disperse phase channel (disperse channel) inlet being set to P_{atm} (0 Bar). On chip activity was monitored using a microscope (Nikon Eclipse Ti-E [41]) with a camera (Andor Zyla 5.5 [40]) connected to the computer used to control the pump.

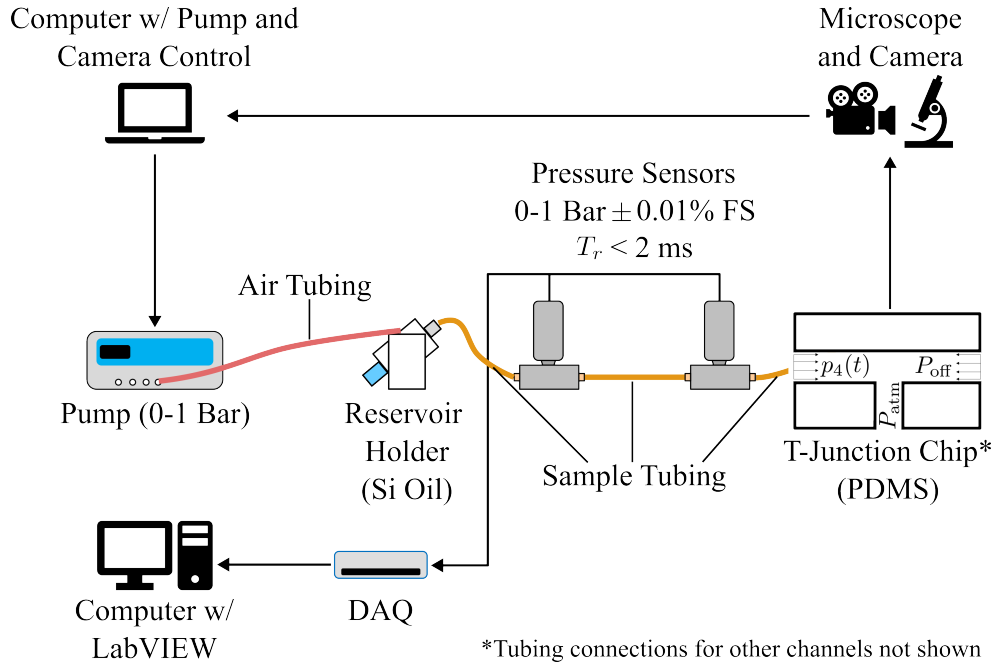


Figure 3.2: Apparatus used to measure transient pressure waves across sample tubing. Note that the grey box under each pressure sensor is a junction that was machined to integrate the pressure sensors into the microfluidic setup.

The experiments were performed using the same components present in the plant of the PDMFCS, with the addition of pressure sensing elements along the sample tubing. Notice that the outlet of the sample tubing was connected to a downstream microfluidic chip to ensure that the internal pressure dynamics that would be present in the sample tubing during PDMFCS operation are modeled as accurately as possible. P_{off} was requested at the pump for the continuous channel to: 1) account for the fact that the pump cannot send negative (vacuum) pressure signals and thus the input pressure wave sent through the measurement channel must oscillate around a positive (greater than atmospheric) pressure, and 2) simulate actual operation of the PDMFCS which will typically have at least one other channel pressurized to manipulate an interface. P_{atm} was requested at the pump for the dispense channel inlet to prevent any fluid flowing from the chip into the measurement channel (reversal of the flow direction) and to provide an outlet for the fluid flowing from the measurement and continuous channels. See Figure 3.3 below for visualization of the measurement, continuous, and dispense channel.

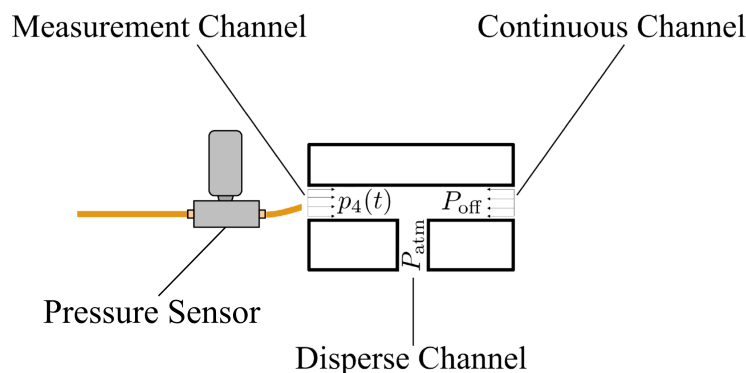


Figure 3.3: Measurement, continuous, and disperse channel of microfluidic chip in context of experiments. Sample tubing with pressure sensor shown upstream of chip. Note that the grey box under the pressure sensor is a junction that was machined to integrate the pressure sensor into the microfluidic setup.

3.2.2 Experimental Parameters

Sample Tubing Length and Diameter

FEP tubing (CTQ-FEP-3, 1/16 in outer diameter (OD), 763 μm ID, [79]) was used in every experiment except for variation of tubing material elasticity, E , which used tubing of varying material with a 1/16 in OD and 254 μm ID. The 763 μm ID tubing was preferred due to its inner diameter being closest to the size of the diameter of the channel in the machined junctions used to hold the pressure sensors, which is 0.04 in (1.016 mm), the possible effects and reasoning for this pressure junction diameter is discussed in Section 3.2.3. Further, a 1/16 in OD is a standard OD for sample tubing used in microfluidic applications, thus it is also a standard size for punched microfluidic chip inlets.

To vary the dimensionless geometric property of the tubing, $\frac{L}{D_i}$, the length of the tubing was varied according to Table 3.1 below.

Table 3.1: Lengths of tubing considered to vary $\frac{L}{D_i}$.

$L \pm 0.5$ [mm]	$\frac{L}{D_i} \pm 0.7$
69	90.4
90	118.0
110	144.2
130	170.4
150	196.6

Length of the tubing in this investigation is considered the length, L , between the two pressure sensor junctions as seen in Figure 3.4 below.

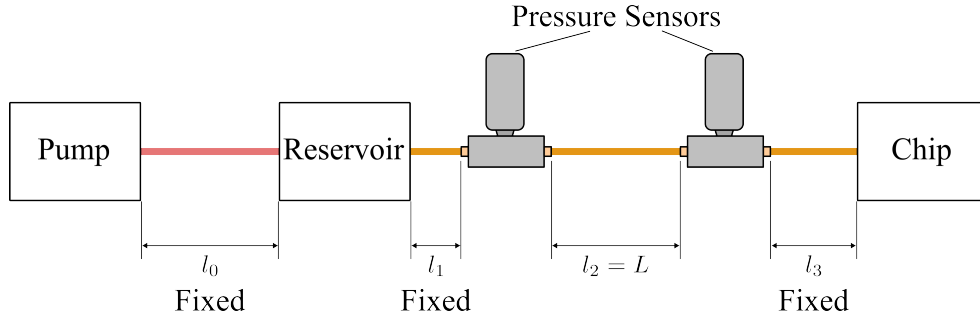


Figure 3.4: Visualization of lengths of tubing in experimental apparatus for measurement channel. Pressure sensor connections to sample tubing shown. Note that the grey box under each pressure sensor is a junction that was machined to integrate the pressure sensors into the microfluidic setup.

For experimental cases evaluating variation of P_A , P_{off} , and E , L was kept to 69 ± 0.5 mm. For the case evaluating the effect of varying μ , L was kept at 150 ± 0.5 mm to help diminish the amount of fluid expelled from the reservoir at lower fluid viscosities. In evaluating the effect of varying $\frac{L}{D_i}$, L was varied. Length of the air tubing, l_0 , and other connected sample tubing lengths (l_1 , l_3) were kept at a fixed length for each experiment, see Table 3.2 below. The air tubing length was chosen to allow practical ease of changing the variable length, L . Further, the sample tubing lengths were chosen to attempt to minimize the overall travel distance of the silicone oil so as to limit the attenuation of the pressure wave by the time it reached the inlet pressure sensor.

Table 3.2: Lengths of other tubing segments.

Segment	Length ± 0.5 [mm]
l_0	214
l_1	145
l_3	134

Sample Tubing Material Elasticity

Evaluation of the effect of the material elasticity on the pressure transient FR across the sample tubing required tubing of constant geometric properties that only varied in its elasticity. Notably, most microfluidic tubing manufacturers specify the flexural modulus of the material, E_{flex} instead of the tensile modulus, E_{tens} . However, according to materials theory E_{flex} can be taken to be a measure of elasticity (stiffness) of a material qualitatively equivalent to E_{tens} [80], so E_{flex} was used as a measure of material elasticity in this investigation. The tubing material considered for this investigation and its corresponding E_{flex} are presented in Table 3.3 below, E_{flex} data is from IDEX [81]. All tubing had an ID of $254 \mu\text{m}$, a 1/16 in OD, and was purchased from SciPro [82], the Canadian supplier for IDEX tubing.

Table 3.3: Investigated tubing materials, E_{flex} data from IDEX [78] measured at 23 °C.

Material	E_{flex} [GPa]
FEP	0.586
HPPFA	0.590
Tefzel ETFE	1.00
PEEK	4.10

The materials explored are not representative of all tubing materials used in microfluidic applications, two other well used materials are Tygon and PTFE which were used in a variety of studies, see [83, 84, 85, 86, 87, 88]. However, the selection of tubing available from standard microfluidic tubing suppliers that was geometrically equivalent and only varied in material elasticity was limited, but the available tubing had enough variation in E_{flex} to attempt to explore this effect. However, the limitation of the purchasable tubing resulted in the ID of the tubing for these tests being much smaller than the ID of the pressure sensor junction channel, ($254 \mu\text{m}$ as opposed to 1.016 mm), the effect of this is discussed in Section 3.2.3. To try and solve this problem, contacting custom tubing

suppliers was attempted, but a timely response was not received so this avenue was not explored.

Sample Tubing Wall Thickness

A further consequence of the constraint on purchasable tubing was in the properties necessary to investigate the dynamic effect of varying the wall thickness, w_t , of the tubing. This test required tubing of a constant ID and E , with a varying OD. Tubing available that satisfied this criteria had at largest a 250 μm ID, which presented the same problem with the pressure junctions noted for the tests exploring the material elasticity’s dynamic effect. Further, the necessity to vary the OD of the tubing resulted in fluid leakage from both the pressure junctions and the microfluidic chip during testing, even when methods of prevention such as tubing sleeves [89] were used. Thus, appropriate testing of the effect of w_t would best be done by: 1) manufacturing/designing a new pressure junction(s) to allow each OD of the tubing to be connected without leakage, 2) varying microfluidic chip design to allow each possible OD without leakage, 3) using custom tubing and/or junctions to ensure the microfluidic junction channel ID is on a similar scale to the ID of the sample tubing. Given the complexity and involvement required in these proposed tests, the effect of varying w_t on the dynamic pressure response across the sample tubing was deemed out of scope for the current investigation.

Fluid

Silicone oil was selected as the working fluid for these experiments as it is typically used as the continuous phase fluid in operation of the PDMFCS [35, 36, 43], and different viscosity silicone oil is readily available to purchase. All fluid was purchased from Sigma-Aldrich [90], the fluid properties are presented in Table 3.4 below.

Table 3.4: Properties of silicone oil used in experiments, all properties measured by the manufacturer [87] at 25°C.

ν [cSt]	ρ [$\frac{\text{kg}}{\text{m}^3}$]	$\mu \cdot 10^3$ [Pa · s]
5	913	4.57
10	930	9.30
20	950	19.0
50	960	48.0
100	960	96.0

For experimental cases evaluating variation of P_A , P_{off} , and $\frac{L}{D_i}$, 50 cSt Silicone oil was used. Evaluation of E used 5 cSt Silicone oil to try and compensate for increased pressure losses due to the decreased ID of the tubing.

Requested Pressure Wave Amplitude and Offset

The pressure sinewave requested from the pump (3.1) is physically constrained by the fact that the pump used in the experiments (MFCS-EZ) cannot produce a negative (vacuum) pressure, i.e. a pressure below atmospheric, and thus pressure wave oscillations must occur over a positive (greater than atmospheric) pressure offset. It was necessary to investigate the effect of increasing P_{off} on the FR, in order to understand how higher pressures may affect the transient pressure response. Further, the effect of increasing P_A needed to be investigated for two primary reasons. First, the input pressure wave is attenuated as it travels through the experimental setup, an observation also noted in [56], so it was practically important to determine an appropriate P_{off} and P_A to ensure the inlet and outlet sample tubing pressure waves are measurable. Second, given that the pressure wave attenuates as it moves through the system, it was necessary to examine whether the degree of this attenuation affected the pressure transient dynamics across the sample tubing, i.e. it was necessary to determine if the pressure transient dynamics across the sample tubing is amplitude dependent.

The amplitude dependency was the first tested parameter variation to evaluate if any change to the experimental plan/setup/analysis needed to be performed, where for a constant P_{off} set to 200 mbar, amplitudes summarised in Table 3.5 below were evaluated.

Table 3.5: Input pressure amplitudes considered with constant $P_{\text{off}} = 200$ mbar.

P_A [mbar]
$0.05P_{\text{off}}$
$0.1P_{\text{off}}$
$0.15P_{\text{off}}$
$0.25P_{\text{off}}$
$0.3P_{\text{off}}$

For the offset dependency, P_A was held constant at $0.25P_{\text{off}}$, for the pressure offsets considered in Table 3.6 below.

Table 3.6: Input pressure offsets considered with constant $P_A = 0.25P_{\text{off}}$.

P_{off} [mbar]
50
100
150
200
250

For all tests focused only on varying tubing or fluid properties, P_{off} was set to 100 mbar, and P_A was set to $0.25P_{\text{off}}$ (25 mbar). Note that this method of testing the dependency of the response was inspired by the procedure for experimentally determining the FR of microfluidic pressure pumps in [56].

Requested Pressure Wave Frequency

For each experimental case, input and output pressure waves, determined from the request specified by (3.1), were measured at 19 different frequencies over a frequency range of 0.01 to 0.4 Hz inclusive. This frequency range was determined from analyzing the results of preliminary tests, with the experimental setup described in Figure 3.2 in Section 3.2.1 and sending a pressure wave through the system at different frequencies, where approximate locations of corner frequencies necessary to approximate a TF model from the experimental FR of the pressure dynamics were found to be within this range. Further, prior dynamic studies of the MFCS-EZ [35, 56], have shown that the pump output only slightly attenuates input signals at the upper bound of this frequency range. Nineteen specific frequencies points were selected to provide sufficient resolution to approximate a TF model from the experimental FR, which again was determined from preliminary testing. The specific frequency points considered were 0.01, 0.02, 0.03, 0.04, 0.05, 0.06, 0.07, 0.08, 0.09, 0.1, 0.2, 0.22, 0.25, 0.28, 0.3, 0.32, 0.35, 0.38, and 0.4 Hz.

Microfluidic Chip

For the tests, the downstream microfluidic chip had a standard T-junction design. The chip design was kept constant throughout a given experimental parameter variation case to ensure consistency in the results. Chips were manufactured using PDMS and soft lithography [91]. Experimental cases considering the variation in P_A , P_{off} , $\frac{L}{D_i}$, μ used the chip dimensions specified in Figure 3.5 a). While the experimental case considering the

variation in E used the chip dimensions specified in Figure 3.5 b). Due to the master mold of the chip specified in Figure 3.5 a) breaking during the initial testing of E , a different master mold was used for the chip for testing the effect of E due to time constraints. This was deemed a reasonable decision since in the context of the objectives of this study it is only important that the chip design remain the same for a given experimental case determining the dynamic effect of changing the value of a given parameter, not between experimental cases that differ in the parameter effect they are investigating.

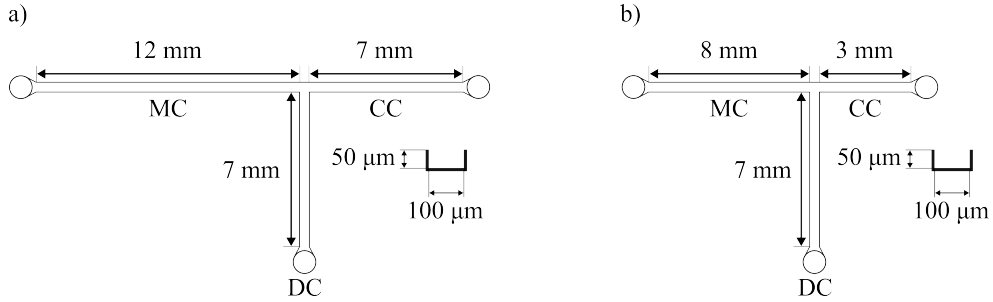


Figure 3.5: Microfluidic chip designs used in experiments. a) Chip design used for experimental cases evaluating effect of varying P_A , P_{off} , $\frac{L}{D_i}$, and μ . b) Chip design used for experimental case evaluating effect of varying E . MC, DC, CC, stand for Measurement Channel, Disperse Channel, and Continuous Channel respectively, see Section 3.2.1 and Figure 3.3. All chips have a channel depth (into the page) of $50 \mu\text{m}$ and a channel width of $100 \mu\text{m}$.

3.2.3 Other Practical Considerations

Analog Measurement and Digital Data Acquisition

The pressure sensors output being an analog voltage, and the necessity to sample this voltage with a DAQ for digital storage and analysis had two very important practical considerations for the experiments. First, since the digitized measurement from the pressure sensors is output as a voltage, it was necessary to statically calibrate [64] the sensors and DAQ setup to relate the measured voltage to a pressure, the method and results of this calibration are presented in Appendix B. Next, measurements of input and output transients depend on the measurements being taken simultaneously, i.e. samples of measurements at both the input and output beginning at the same time. Ideally, a simultaneous sampling device should be used, but the NI USB-6003 DAQ is only capable of multiplexed sampling [92]. However, given that the convert clock operates on the order of nanoseconds, the

aggregate channel sample rate (2 kHz) is way below the maximum aggregate sample rate (100 kHz) [78], and the pressure transient dynamics were found to be within the range of 0.01 to 0.4 Hz, it was considered reasonable to approximate the digital measurements obtained from each DAQ channel as simultaneous. Since the major pressure transient dynamics occur at a timescale much greater than the limiting timescale of the convert clock of the DAQ used in this study, so the nanosecond difference between samples on the input and output measurements would have a negligible affect on the FR analysis.

Pressure Sensor Junctions

In order to use the pressure sensors within the microfluidic setup specialized junctions needed to be designed and manufactured. These junctions were designed to: 1) attempt to limit the sensor/junctions effect on the internal flow in the sample tubing and be leak-proof, 2) preserve a small length-to-diameter ratio for the vertical tap to minimize the time for a change in pressure to be sensed by the sensor [68], and 3) allow for both the pressure sensors and sample tubing of various geometry to be connected to the junctions. A sketch of the cross section of the junction design is presented in Figure 3.6 below. Detailed drawings of these junction designs can be found in Appendix C. Note that IDEX F-333N fittings for 1/16 in OD tubing [93] were used to connect the sample tubing to the junctions, which allowed for various types of sample tubing to be used with the junctions. As well, PTFE plumbers tape [94] was wrapped around the threads of the pressure sensors to leak proof the junction-sensor connection.

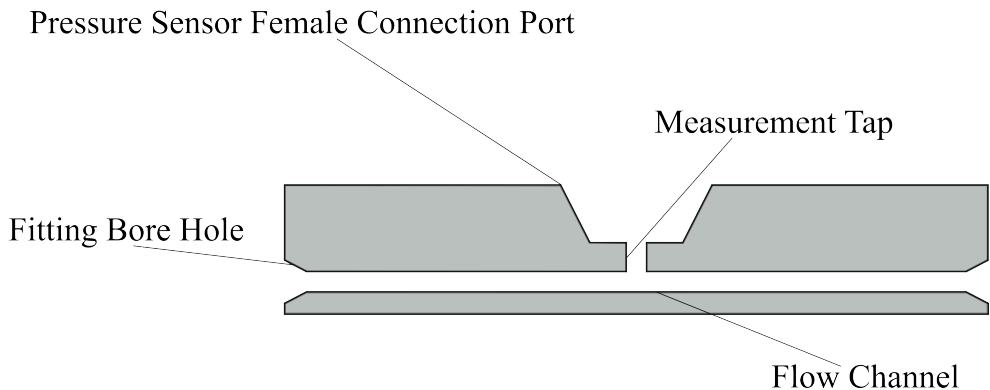


Figure 3.6: Sketch of cross-section of junction used to implement pressure sensors. Flow channel is the channel through which the working fluid is transported through the measurement setup.

Inherently, the junctions affect the flow due to the presence of the vertical pressure tap necessary for the sensors to measure pressure, but given the necessity of this tap for pressure measurement it cannot be avoided. The design of this tap can affect the transient time for the pressure sensor to sense a change in the actual pressure in the fluid. Preserving a small length-to-diameter ratio of this tap helps to reduce the transient time between the pressure change and the sensing of said change, and this relationship was considered in the junction design. Further, it should be noted that the expansion from the small ID of the junction channel to the large pressure sensing cavity, although screwed flush to the tap, may also affect this pressure transient, but typical modelling neglects this [68, 64]. The expansion effect could be avoided by buying a pressure sensor on a similar scale to the microfluidic tubing considered, but available microfluidic pressure sensors did not have the appropriate input range, dynamic response, or accuracy deemed necessary for this investigation. Regardless, it was pertinent to dynamically characterize the junction-sensor apparatus experimentally to determine if the presence of these junctions would have any effect on the FR measurements [68]. The experimental method and in depth results of this characterization can be found in Appendix B, where the primary result was that the junctions would not unnecessarily attenuate or phase shift the input and output sinewaves over the frequency range considered in this experiment [0.01-0.4 Hz], assuming minor losses in the measurement connections are very small.

The use of fittings and the difference in ID between the junction channel and the sample tubing inevitably causes minor losses in the flow, these losses are further compounded by the fact that the flow of the working fluid is laminar [95, 96]. Losses due to the sudden expansion and contraction of the flow diameter are the most significant. Expansion/contraction losses become negligible as the ratio of the small and large diameter approaches unity. Also, expansion losses are greater than contraction losses for a given diameter ratio. Unfortunately, the smallest possible ID that could be machined for the junctions was 1.016 mm (0.04 inches) and the largest microfluidic tubing ID available for purchase, with a 1/16 in OD, was 763 μm . For the majority of tests in which 763 μm ID tubing was used, the diameter ratio was 0.75, indicating that expansion and contraction losses would be present. Given that this ratio is close to one, it is reasonable to assume that these losses will effect the quantitative value of the experimental FR and estimated TF parameters, but the order of magnitude of the experimental FR and the estimated parameters will not be greatly affected [73, 96]. However, for the experimental case where E is varied, the ID of the sample tubing is 254 μm which gives a diameter ratio of 0.25, which will result in significant losses. These losses are important to consider in interpreting the results as an increase in the pressure loss would result in a decrease in the velocity of the fluid flow, which implies that longer pressure transients would be measured in the setup,

than what would actually be present in the sample tubing without any sensing apparatuses connected. The qualitative understanding of these losses was used for interpretation of experimental results, but no quantitative assessment of the losses on the transient pressure measurements was determined through either experimentation or simulation as this was deemed outside the scope of this study. Though, a method of quantifying these losses may be useful in order to produce more accurate TF models from experimental dynamic data for use in an actual PDMFCS application, if the losses over a given tubing-junction connection are deemed significant and no variation to the experimental setup can be made.

Continuous and Disperse Channel Connections

For the continuous and disperse channel connections, the tubing connection setup and their placement relative to the measurement channel in the experimental setup is shown in Figure 3.7. Continuous and disperse channel tubing lengths were kept constant over all experimental tests, the values are presented in Table 3.7. The continuous and disperse channel used the same tubing as the measurement channel for a given test. The lengths of the tubing used in these channels were based solely on practically implementing the experimental setup.

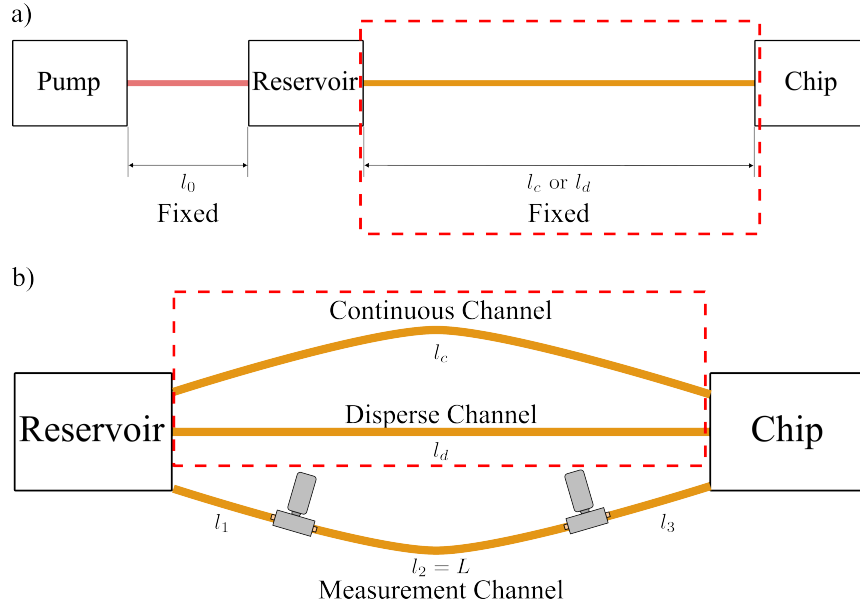


Figure 3.7: a) Visualization of lengths of tubing in experimental apparatus for continuous and disperse channel. b) Orientation of continuous, disperse, and measured channels in experimental setup, air tubing connection not shown. Note that the red box represents the set containing the continuous and disperse channel tubing.

Table 3.7: Lengths of tubing used for continuous and disperse channels.

$l_0 \pm 0.5$ [mm]	$l_c \pm 0.5$ [mm]	$l_d \pm 0.5$ [mm]
214	560	550

3.3 Data Analysis

In the following discussion, 'steady-state' refers to the state of the dynamic response of a stable LTI system at which sufficient time has passed such that the transients associated with the poles present in the systems response to a sinusoidal input signal have died [51]. Not the assumption of steady-state flow, as was discussed in Chapter 2. Note that the method of estimating the FR was also used by Wong in his characterization of the pressure pump [37]. All analysis was automated using Python and Matlab code, see Appendix D.

3.3.1 Pressure Wave Amplitude and Phase Estimation

At steady-state, each input and output pressure wave for a specific frequency was modeled as a general sinewave of the form [97]

$$p(t) = A_p \sin(\omega t + \phi_p) + m = A_p \cos(\phi_p) \sin(\omega t) + A_p \sin(\phi_p) \cos(\omega t) + m \quad (3.6)$$

Where A_p is the amplitude of the sinewave, ϕ_p is the phase of the wave [rad], ω is the frequency [rad/s], t is the time [s], and m is the offset [mbar]. For a given test case, pressure waves within the frequency range of interest are being sent at a constant ω and m , and at steady-state A_p and ϕ_p are constant. Thus, (3.6) can be rewritten as

$$p(t) = \alpha_0 \sin(\omega t) + \alpha_1 \cos(\omega t) + \alpha_2 \quad (3.7)$$

Where, $\alpha_0 = A_p \cos(\phi_p)$, $\alpha_1 = A_p \sin(\phi_p)$, and $\alpha_2 = m$. It can be shown that

$$A_p = \sqrt{\alpha_0^2 + \alpha_1^2} \quad (3.8)$$

and

$$\phi_p = \tan^{-1}\left(\frac{\alpha_1}{\alpha_0}\right) \quad (3.9)$$

The measured pressure data for a given steady-state sinusoidal pressure wave at some time t_i was assumed to be

$$p_m(t_i) = p(t_i) + \epsilon_i = \alpha_0 \sin(\omega t_i) + \alpha_1 \cos(\omega t_i) + \alpha_2 + \epsilon_i \quad (3.10)$$

Where $\epsilon_i \sim N(0, \sigma^2)$ is the error in the measurement at time t_i . Thus, the set of measurements of a steady-state pressure wave from some initial time t_1 to some final time t_N can be written in a general linear model (GLM) form [98] as

$$\mathbf{p}_m = \mathbf{X}_{p_m} \boldsymbol{\alpha} + \boldsymbol{\epsilon} \quad (3.11)$$

Which in expanded form is

$$\begin{bmatrix} p_m(t_1) \\ \vdots \\ p_m(t_N) \end{bmatrix} = \begin{bmatrix} \sin(\omega t_1) & \cos(\omega t_1) & 1 \\ \vdots & \vdots & \vdots \\ \sin(\omega t_N) & \cos(\omega t_N) & 1 \end{bmatrix} \begin{bmatrix} \alpha_0 \\ \alpha_1 \\ \alpha_2 \end{bmatrix} + \begin{bmatrix} \epsilon_1 \\ \vdots \\ \epsilon_N \end{bmatrix}$$

Assuming each $\epsilon_i \sim N(0, \sigma^2)$ to be independent and identically distributed, the estimate of $\boldsymbol{\alpha}$ can be calculated using ordinary least squares (OLS) estimation. Where this estimate is given by [99]

$$\hat{\boldsymbol{\alpha}} = (\mathbf{X}_{p_m}^T \mathbf{X}_{p_m})^{-1} \mathbf{X}_{p_m}^T \mathbf{p}_m \quad (3.12)$$

From determination of $\hat{\boldsymbol{\alpha}}$, (3.12), the amplitude and phase of the measured steady-state pressure wave at a given frequency, over the considered interval $[t_1, t_N]$, can be estimated using (3.8) and (3.9) where

$$\hat{A}_p = \sqrt{\hat{\alpha}_0^2 + \hat{\alpha}_1^2} \quad (3.13)$$

and

$$\hat{\phi}_p = \tan^{-1}\left(\frac{\hat{\alpha}_1}{\hat{\alpha}_0}\right) \quad (3.14)$$

This process is repeated for each input and output pressure wave measurements over the set of input pressure wave frequencies for each test case within a given experimental case. Note that this method of estimating the sinewave parameters was also used by Wong in his FR characterization of the pressure pump [37].

3.3.2 Determination of Magnitude and Phase Frequency Response

By considering measurements of the steady-state input and output pressure waves at a given frequency over a common interval $[t_0, t_N]$ and estimating the amplitude and phase of both waves using the method described in Section 3.3.1, the magnitude and phase FR of the system at a specific frequency are determined by

$$|G_p(j\omega)| = \frac{\hat{A}_{p_4}(\omega)}{\hat{A}_{p_3}(\omega)} \quad (3.15)$$

for the magnitude FR, and

$$\angle G_p(j\omega) = \hat{\phi}_{p_4}(\omega) - \hat{\phi}_{p_3}(\omega) \quad (3.16)$$

for the phase FR. Where p_3 and p_4 represent the pressure wave at the inlet and outlet of the sample tubing respectively. The $\hat{}$ symbol is dropped for the magnitude and phase FR, (3.15) and (3.16) for simplicity of notation, although they are inherently estimates of the true magnitude and phase FR of the system.

For a given test case, determining the magnitude and phase FR, (3.15) and (3.16), over the frequency range of interest, and then plotting the FR over this frequency range on a Bode diagram [49, 51, 100] provides the experimental FR of the system. From which, an estimate of the TF of the system was determined. Note that for plotting the FR, the magnitude FR was converted to Decibels [dB] where

$$|G_p(j\omega)|_{\text{dB}} = 20\log_{10}(|G_p(j\omega)|) \quad (3.17)$$

and the phase FR was converted to degrees [$^\circ$] using

$$\angle G_p(j\omega)_{\text{deg}} = \angle G_p(j\omega) \frac{180^\circ}{\pi} \quad (3.18)$$

Where for the remainder of this document $|G_p(j\omega)|$ will refer to $|G_p(j\omega)|_{\text{dB}}$ and $\angle G_p(j\omega)$ will refer to $\angle G_p(j\omega)_{\text{deg}}$ unless otherwise noted.

3.3.3 Estimation of Transfer Function From Experimental Frequency Response

With determination of the experimental FR over the frequency range of interest, a TF estimate was obtained by fitting a simulated TF FR over the experimental FR data from the Bode plot, through use of MATLAB's `tf()` [101] and `bode()` [102] functions. Also, from this estimated TF, the system model's response to a step input was simulated using MATLAB's `step()` [103] function, the time constant was evaluated as the time for the output to reach 63% of the input value [49, 51] using MATLAB's `stepinfo()` function [104]. This was repeated for all tests within a given experimental case.

3.3.4 Uncertainty

All experimental results and parameters determined from said results are presented at the 95% confidence level [64]. This section summarizes the general methodology for the uncertainty calculations.

Parameter Uncertainty

The initial uncertainty from which all corresponding uncertainties propagate is the uncertainty in the estimate of the pressure sinewave parameters. Considering the measurements of the pressure wave, assumed to come from a general sinewave model, presented in GLM form with $\epsilon \sim \mathbf{N}(\mathbf{0}, \sigma^2 \mathbf{I}_{\text{ident}})$ as in (3.11), the estimate of the variance in the measurement error is given by [99]

$$\hat{\sigma}^2 = \frac{\mathbf{p}_m^T (\mathbf{I}_{\text{ident}} - \mathbf{P}_{\mathbf{x}_{\mathbf{p}_m}}) \mathbf{p}_m}{n - r} \quad (3.19)$$

Where $\mathbf{P}_{\mathbf{x}_{\mathbf{p}_m}} = \mathbf{X}_{\mathbf{p}_m} (\mathbf{X}_{\mathbf{p}_m}^T \mathbf{X}_{\mathbf{p}_m})^{-1} \mathbf{X}_{\mathbf{p}_m}^T$, $n = \text{rank}(\mathbf{I}_{\text{ident}})$, and $r = \text{rank}(\mathbf{X}_{\mathbf{p}_m})$. From (3.19), the estimate of the covariance matrix of the parameter vector estimate can be calculated using

$$\widehat{\text{cov}}(\hat{\boldsymbol{\alpha}}) = \hat{\sigma}^2 (\mathbf{X}_{\mathbf{p}_m}^T \mathbf{X}_{\mathbf{p}_m})^{-1} \quad (3.20)$$

Where the estimated variance of each parameter estimate is along the diagonal of the estimated covariance matrix. The uncertainty in the parameter estimate at the 95% confidence interval is then calculated using

$$\Delta u_{\hat{\alpha}_i} = \pm t_{\text{val}_{n-r, 1-0.05/2}} \sqrt{\widehat{\text{var}}(\hat{\alpha}_i)} \quad (3.21)$$

Where, $t_{\text{val}_{n-r, 1-0.05/2}}$ is the t-value test statistic with $n - r$ degrees of freedoms at a two-sided 95% confidence level [105].

Uncertainty Propagation

From determining the uncertainty in the estimated sinewave parameters using (3.21), the uncertainty in the experimental FR magnitude and phase was calculated using standard

propagation of uncertainty techniques [64, 65, 105]. Where for a calculated parameter, y , that is a function of experimental measurements and/or parameters, x_i , as in

$$y = f(x_i, \dots, x_N) \quad (3.22)$$

The uncertainty associated with y is estimated as

$$\Delta u_y \approx \sqrt{\sum_{i=1}^N \left(\frac{\delta y}{\delta x_i} \Delta u_{x_i}\right)^2} \quad (3.23)$$

Where, Δu_{x_i} is the uncertainty associated with each x_i .

Sequential Perturbation

For the parameters of the estimated TF used to model the experimental FR, there is no analytic equation relating the estimated TF parameters to the experimental FR. Instead, the TF parameters were estimated from graphical interpretation of the experimental FR. Thus, $\frac{\delta y}{\delta x_i} \Delta u_{x_i}$ needed to be estimated. So, to calculate the uncertainty in the estimated TF parameters sequential perturbation was used [65]. Where $\frac{\delta y}{\delta x_i} \Delta u_{x_i}$ was estimated as

$$\frac{\delta y}{\delta x_i} \Delta u_{x_i} \approx \frac{|y(x_i^+) - y(x_i)| + |y(x_i^-) - y(x_i)|}{2} \quad (3.24)$$

With x_i^+ and x_i^- representing the upper and lower uncertainty bound of a given x_i . By obtaining the parameters associated with fitting the estimated TF to the upper and lower uncertainty bounds of the experimental FR, (3.24) was utilized to estimate the uncertainty in the TF parameters. This method was also used to obtain the uncertainty in the transient characteristic of the TF models simulated step response.

3.4 HECM Model Analysis

3.4.1 HECM Primary Model Form

The HECM was used to model the sample tubing dynamics, as was done in previous PDMFCS studies [35, 36, 43]. A symmetric circuit formulation was the primary form of

the HECM considered for the sample tubing pressure transient dynamics, see Figure 3.8, to account for the continuous nature of the viscous and inertial losses both before and after the losses associated with compliance effects [59]. See also Figure 2.1 in Section 2.2. Ground of the circuit is considered atmospheric pressure.

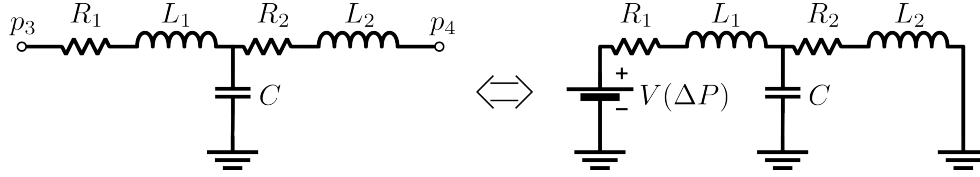


Figure 3.8: Symmetric HECM of sample tubing used for comparison to experimental results.

3.4.2 Transfer Function Determination

In the HECM the slowest component transient response can be considered to model the time it takes for the pressure field within the sample tubing to reach a hydrodynamic steady-state. This response was assessed by deriving TF's for the different circuit components, considering the pressure drop across the component ($\Delta P_{\text{component}} = V_{\text{component}}$) as the output and the pressure drop across the sample tubing as the input ($\Delta P = V$). The TF's of the different components in the circuit can be derived from Kirchoff's voltage and current laws, with $R_1 = R_2 = R/2$ and $L_1 = L_2 = L_{\text{hyd}}/2$. See Appendix E for the details of said derivation, where the resulting TF's are given by

$$G_{R_1}(s) = \frac{V_{R_1}(s)}{V(s)} = \frac{R(CL_{\text{hyd}}s^2 + CRs + 2)}{(L_{\text{hyd}}s + R)(CL_{\text{hyd}}s^2 + CRs + 4)} \quad (3.25)$$

$$G_{R_2}(s) = \frac{V_{R_2}(s)}{V(s)} = \frac{2R}{(L_{\text{hyd}}s + R)(CL_{\text{hyd}}s^2 + CRs + 4)} \quad (3.26)$$

$$G_{L_1}(s) = \frac{V_{L_1}(s)}{V(s)} = \frac{L_{\text{hyd}}s(CL_{\text{hyd}}s^2 + CRs + 2)}{(L_{\text{hyd}}s + R)(CL_{\text{hyd}}s^2 + CRs + 4)} \quad (3.27)$$

$$G_{L_2}(s) = \frac{V_{L_2}(s)}{V(s)} = \frac{2L_{\text{hyd}}s}{(L_{\text{hyd}}s + R)(CL_{\text{hyd}}s^2 + CRs + 4)} \quad (3.28)$$

$$G_C(s) = \frac{V_C(s)}{V(s)} = \frac{2}{CL_{\text{hyd}}s^2 + CRs + 4} \quad (3.29)$$

$G_R(s)$ (3.25, 3.26), $G_L(s)$ (3.27, 3.28), and $G_C(s)$ (3.29) represent the transient pressure field dynamics associated with the fluid overcoming viscous, inertial, and compliance effects with a sudden change in the pressure drop across the sample tubing respectively. As these responses happen simultaneously in the HECM, the slowest transient response is considered to model the time it takes for the fluid within the sample tubing to reach hydrodynamic steady-state. Values of hydrodynamic resistance, R , and inductance, L_{hyd} , were calculated using (2.1) and (2.2). Hydrodynamic capacitance, C , values were evaluated using the general formulation (2.3), while also considering the tubing compliance for thin and thick wall tubes, (2.4) and (2.5) respectively.

Since the silicone oil manufacturer/supplier did not have data for the adiabatic bulk modulus, β_a was assumed to be equal to 1.7237 GPa, which is a typical bulk modulus value for hydraulic oils [106]. Further, since the tubing manufacturer/supplier did not have data for E_{tens} this value was estimated from other suppliers data sheets, which varied depending on the tubing material, see Table 3.8 below.

Table 3.8: Estimated values of E_{tens} for tubing materials considered in experiments from other manufacturers/suppliers. Used in HECM parameter calculations.

Material	E_{tens} [GPa]	Source
FEP	0.346	[107, 108]
HPPFA	0.451	[109]
Tefzel ETFE	0.965	[110]
PEEK	1.10	[111]

Evaluation of thick wall capacitance, (2.5), was only performed for FEP tubing, with ν_p estimated as 0.48 [112].

3.4.3 Comparison of Experimental and HECM Dynamic Response

Difference in HECM and Experimental Transfer Functions and Signals

The TF's derived from the HECM approximate the dynamic response of the pressure drop associated with viscous, inertial, and compliance effects with an arbitrary change in

the total pressure drop across the sample tubing. Meanwhile, the TF's estimated from the experimental FR's model the dynamic response of the sample tubing output pressure signal with an arbitrary change of the input pressure signal. Thus, the analytic and experimental models are slightly different in the input and output signals considered. This may cause the HECM component TF's to differ in model and transient/frequency response form from the experimentally estimated TF's, depending on the complexity of the circuit considered.

Comparing the HECM and Experimental Model

Despite the possible difference in form of the TF and associated transient/frequency response between the HECM and experimentally estimated TF's, the models are similar in that they both characterize the step response associated with a change in pressure, i.e. the time for the fluid in the system to reach hydrodynamic steady-state. Thus, for the HECM to be an appropriate model of the sample tubing pressure dynamics, the HECM component TF with the slowest step response should have a step response on a similar timescale to that of the experimentally estimated TF for the same tubing/fluid parameters. That is, the HECM component with the slowest step response should approximate a similar timescale for the fluid to reach hydrodynamic steady-state as the experimentally estimated TF. As such, it was deemed most appropriate to determine the validity of the HECM in approximating the pressure transient response across the sample tubing by comparing the quantitative timescale of the HECM component TF's step response characteristics to the quantitative timescale of the experimentally estimated TF's step response characteristics. Also, the change in the HECM quantitative step response characteristics timescale with variation in tubing/fluid parameters was assessed and compared to the variation in timescale with change in parameters associated with the experimentally estimated TF's.

Quantifying Step Response Characteristics

Quantitative step response characteristics were evaluated depending on the order of the TF model under consideration. For first-order models the step response is characterized by its time constant, τ , that is the time for the output signal to reach 63% of its steady-state value. For the higher order models, the defining step response characteristic was settling time (T_s), the time required for the output transient damped oscillations to reach and remain within ± 0.02 of the output steady-state value [39, 49, 51]. T_s was used as the main assessment of the time for the fluid to reach hydrodynamic steady-state. Timing

characteristics of the different TF's were assessed and set using MATLAB's `stepinfo()` function [104].

Comparison of HECM and Experimental FR

Even though the input-output signals for the HECM components differ from the input-output signals for the experimental FR (pressure drops vs gauge pressures), it is still useful to assess the frequency domain performance of the HECM as opposed to the experimental FR. The components in the HECM may not have FR's equivalent to that found in the experiments due to the differing input-output signals and the fact that each component TF is a characterization of the dynamics associated with specific fluid phenomena in the tubing as opposed to the pressure transient dynamics across the whole tubing. Regardless of FR form, if the HECM were to be a suitable model, it is expected that the corner frequencies of the FR are comparable to that found in experiment. To compare the FR's, Bode plots of the HECM components were determined using MATLAB's `bode()` function [102], ensuring that the Bode plots encompassed the frequency range of the experimental FR [0.01,0.4] Hz.

3.4.4 Lower Order HECM Model Forms

Given that the symmetric form of the HECM produces TF's of a relatively high-order, simpler versions of the HECM were also considered to see if lower-order models could capture similar transient/frequency responses as the experimentally estimated TF's. All TF's were derived and parameters were calculated using the same methods as described in Section 3.4.2, where the TF derivations are given in more detail in Appendix E. Transient and frequency response characteristics were determined using MATLAB.

Second-Order HECM

The second-order HECM, Figure 3.9, was implemented in Wong et al.'s PDMFCS studies [35, 36]. One may interpret this form as modelling a case where the losses are discontinuous, that is some of the flow experiences inertial losses and other parts of the flow experience compliance losses, rather than a continuous application of both types of losses along the tubing [59].

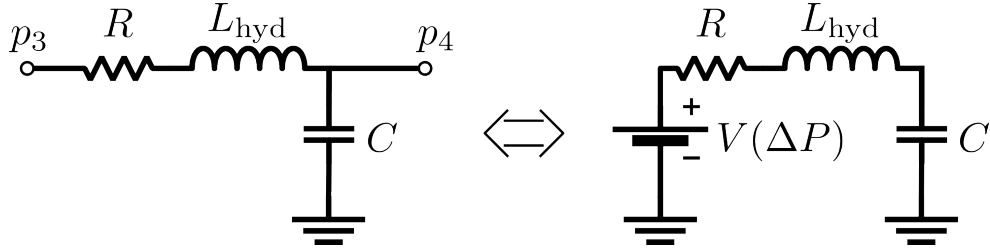


Figure 3.9: Second-order HECM of sample tubing used for comparison to experimental results

The dynamic characteristics of this circuit are dominated by the inertial and compliance components, the TF's of which are given by

$$G_L(s) = \frac{V_L(s)}{V(s)} = \frac{L_{\text{hyd}}Cs^2}{L_{\text{hyd}}Cs^2 + RCs + 1} = \frac{s^2}{s^2 + \frac{R}{L_{\text{hyd}}}s + \frac{1}{L_{\text{hyd}}C}} \quad (3.30)$$

$$G_C(s) = \frac{V_C(s)}{V(s)} = \frac{1}{L_{\text{hyd}}Cs^2 + RCs + 1} = \frac{\frac{1}{L_{\text{hyd}}C}}{s^2 + \frac{R}{L_{\text{hyd}}}s + \frac{1}{L_{\text{hyd}}C}} \quad (3.31)$$

First-Order HECM

There are two ways to model the first-order HECM. The first is to neglect the effect of inertial losses, which results in a RC circuit of the form in Figure 3.10 below, where the fluid only experiences viscous and compliance losses.

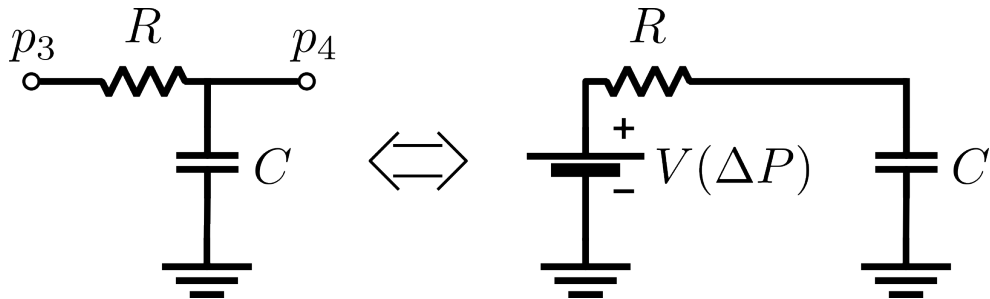


Figure 3.10: First-order RC HECM of sample tubing used for comparison to experimental results

The dynamic characteristics of this circuit are characterized by the TF of the resistive

$$G_R(s) = \frac{V_R(s)}{V(s)} = \frac{RCs}{1 + RCs} \quad (3.32)$$

and compliance component

$$G_C(s) = \frac{V_C(s)}{V(s)} = \frac{1}{1 + RCs} \quad (3.33)$$

The second method of modelling a first-order HECM is by neglecting compliance effects, which results in the RL circuit pictured in Figure 3.11 below

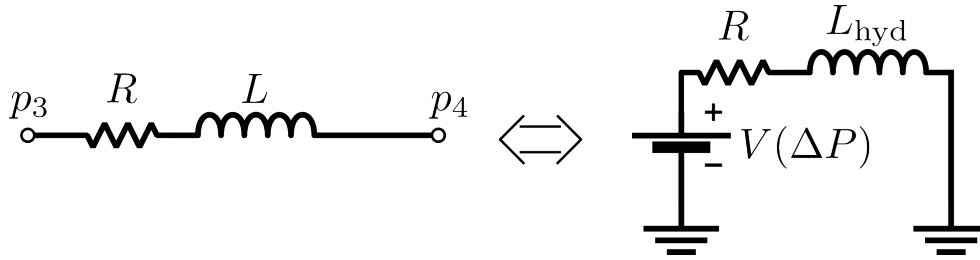


Figure 3.11: First-order RL HECM of sample tubing used for comparison to experimental results

The dynamic characteristics of this circuit are characterized by the TF of the resistive

$$G_R(s) = \frac{V_R(s)}{V(s)} = \frac{1}{1 + \frac{L_{\text{hyd}}}{R}s} \quad (3.34)$$

and inertial component

$$G_L(s) = \frac{V_L(s)}{V(s)} = \frac{\frac{L_{\text{hyd}}}{R}s}{1 + \frac{L_{\text{hyd}}}{R}s} \quad (3.35)$$

3.4.5 Modelling Considerations and Assumptions

In the experiments, the pressure at the outlet of the sample tubing is not exactly atmospheric, due to the presence of the downstream chip, although the disperse channel in

the chip is open to atmosphere. However, considering the pressure differential relative to ground is rational in the HECM for the following reasons. First and most importantly, the HECM is used to assess the dynamic response across the circuit components associated with changing the pressure drop ($\Delta P = p_3 - p_4$) across the tubing, where the value of this pressure drop is arbitrary from a dynamic modelling perspective. Second, if the downstream chip channels were also modelled, this would increase model order, result in the model becoming MIMO, and therefore increase difficulty in analysis all without significantly changing the order of magnitude of the quantitative values of the transient response characteristics, where this magnitude is on the order of milliseconds [22].

Chapter 4

Results and Discussion

This chapter will present and discuss the results obtained using the methodology developed in Chapter 3 to experimentally characterize the pressure transient dynamics across the sample tubing in the PDMFCS plant, followed by a comparison of experimentally determined and HECM predicted dynamic responses. The effectiveness of the experimental setup and procedure at simultaneously measuring the pressure waves, as well as fitting a sinewave model to the measurements is presented in Section 4.1. Section 4.2 details the experimental FR results and the accompanying estimated TF, followed by assessment of the change in dynamic response with variation in the tubing/fluid parameters. Comparison of the dynamic response of the experimentally estimated TF to that of the HECM is found in Section 4.3.

4.1 Experimental Pressure Waves and OLS Fit

With the experimental plan and setup described in Sections 3.1 and 3.2, input and output pressure waves were successfully measured approximately simultaneously along the sample tubing. The beginning section of measurements for input-output pressure waves at a frequency of 0.01 Hz used for FR analysis of a requested pressure wave with $P_{\text{off}} = 150$ mbar and $P_A = 0.25P_{\text{off}}$ are shown in Figure 4.1. The transient fully dissipated at around 400 seconds (~ 7 minutes), after which steady-state pressure waves were measured. Measurements at a given frequency were taken over a time interval of 13-20 minutes, depending on the frequency of the wave, to ensure an adequate number of periods (8-10) of the steady-state pressure waves were within the steady-state measurement region selected for OLS fitting and FR analysis, to decrease the uncertainty in the results.

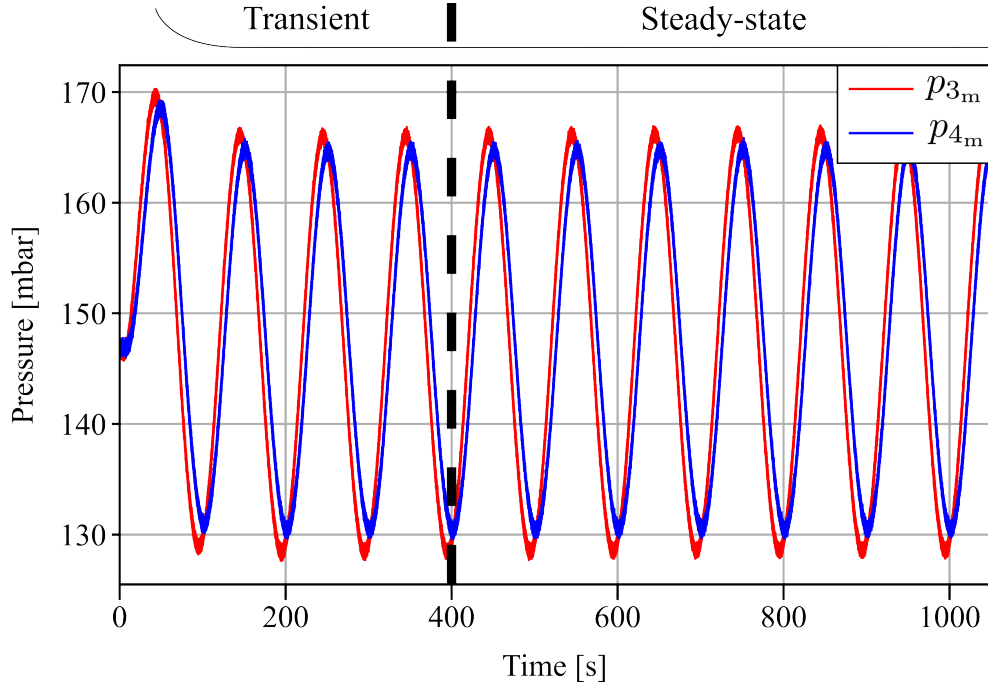


Figure 4.1: Beginning portion of input and output pressure wave measurements with $P_{\text{off}} = 150$ mbar, $P_A = 0.25P_{\text{off}}$, and $f = 0.01$ Hz. Steady-state measurement regions were used for OLS fitting and FR analysis. p_{3_m} and p_{4_m} represent the pressure wave measurements at the inlet and outlet of the sample tubing respectively. Measurement uncertainties are not shown for the purpose of visual clarity.

The OLS estimation method (Section 3.3) provided good fits of the pressure waves at the slowest (0.01 Hz) and fastest (0.4 Hz) considered frequencies. This can be seen from the measured and estimated steady-state pressure waves at the inlet of the sample tubing for the experimental case of $P_{\text{off}} = 150$ mbar, $P_A = 0.25P_{\text{off}}$ for 0.01 and 0.4 Hz shown in Figure 4.2. The values of the estimated parameters with relative uncertainties [105] are presented in Table 4.1.

Notice that the inlet pressure wave attenuation increases as the requested frequency increases. Given that upstream of the inlet pressure sensor there is a relatively significant length of sample tubing connecting the reservoir to the inlet pressure sensor, see Figure 3.4 and Table 3.2 in Section 3.2.2, this behaviour is expected [56]. Where the portion of sample tubing connecting the reservoir to the inlet pressure sensor imposes its own energy loss and dynamic effects on the flow before it reaches the sensing region of the inlet pressure sensor. From the dynamic analysis presented in Section 4.2, it is observed that increasing the

oscillation frequency will result in increased attenuation of the pressure wave as it travels through the tubing. Physically, this attenuation likely stems from the fact that in laminar flow the viscous forces tend to damp high frequency behaviour [73, 113]. The experimental results, presented in Section 4.2, show that the relative flow energy between the outlet and inlet wave (the relative energy loss) dictates the lowest frequency of behaviour that is damped by viscous effects. Examining this behaviour from the perspective of a physical wave travelling through a medium, since the pressure wave loses energy due to friction effects as it travels through the tubing, the wave energy at the outlet is lower than the energy at the inlet. Wave energy is proportional to both amplitude and frequency [114], thus at a constant frequency, wave energy loss through the tubing results in attenuation of the amplitude of the wave as it travels from the inlet to the outlet of the sample tubing. Experimentally, it was observed that the amount of relative energy loss through the tubing increased with frequency due to the tendency for viscous forces in laminar flow to preferentially damp high frequency behaviour [73, 113]. This implies that the increase in the inlet wave energy was negligible in comparison to the increase in energy (frictional) losses through the tube as the frequency of oscillation was increased.

The effect of the attenuation of the inlet pressure wave on the experimental FR of the pressure transients across the sample tubing was investigated by varying P_A , see Section 4.2.2. Also, the noise in the measurement signal becomes more prevalent at higher frequencies, which is expected as electronic noise operates in a high-frequency domain [64]. This noise could be removed from the measurement signal by the addition of a low-pass filter [70], but no such addition was made in these experiments. As a final note, the pressure wave offset differs between the 0.01 Hz and 0.4 Hz wave. This can be attributed to: 1) slight bias error in the pressure sensors, which can be amplified by slight differences in elevation/angle in the sensors during measurement and/or, 2) the Fluigent pumps difficulty in maintaining the offset at increased frequency requests. Regardless, this difference in offset has a negligible effect on the FR analysis, as only the relative amplitudes and phases of the input-output sinewaves are needed.

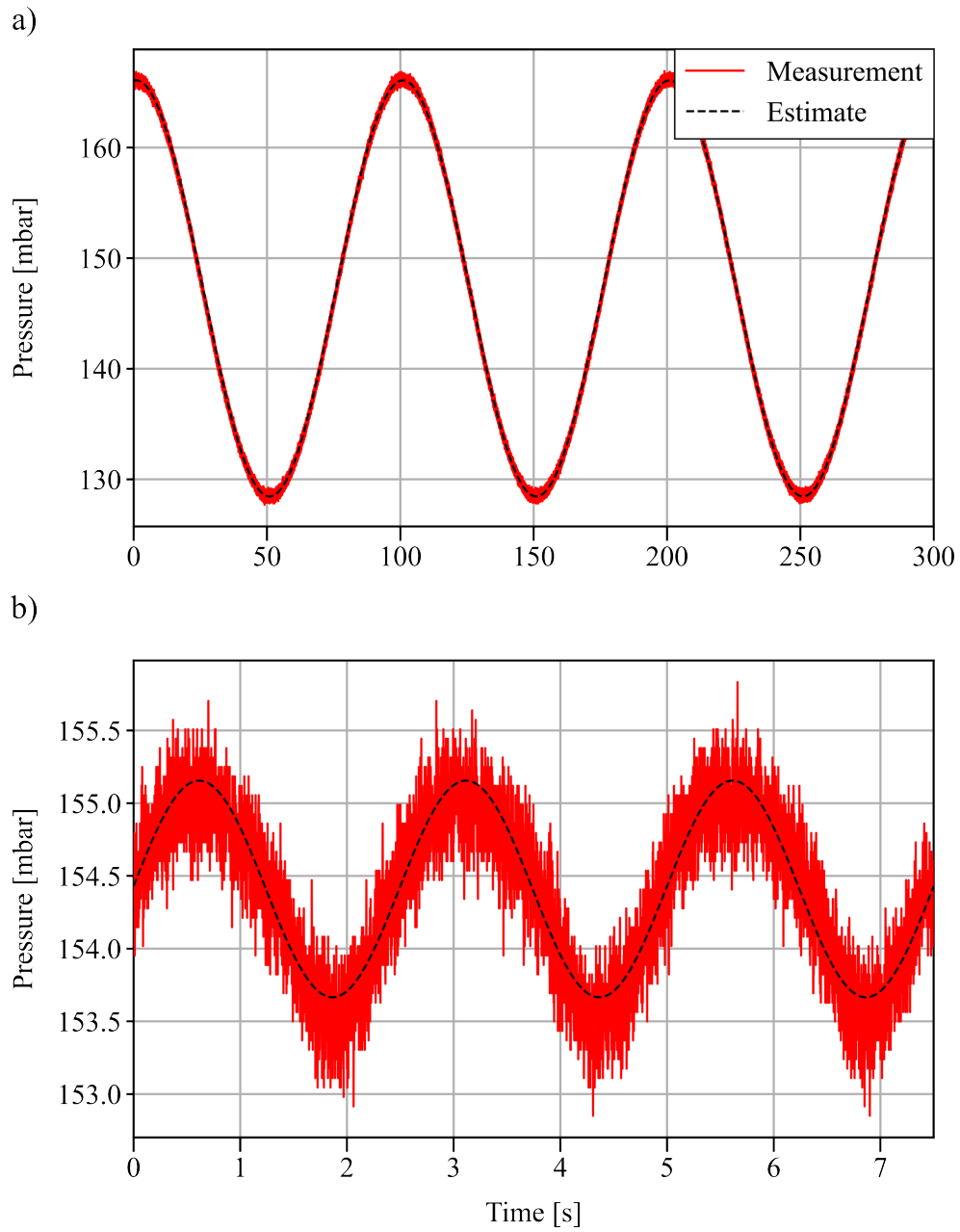


Figure 4.2: Measured and estimated steady-state pressure waves wave measured at the inlet of the sample tubing with $P_{\text{off}} = 150$ mbar and $P_A = 0.25P_{\text{off}}$. a) $f = 0.01$ Hz, b) $f = 0.4$ Hz. Measurement uncertainties are not shown for the purpose of visual clarity.

Table 4.1: Estimated parameters of (3.7) from OLS estimation of input pressure wave for 0.01 and 0.4 Hz frequency cases, with $P_{\text{off}} = 150$ mbar and $P_A = 0.25P_{\text{off}}$. Relative uncertainties shown.

f [Hz]	$\hat{\alpha}_0$ [mbar]	$\hat{\alpha}_1$ [mbar]	$\hat{\alpha}_2$ [mbar]
0.01	$1.15 \pm 0.06\%$	$18.8 \pm 0.004\%$	$148 \pm 0.0003\%$
0.4	$0.745 \pm 0.2\%$	$0.019 \pm 6\%$	$154 \pm 0.0005\%$

4.2 Experimental Frequency Response and Simulated Transient

4.2.1 General Form

The experimental FR for each test in each experimental case had the general form of a first-order system with one zero and a transport lag component. Thus, the estimated TF to model each experimental FR had the form

$$G_p(j\omega) = e^{-d(j\omega)} \frac{1 + a(j\omega)}{1 + b(j\omega)} \quad (4.1)$$

A Bode plot of the experimental FR with the FR of the estimated TF overlapped, for the test considering an input pressure wave of $P_{\text{off}} = 150$ mbar and $P_A = 0.25P_{\text{off}}$, is presented with uncertainties in Figure 4.3. Values of the TF model parameters a , b , and d for this case are presented in Table 4.2. In general, the uncertainties in the magnitude and phase FR were relatively small, but increased in size with increase in frequency. The physical nature of the system and its relationship to this general first-order model form with transport lag component are discussed below.

First-Order System

Given that microfluidic flow is dominated by viscous forces and occurs over a low flow velocity, i.e. laminar flow with $Re \ll 1$, it makes sense that the pressure transient dynamics approximate a first-order model. The negligible effect of inertia coupled with the domination of viscous forces in the flow would result in heavy damping of the system response. For all cases, the magnitude of the zero was much greater than the magnitude of the pole which results in the subsequent tapering in magnitude attenuation at higher frequencies

and slightly faster step response time constants, compared to a first-order system without a zero [49].

Within this study the zero was included in the TF estimation to increase the accuracy in the estimated phase FR fit to the experimental data. While including the zero in the TF estimation resulted in an improved fit of the estimated phase FR to the experimental phase FR, the fact that it occurs at a frequency upwards of 33 times faster than the pole suggests that it may be physically reasonable to neglect it in the TF estimation. Further, prior pressure transient models have shown/assumed the pressure magnitude attenuation to continuously increase with an increase in frequency [44, 58, 68]. Neglecting the zero may result in slight changes in the estimated values of b and d . The perceived presence of the zero in the experimental FR may be a consequence of both the increased attenuation of the pressure waves and the decrease of the signal to noise ratio of the pressure wave measurements at high frequencies, resulting in a worse OLS estimation of the phase of a given wave. Decrease in the signal to noise ratio also increases the uncertainty of the experimental FR and the parameters of the estimated FR. The effect of noise could be minimized through the use of low-pass filters, but no such compensation was performed in these experiments.

Transport Lag

It is physically reasonable and expected that the change in the output pressure wave would lag the change of the input pressure wave. As an input pressure wave propagates through the tubing at the speed of sound in the working fluid, which is finite [68]. Generally, the results showed this transport lag to be very small and almost negligible, which is physically reasonable given the relatively short distance over which the pressure wave travels across the sample tubing in the experiments. Due to the experimental phase FR having larger uncertainty at higher frequencies caused by increased wave attenuation and noise in the measurement signal, it is possible that the true transport delay is slightly different than that found in these analyses.

Transport lag is indicative of a non-minimum phase system, that is a system whose range in phase angle is greater than the minimum phase angle range for all systems with an equivalent magnitude characteristic. Some consequences of non-minimum phase systems in control system design are that the TF must be estimated from both the experimental magnitude and phase FR and that stability analysis is best performed using Nyquist diagrams, as opposed to Bode plot stability assessments using phase and gain margins [51]. As such, careful consideration would have to be made in PDMFCS design on whether or

not to neglect this transport lag component in the model of the sample tubing pressure transient dynamics.

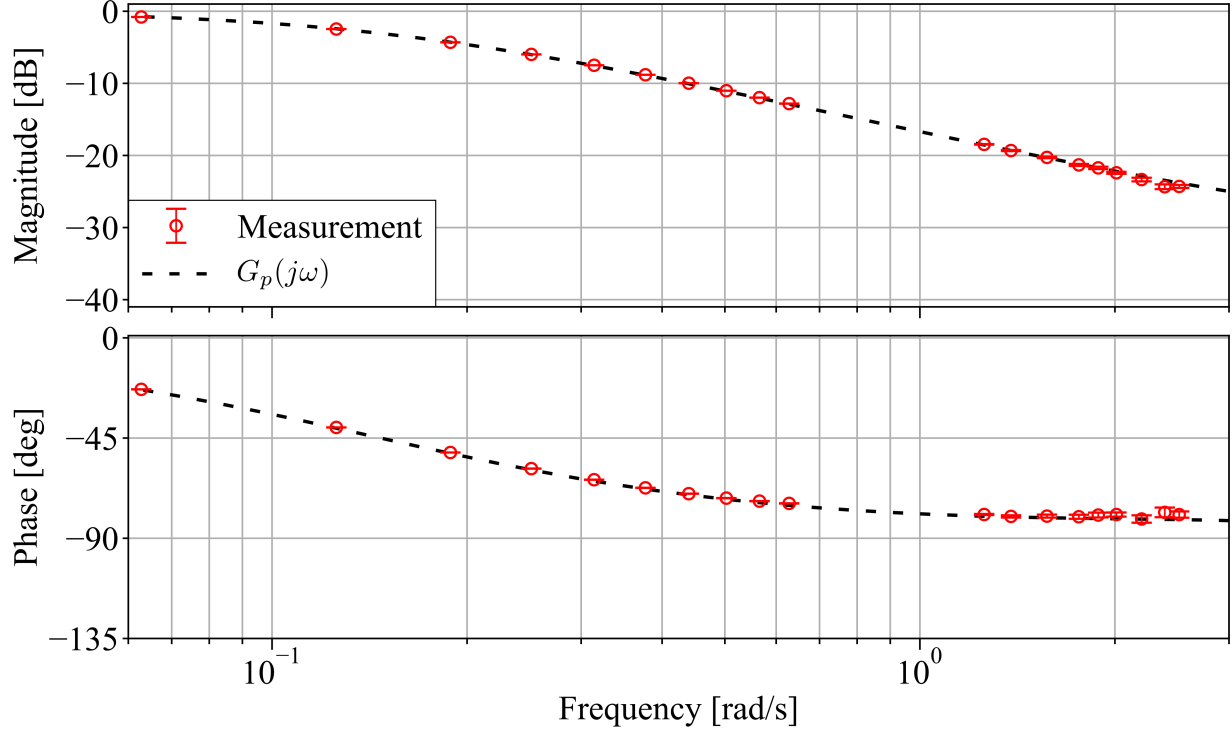


Figure 4.3: Bode plot of FR from experiment and estimated TF for $P_{\text{off}} = 150$ mbar and $P_A = 0.25P_{\text{off}}$.

Table 4.2: Parameters for estimated TF from experimental FR for $P_{\text{off}} = 150$ mbar and $P_A = 0.25P_{\text{off}}$. Relative uncertainties given.

a	b	d
$0.2 \pm 15\%$	$6.9 \pm 1.5\%$	$0.15 \pm 17\%$

4.2.2 Increasing Pressure Amplitude

The pressure transient dynamics across the sample tubing were negligibly affected by the increase in the amplitude of the requested pressure wave (Figure 4.4). Physically, this

would indicate that the pressure wave experiences the same relative attenuation (energy losses) across the tubing regardless of its incoming amplitude. This result is reasonable as these tests considered a constant P_{off} , along with constant tubing and fluid parameters. Which indicates that the mean pressure drop across the tubing was the same over all tests. This would imply the fluid elements, carrying the effect of the change of the input pressure signal, travel through the tubing at approximately the same mean velocity. Where in the steady-state case (3.5), an increase in the pressure drop results in an increase in the flow rate for constant tubing and fluid properties, or an increase of the incoming flow energy (decrease in the relative energy loss across the tubing) [73, 113].

From a dynamic system perspective, since the system does not show any amplitude dependence, the parameter values of the estimated TF were the same for all cases (Table 4.3). The lack of amplitude dependence shows that the system can be approximated as linear since it is obeying the fundamental property of scaling, inherent to the superposition property of linear systems [70]. This indicates that linear control system design and analysis techniques would be applicable to this system [51, 70]. At lower amplitudes, larger TF parameter uncertainties were noted, due to the lower signal to noise ratio of the measurements due to the decreased wave amplitude. The largest relative TF parameter uncertainties are reported in Table 4.3. Note that the relative uncertainties in a and d are much larger than the relative uncertainty in b . This is caused by the increased uncertainty in the experimental FR, due to the decreased pressure wave amplitude and signal to noise ratio, in the relatively higher frequencies that a and d take effect.

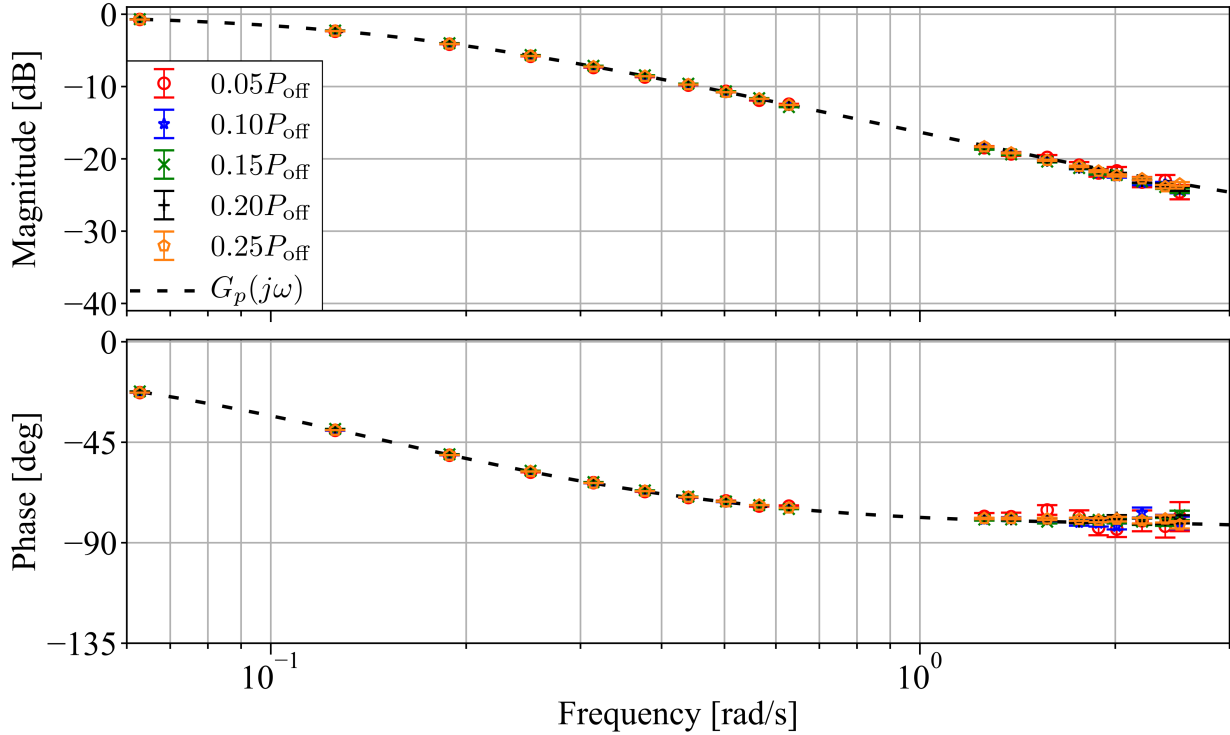


Figure 4.4: Experimental and estimated FR for increasing P_A .

Table 4.3: Parameters for estimated TF from experimental FR's investigating the effect of varying P_A . Relative uncertainties given.

a	b	d
$0.2 \pm 38\%$	$6.6 \pm 3.0\%$	$0.15 \pm 20\%$

4.2.3 Increasing Pressure Offset

Increasing P_{off} primarily resulted in an increase of the corner frequency (Figure 4.5), a decrease in b , and thus a faster step response for the system (Figure 4.6). Physically, this is reasonable as an increase in P_{off} would result in an increase in the mean pressure drop (increase in inlet energy, decrease in relative energy loss) across the tubing, and thus an increase in the mean velocity at which the fluid moves through the system as discussed in Section 4.2.2. Although, the increase in the corner frequencies (decrease in time constants)

with increasing P_{off} is statistically significant, the actual relative difference is rather small unless the pressure is increased significantly (Table 4.4). So, in modelling the sample tubing pressure transient dynamics for a PDMFCS application, it may be reasonable to neglect this effect. A Bode plot of all experimental and estimated FR's and a plot of the step response for each estimated TF was not shown for the purpose of visual clarity, but can be found in Appendix F.

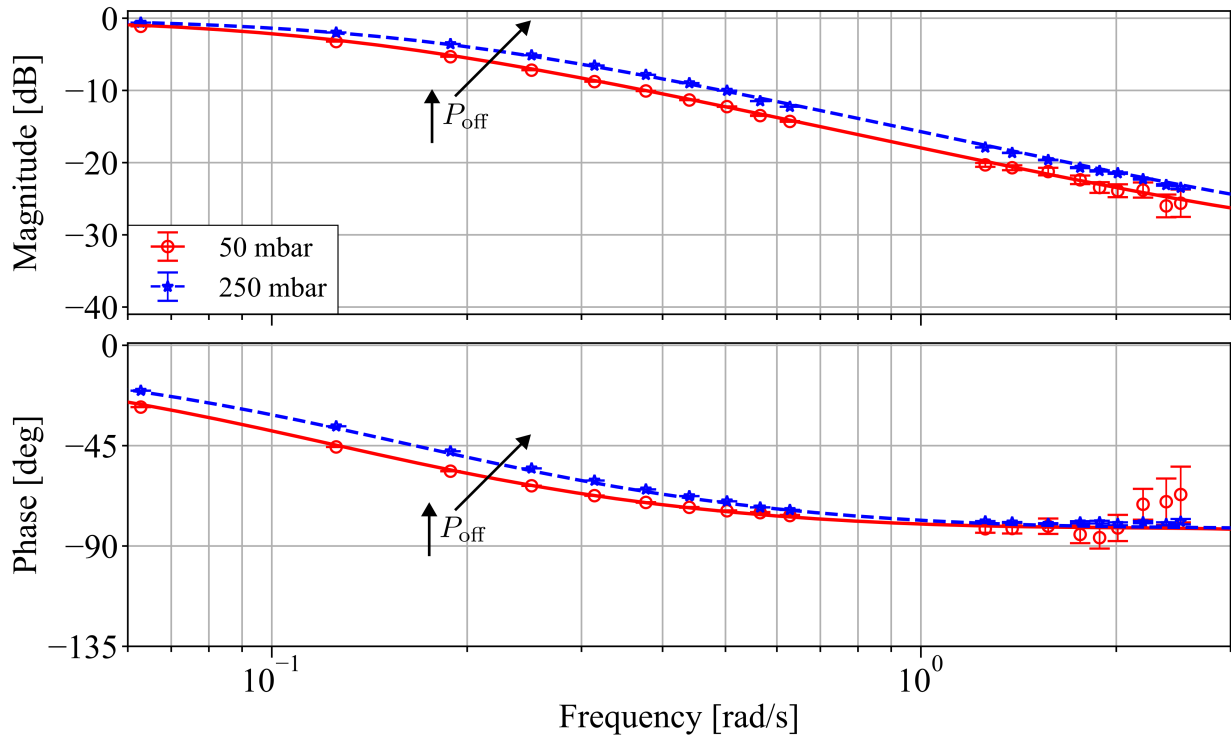


Figure 4.5: Experimental (points) and estimated (lines) FR for $P_{\text{off}} = 50$ and 250 mbar.

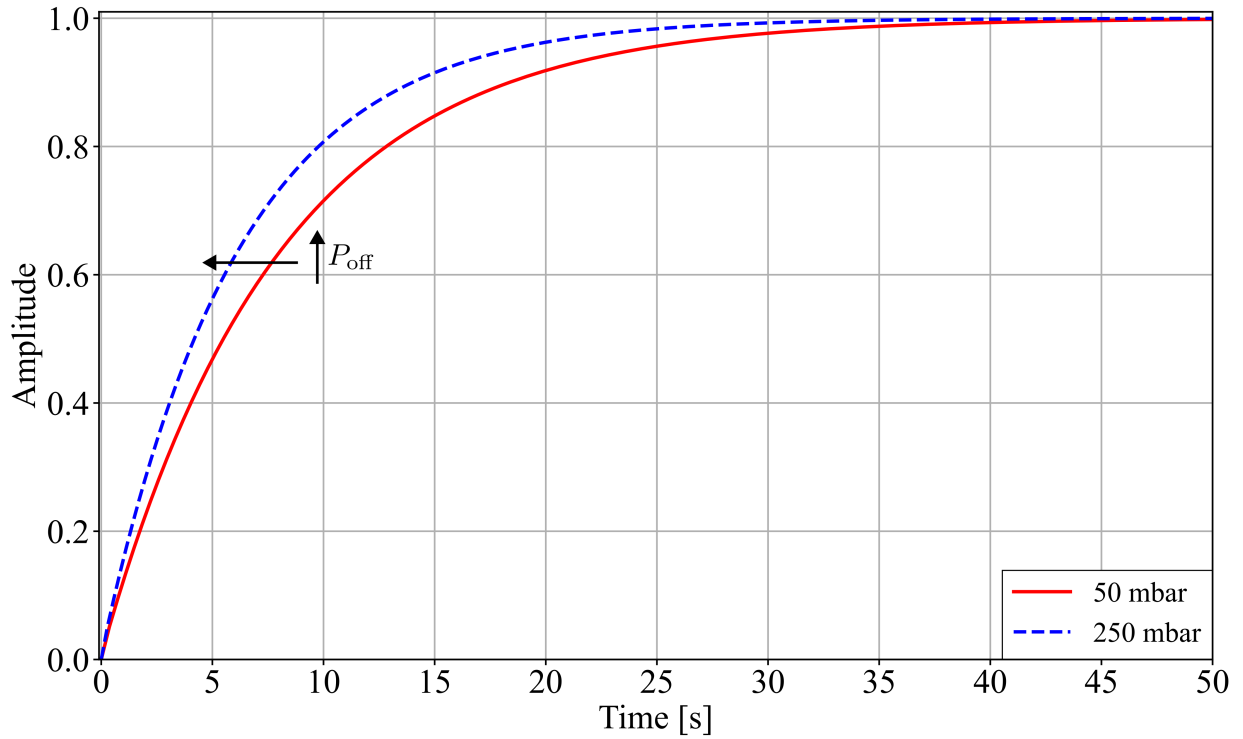


Figure 4.6: Simulated step response for estimated TF from experimental FR for $P_{\text{off}} = 50$ and 250 mbar.

Table 4.4: Parameters and associated time constants for estimated TF's from experimental FR's investigating the effect of varying P_{off} . Note that absolute uncertainties are given to show that the increase (decrease) in corner frequency (time constant) for an increase in P_{off} is statistically significant.

P_{off} [mbar]	a	b	d	τ [s]
50	0.2 ± 0.1	8.0 ± 0.1	0.15 ± 0.03	7.9 ± 0.1
100	0.2 ± 0.04	7.7 ± 0.1	0.15 ± 0.04	7.6 ± 0.1
150	0.2 ± 0.03	6.9 ± 0.1	0.15 ± 0.03	6.8 ± 0.1
200	0.2 ± 0.02	6.6 ± 0.1	0.15 ± 0.02	6.5 ± 0.1
250	0.16 ± 0.02	6.1 ± 0.1	0.12 ± 0.02	6.0 ± 0.1

4.2.4 Increasing Length-Diameter Ratio

An increase in the $\frac{L}{D_i}$ ratio, corresponding to an increase in the tubing length and/or a decrease in the tubing ID, results in a decrease of the corner frequency (Figure 4.7), an increase in b , and thus a slower step response for the system (Figure 4.8). This is physically reasonable, as an increase in the length, or a decrease in the ID, would result in an increase in the relative energy loss across the tubing, and subsequently a decrease in the velocity at which the fluid moves through the tubing with constant pressure and tubing properties (3.5). Further, due to increased attenuation of the pressure waves as $\frac{L}{D_i}$ is increased, the uncertainty in the estimated FR increases.

It is interesting to note that the magnitude of change of the corner frequency and time constant for a change in $\frac{L}{D_i}$ is significant (Table 4.5). Comparing Tables 4.4 and 4.5, the magnitude of change of the corner frequency and time constant for a change in $\frac{L}{D_i}$ is much more significant than that associated with a change of P_{off} for much smaller relative changes. This suggests that the pressure dynamics across the sample tubing have a much higher dependency on the geometric properties of the tubing as opposed to the operating pressure. Further, this indicates that the geometric properties of the tubing are important to consider if the sample tubing pressure dynamics are to be modelled for PDMFCS applications.

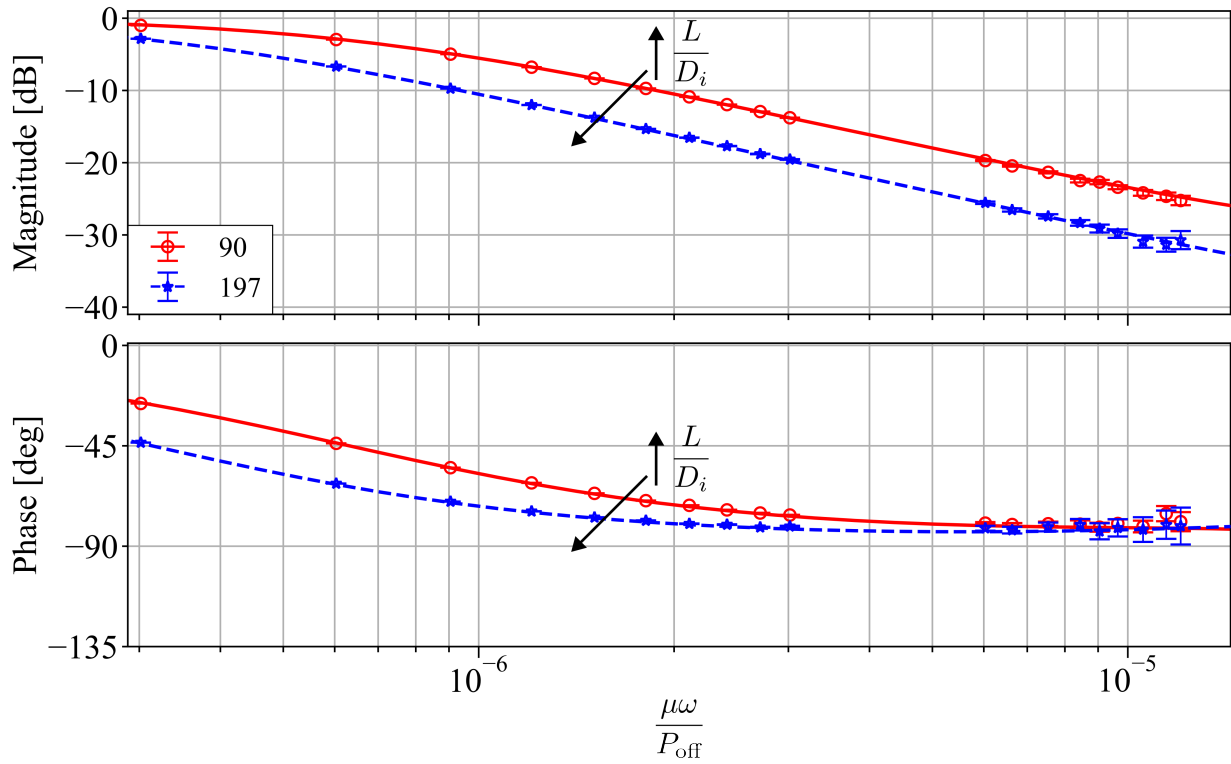


Figure 4.7: Dimensionless experimental (points) and estimated (lines) FR for $\frac{L}{D_i} = 90$ and 197.

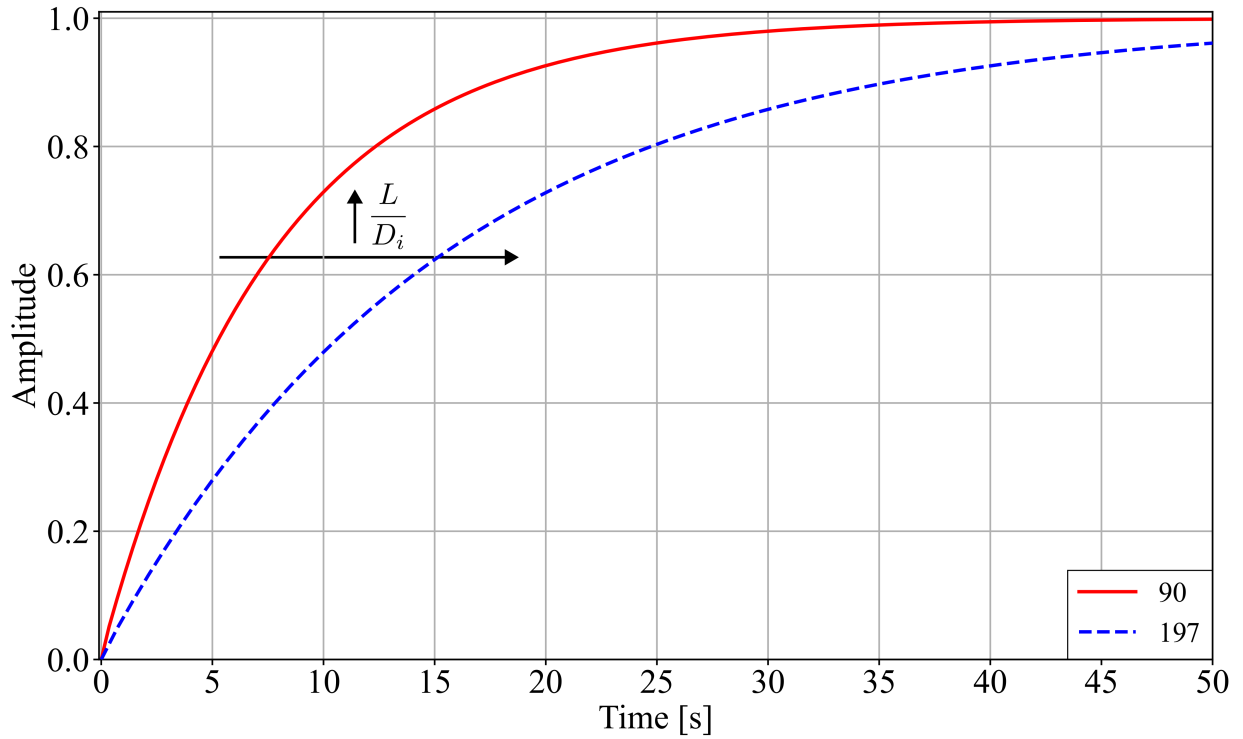


Figure 4.8: Simulated step response for estimated TF from experimental FR for $\frac{L}{D_i} = 90$ and 197. Step response was simulated from dimensional estimated TF, not the dimensionless form.

Table 4.5: Parameters and associated time constants for estimated TF's from dimensional experimental FR's investigating the effect of varying $\frac{L}{D_i}$. Note that absolute uncertainties are given to show that the decrease (increase) in corner frequency (time constant) for an increase in $\frac{L}{D_i}$ is statistically significant.

$\frac{L}{D_i}$	a	b	d	τ [s]
90	0.2 ± 0.1	7.7 ± 0.1	0.15 ± 0.04	7.6 ± 0.1
118	0.14 ± 0.03	9.7 ± 0.1	0.1 ± 0.01	9.6 ± 0.1
144	0.13 ± 0.03	11 ± 0.1	0.08 ± 0.01	10.9 ± 0.1
170	0.13 ± 0.01	13.8 ± 0.1	0.08 ± 0.01	13.7 ± 0.1
197	0.13 ± 0.03	15.4 ± 0.1	0.08 ± 0.02	15.3 ± 0.1

The table of the dimensionless estimated TF parameters, a Bode plot of all experimental

and estimated FR's, and a plot of the step response for each estimated TF were not shown for the purpose of visual clarity, but can be found in Appendix F.

4.2.5 Increasing Fluid Viscosity

Similar to an increase in $\frac{L}{D_i}$, an increase in the viscosity of the fluid results in a decrease of the corner frequency (Figure 4.9), an increase in b , and a slower step response for the system (Figure 4.10). Physically, this is rational as an increase in the viscosity would result in an increase in the relative energy loss across the tubing due to an increase in the viscous forces resisting the flow of the fluid, and subsequently a decrease in the velocity at which the fluid moves through the tubing with constant pressure and tubing properties (3.5). As in the $\frac{L}{D_i}$ case, due to increased attenuation of the pressure waves as the viscosity is increased, the uncertainty in the estimated FR increases.

Similar to the $\frac{L}{D_i}$ case, increasing the viscosity has a significant influence on the magnitude of the values of the corner frequency and time constant (Table 4.6). Where, it can be concluded that the pressure transient dynamics across the sample tubing are highly influenced by the viscosity of the working fluid. Thus, for developing a plant model including the sample tubing dynamics in a PDMFCS application, it is imperative to consider the viscosity of the working fluid, much like the tubing geometric properties.

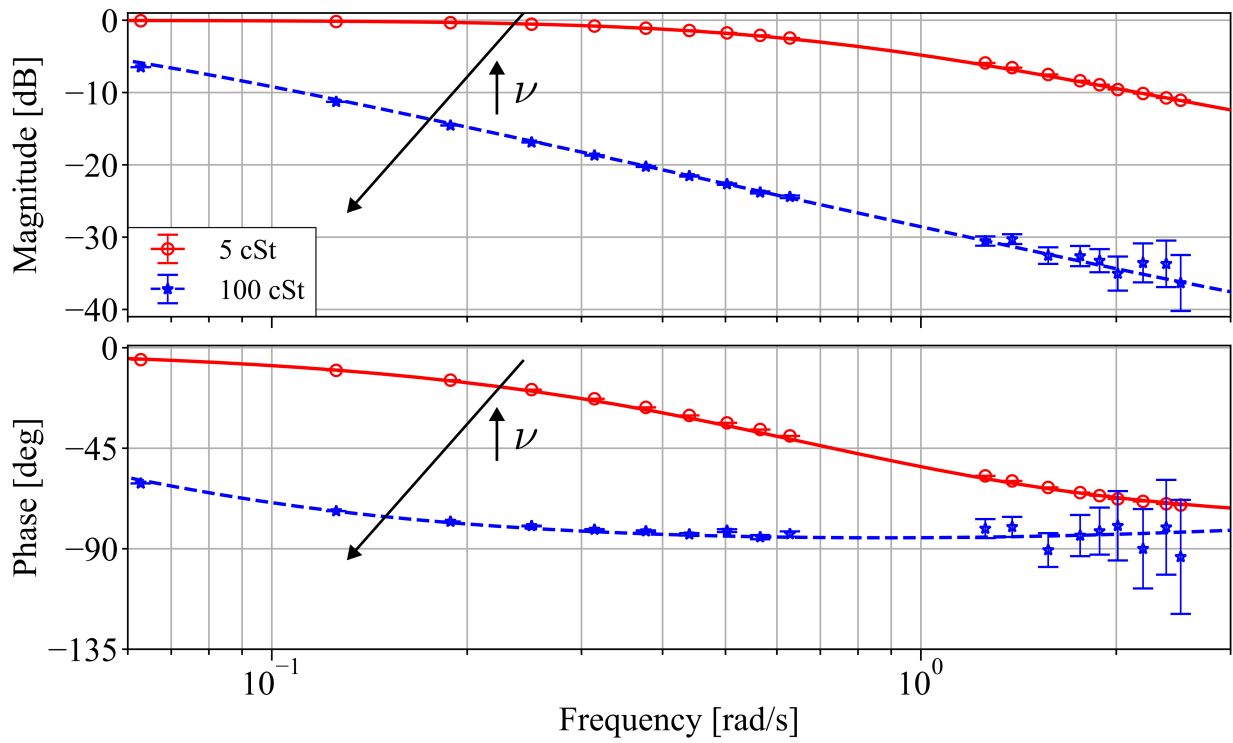


Figure 4.9: Dimensionless experimental (points) and estimated (lines) FR for $\nu = 5$ and 100 cSt.

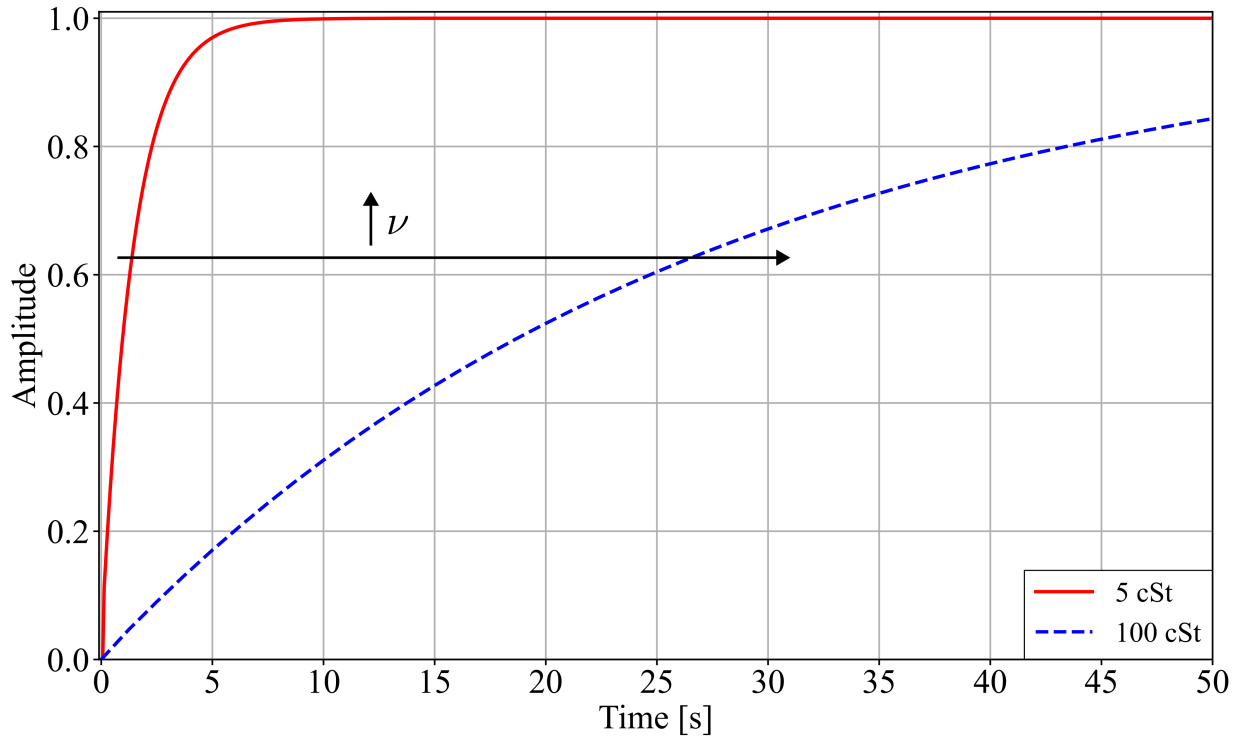


Figure 4.10: Simulated step response for estimated TF from experimental FR for $\nu = 5$ and 100 cSt.

Table 4.6: Parameters and associated time constants for estimated TF's from experimental FR's investigating the effect of varying viscosity. Note that absolute uncertainties are given to show that the decrease (increase) in corner frequency (time constant) for an increase in viscosity is statistically significant.

ν [cSt]	a	b	d	τ [s]
5	0.12 ± 0.01	1.44 ± 0.01	0.085 ± 0.005	1.33 ± 0.01
10	0.12 ± 0.003	2.20 ± 0.03	0.085 ± 0.003	2.15 ± 0.03
20	0.12 ± 0.01	4.60 ± 0.08	0.08 ± 0.003	4.53 ± 0.08
50	0.13 ± 0.03	15.4 ± 0.1	0.08 ± 0.02	15.3 ± 0.1
100	0.13 ± 0.03	27.0 ± 0.5	0.08 ± 0.01	26.8 ± 0.5

A Bode plot of all experimental and estimated FR's and a plot of the step response for each estimated TF was not shown for the purpose of visual clarity, but can be found in

4.2.6 Increasing Tubing Material Stiffness

These tests pushed the current experimental setup to its limits, due to the small ratio of tubing ID to junction diameter (0.25). The small ratio caused extensive expansion/contraction losses through the pressure sensor junctions [73, 96] resulting in measured pressure transients that are much slower than what would actually be present in the sample tubing during normal PDMFCS operation with similar tubing/fluid properties, as discussed in Section 3.2.3. From the measurement perspective, very high attenuation of the input and output waves was observed. This attenuation resulted in magnitude FR attenuation across all frequency bands, and large signal-to-noise ratios that contributed significantly to the magnitude of the uncertainty in the experimental FR (Figure 4.11). No clear relationship between the corner frequency and τ with material stiffness was noted, and there was overlap for the uncertainty bounds of b and τ of the estimated TF's (Table 4.7).

Although the lack of relationship between the parameter values and material stiffness, as well as the overlap of the b and τ uncertainty bounds, may indicate that the pressure transient dynamics across the sample tubing are independent of the tubing material stiffness; there is hesitance to make such a definitive conclusion due to the limitations of the experimental setup used to test this dependency which resulted in significant expansion/contraction losses and large uncertainties in the estimated TF parameters. As previously discussed in Section 3.2.3, the low diameter ratio (0.25) between the sample tubing and the junctions, coupled with the fact that microfluidic flow is laminar, resulted in large expansion and contraction losses [73, 96]. These losses created unrealistic and highly attenuated flow conditions, which resulted in large uncertainties in pressure wave measurements that propagated through to the subsequent experimental FR and TF estimation. As previously stated, see Section 3.2.3, the diameter ratio for all other parameter tests was 0.75, which results in only minor expansion/contraction loss [73, 96] that did not greatly affect the physical realism of the flow. Thus, to confidently conclude sample tubing pressure dynamics dependency on tubing material stiffness, an improvement of the experimental setup/procedure is necessary.

To improve the experimental setup, it is advisable to develop an apparatus and/or purchase sample tubing, such that the ratio of the sample tubing ID and the junction diameter is close to one. Where, a diameter ratio approximately equal to one would result in the most realistic flow conditions and minimize the expansion and contraction losses in the flow [73], decreasing the uncertainty in the experimental measurements associated

with the setup. These tests would be best suited for further study, possibly in conjunction with exploration of how the microfluidic chip and tubing wall thickness affect the pressure transient dynamics across the sample tubing. It should also be noted that improving the setup to minimize expansion/contraction losses would also increase the accuracy of the experimental FR and estimated TF for the tubing setups used to explore the other experimental parameters in this study.

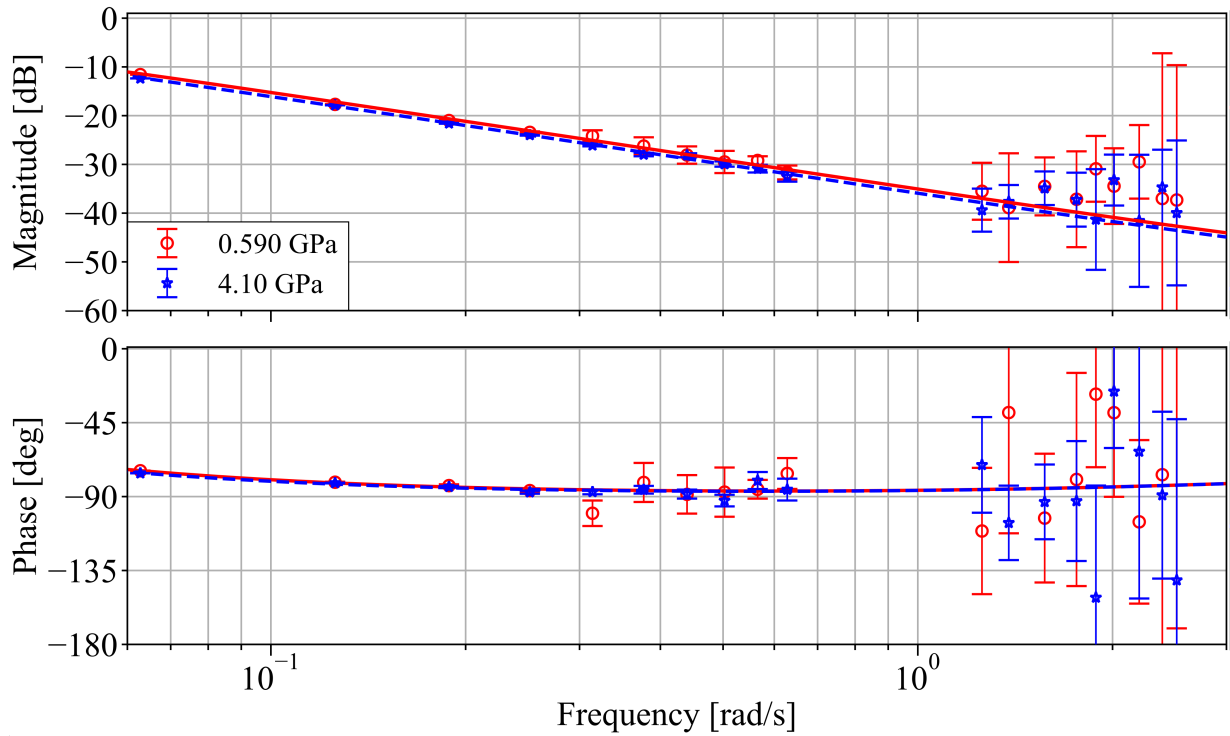


Figure 4.11: Dimensionless experimental (points) and estimated (lines) FR for $E_{\text{flex}} = 0.590$ (HPPFA) and 4.10 GPa (PEEK).

Table 4.7: Parameters and associated time constants for estimated TF's from experimental FR's investigating the effect of varying tubing material stiffness. Note that absolute uncertainties are given to show that the effect of varying material stiffness on the corner frequency and time constant cannot be verified statistically due to the overlapping uncertainty bounds.

Material	E_{flex} [GPa]	a	b	d	τ [s]
FEP	0.586	0.13 ± 0.06	51 ± 2	0.08 ± 0.01	51 ± 2
HPPFA	0.590	0.13 ± 0.03	57 ± 3	0.08 ± 0.02	57 ± 3
Tefzel ETFE	1.00	0.13 ± 0.07	55 ± 3	0.08 ± 0.01	55 ± 3
PEEK	4.10	0.13 ± 0.04	63 ± 4	0.08 ± 0.03	63 ± 4

A Bode plot of all experimental and estimated FR's and a plot of the step response for each estimated TF was not shown for the purpose of visual clarity, but can be found in Appendix F.

4.2.7 Summary

Effectiveness of Methodology

The experimental setup and methodology described in Chapter 3, proved to be effective at experimentally characterizing the pressure transient dynamics across the sample tubing using FR techniques, for tubing setups that minimize expansion and contraction losses across the sample tubing/pressure sensor junctions. Pressure transient dynamics across the sample tubing were shown to be characterized as a first-order TF with a transport lag component. This experimental methodology allows an experimentally estimated TF of the pressure transient dynamics across the sample tubing to be incorporated into the PDMFCS plant model to improve its accuracy. With, an improvement in the PDMFCS plant model accuracy, more accurate stability and dynamic response analyses of the system can be performed. Where, increased accuracy in the stability and dynamic response analyses will allow for the development of an informed and robust design methodology for the PDMFCS, which will advance the PDMFCS towards modularity.

Effect of Parameter Variation

Pressure transient dynamics were shown to have no amplitude dependence and a slight dependency on the mean input pressure, but were most significantly affected by tubing

geometric properties and fluid viscosity. Decreasing the offset pressure, increasing the tubing’s length to diameter ratio, or increasing the fluid’s viscosity resulted in an increase in the relative energy loss across the tubing, which decreased the corner frequency and increased the step response time constant. Understanding the effect of this parameter variation is useful from a PDMFCS design standpoint, as future designers can now infer how to physically vary dynamic response characteristics of the system to reach desired stability and response objectives. Further, the lack of amplitude dependency indicates that the system can be approximated as linear for control system design and analysis. No effect of material stiffness was observed, but a definitive conclusion was not made on this dependency due to limitations of the experimental setup resulting in significant expansion/contraction losses which created physically unrealistic flow conditions and large uncertainties in the measurements obtained during the material stiffness tests. As such, an improvement to the experimental setup to minimize expansion/contraction losses is necessary so that the true effect of material stiffness can be quantified.

4.3 Hydrodynamic Equivalent Circuit Model

4.3.1 Comparison to Experimentally Estimated TF

For the following discussion, the calculation of the hydrodynamic resistance (2.1), inertial (2.2), and compliance (2.3, 2.4, 2.5) effects considered the experimental case where $P_{\text{off}} = 100$ mbar, $P_A = 0.25P_{\text{off}}$, $L = 69$ mm, $D_i = 0.763$ mm, silicone oil is the working fluid with $\nu = 50$ cSt, and the tubing material is FEP. The choice of the experimental case used for the HECM comparison and calculated parameter values was arbitrary. Due to the lack of manufacturer/supplier information for the values of E_{tens} and ν_w of the sample tubing, these values were assumed to be 0.346 GPa [107, 108] and 0.48 [112], which are the values provided by other manufacturers for FEP tubing. Similarly, β_a for the purchased silicone oil was not known by the manufacturer, so its value was assumed to be 1.7237 GPa, which is a typical value of adiabatic bulk modulus for hydraulic oils [106].

Model Form

Compared to the non-minimum phase first-order model estimated from the experimental FR, the symmetric HECM results in third (3.25, 3.26, 3.27, 3.28), and second order TF’s (3.29). Meanwhile the simplified HECM’s produce second (3.30, 3.31), and first-order (3.32, 3.33, 3.34,3.35) TF’s. Notably, $G_C(s)$ of the RC HECM (3.33), and $G_R(s)$ of the RL

HECM (3.34) present the same qualitative first-order characteristics as the experimentally estimated TF, albeit without the zero and transport lag component. In fact, no HECM form captures the transport lag component present in the experimentally estimated TF, which makes sense as the HECM is derived from the assumption of hydrodynamic steady-state flow. Although it should be noted that the transport lag observed from experiments was rather small and it may be reasonable for an analytical model to neglect this. Clearly, the higher-order TF's will have differing forms of step and frequency response than that of the experimentally estimated TF, but this is reasonable given that the input-output signals differ between the model and experiment, and the HECM component dynamics relate to start-up time due to individual fluidic losses as opposed to the raw pressure transient across the tubing, as discussed in Section 3.4.3. Thus, for the higher-order models it is sufficient to determine their effectiveness at modelling the sample tubing dynamics by assessing if the order of magnitude of the step response characteristics and the locations of the corner frequencies are approximately equivalent to those found from the experimental characterization of pressure transient dynamics across the sample tubing.

Transient and Frequency Response Characteristics

When compared to the simulated step response characteristic from the experimentally estimated TF, it is seen that the governing HECM components for a given model form predict transient characteristics that are orders of magnitude faster than those experimentally characterised (Table 4.8). Further, the FR of the governing HECM components for a given model form present corner frequencies much greater than those found in the experimental FR (Figures 4.12, 4.13, 4.14, 4.15, and 4.16). Varying the tubing capacitance, or neglecting either the inertial or compliance effects for the first-order models, showed slight differences in transient times and corner frequencies, but any improvements to the model were marginal. Therefore, the HECM, regardless of model form, predicts a significantly faster time for the flow through the sample tubing to reach hydrodynamic steady-state, than what was experimentally discovered. Hence, the HECM inadequately approximates dynamics across the sample tubing, and therefore should not be used to quantitatively model the sample tubing in the PDMFCS.

Table 4.8: Comparison of governing simulated step response characteristic for HECM forms and experimentally estimated TF.

Tubing Capacitance	Model	Governing TF	$T_s \cdot 10^3$ [s]	τ [s]
Wong et al.(2.3)	Symmetric	$G_C(s)$	2.82	N/A
	Second Order	$G_L(s)$	2.84	N/A
	First Order (RC)	$G_C(s)$	N/A	$0.0181 \cdot 10^{-3}$
	First Order (RL)	$G_R(s)$	N/A	$0.362 \cdot 10^{-3}$
	Experimental	$G_p(s)$	N/A	7.9 ± 0.1
Thin Wall (2.4)	Symmetric	$G_C(s)$	2.67	N/A
	Second Order	$G_C(s)$	2.92	N/A
	First Order (RC)	$G_C(s)$	N/A	$0.0741 \cdot 10^{-3}$
	First Order (RL)	$G_R(s)$	N/A	$0.362 \cdot 10^{-3}$
	Experimental	$G_p(s)$	N/A	7.9 ± 0.1
Thick Wall (2.5)	Symmetric	$G_C(s)$	2.68	N/A
	Second Order	$G_L(s)$	2.74	N/A
	First Order (RC)	$G_C(s)$	N/A	$0.114 \cdot 10^{-3}$
	First Order (RL)	$G_R(s)$	N/A	$0.362 \cdot 10^{-3}$
	Experimental	$G_p(s)$	N/A	7.9 ± 0.1

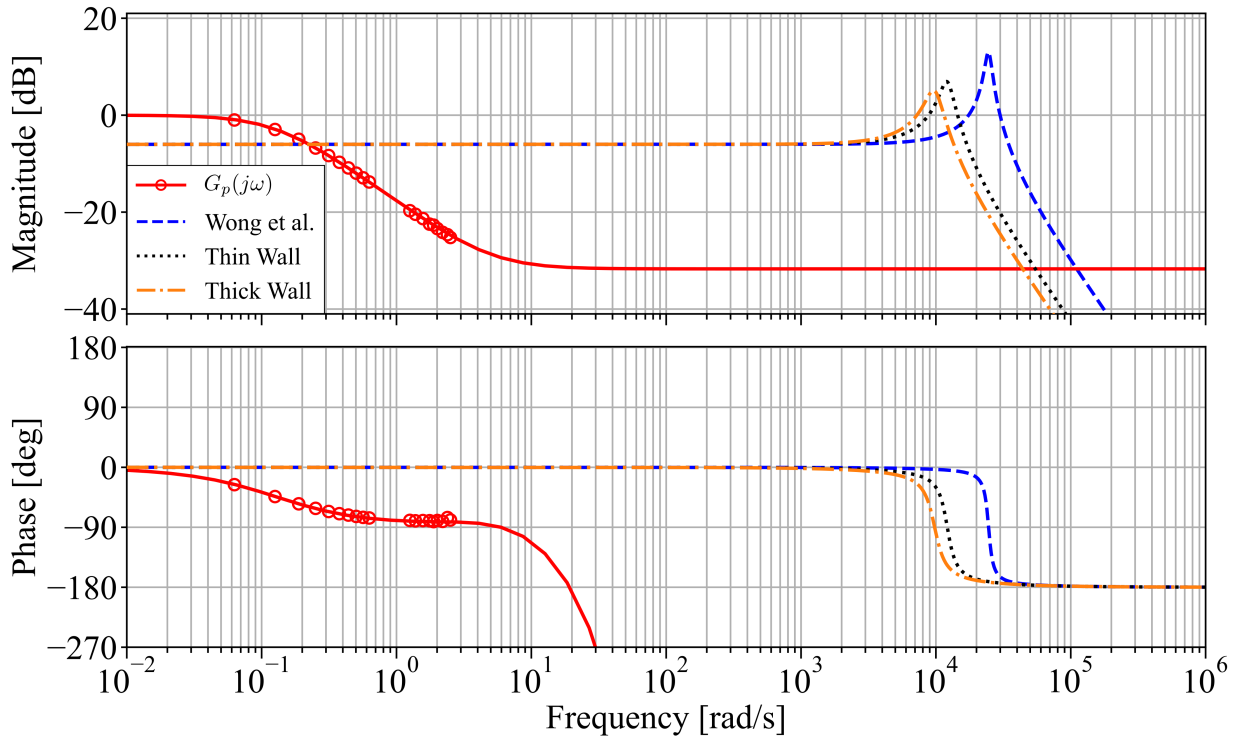


Figure 4.12: Comparison of FR of governing TF for symmetric HECM, $G_C(s)$, and experimentally estimated TF, $G_p(s)$, for pressure transient dynamics across sample tubing. For FR of $G_C(s)$, Wong et al.'s (2.3), thin wall (2.4), and thick wall (2.5) compliance models were considered. Uncertainties in experimental FR points are not shown for the purpose of visual clarity.

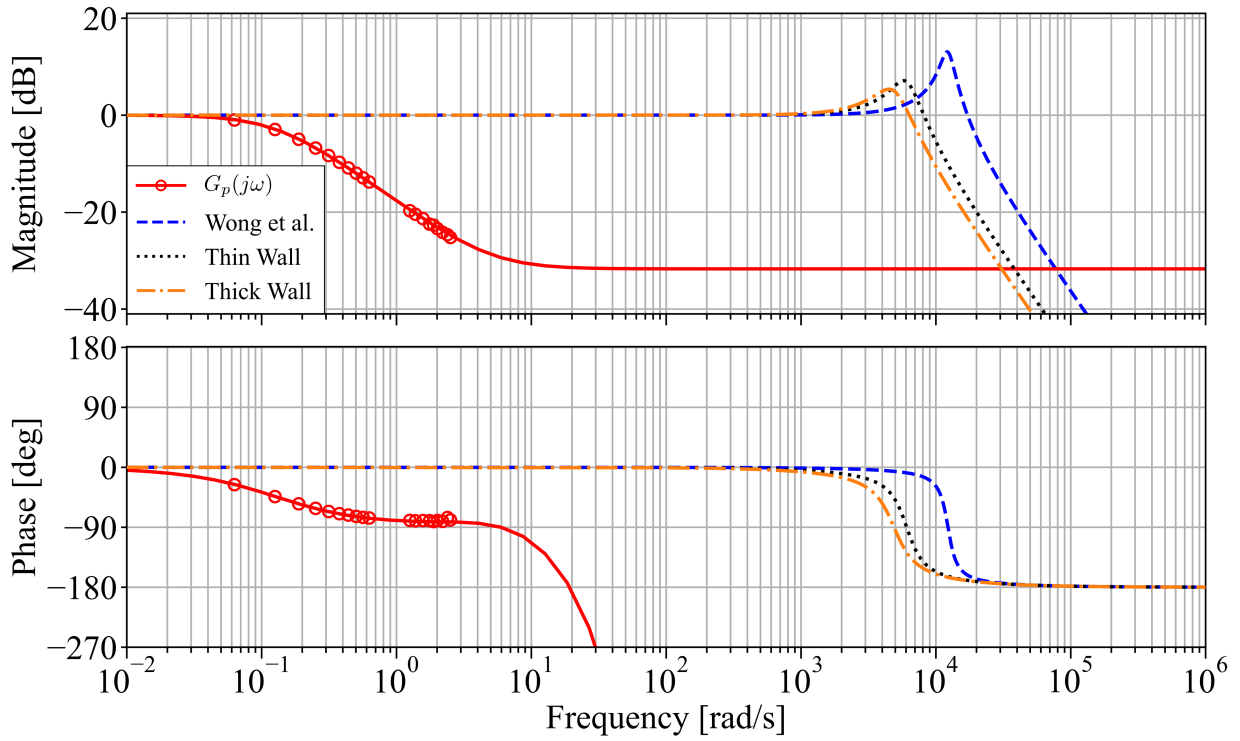


Figure 4.13: Comparison of FR of governing TF for second-order HECM, $G_C(s)$, and experimentally estimated TF, $G_p(s)$, for pressure transient dynamics across sample tubing. For FR of $G_C(s)$, Wong et al.'s (2.3), thin wall (2.4), and thick wall (2.5) compliance models were considered. Uncertainties in experimental FR points are not shown for the purpose of visual clarity.

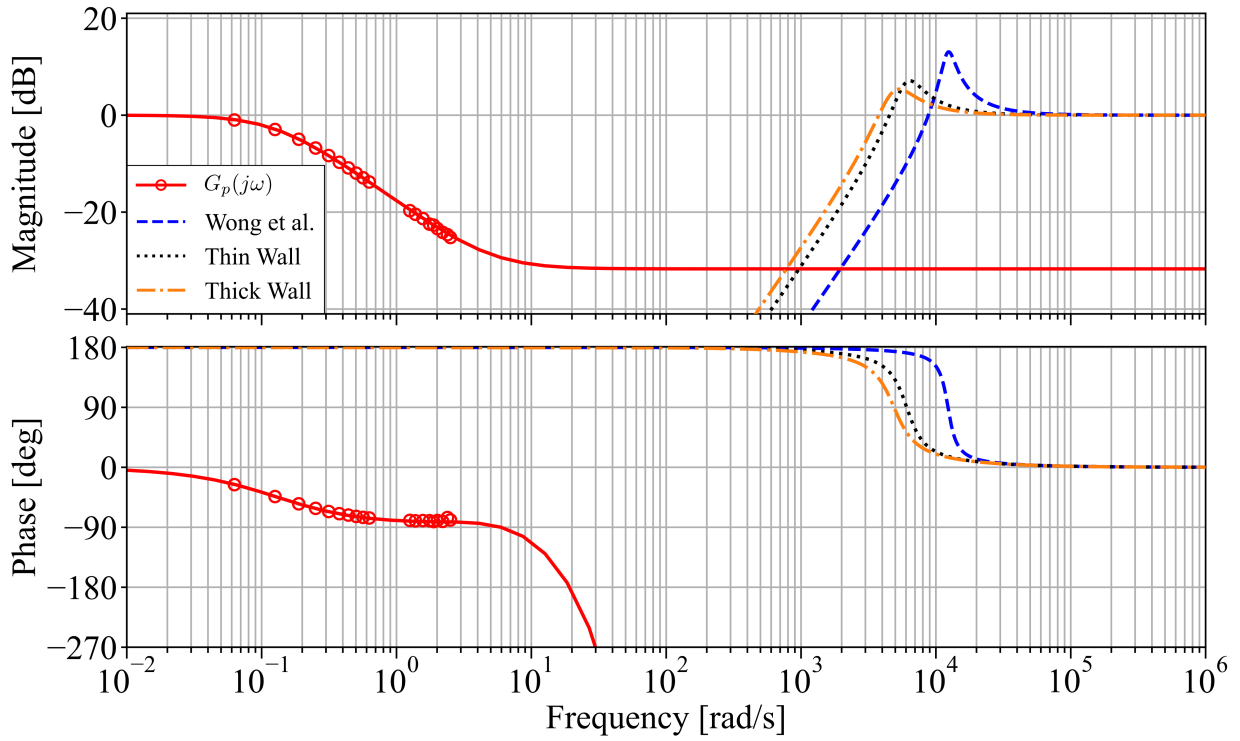


Figure 4.14: Comparison of FR of governing TF for second-order HECM, $G_L(s)$, and experimentally estimated TF, $G_p(s)$, for pressure transient dynamics across sample tubing. For FR of $G_L(s)$, Wong et al.'s (2.3), thin wall (2.4), and thick wall (2.5) compliance models were considered. Uncertainties in experimental FR points are not shown for the purpose of visual clarity.

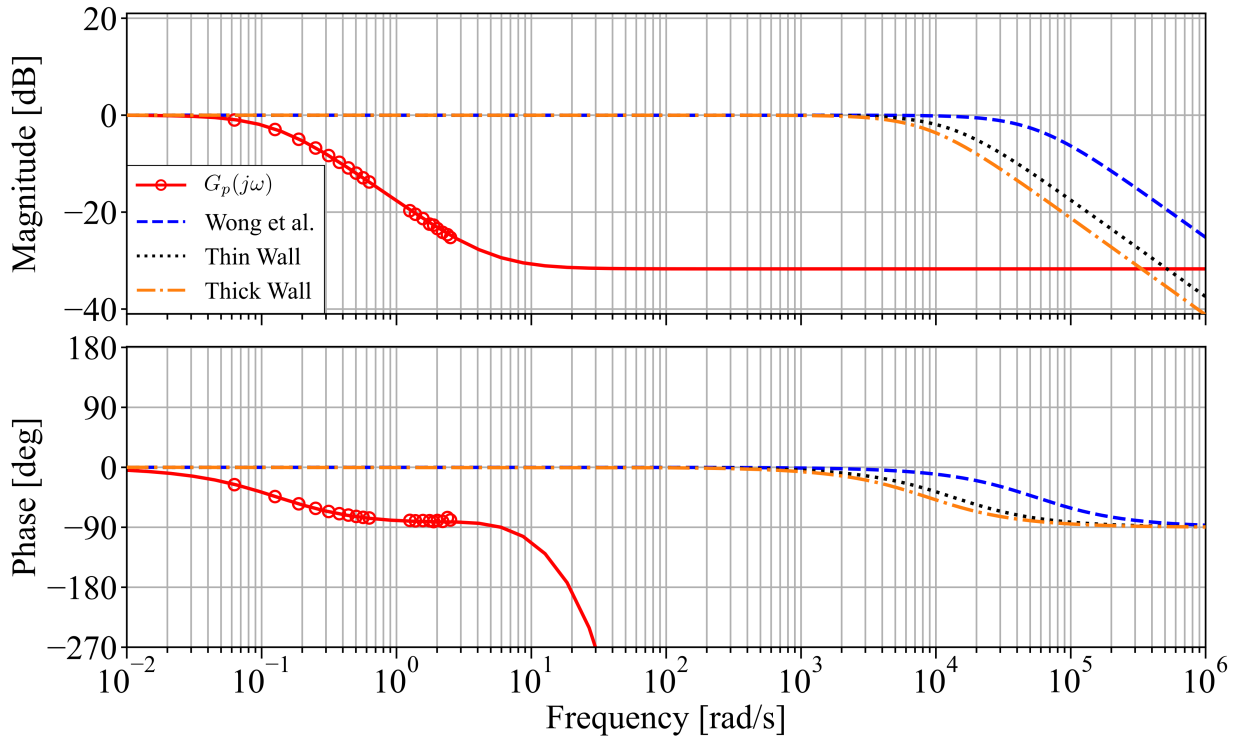


Figure 4.15: Comparison of FR of governing TF for first-order RC HECM, $G_C(s)$, and experimentally estimated TF, $G_p(s)$, for pressure transient dynamics across sample tubing. For FR of $G_C(s)$, Wong et al.'s (2.3), thin wall (2.4), and thick wall (2.5) compliance models were considered. Uncertainties in experimental FR points are not shown for the purpose of visual clarity.

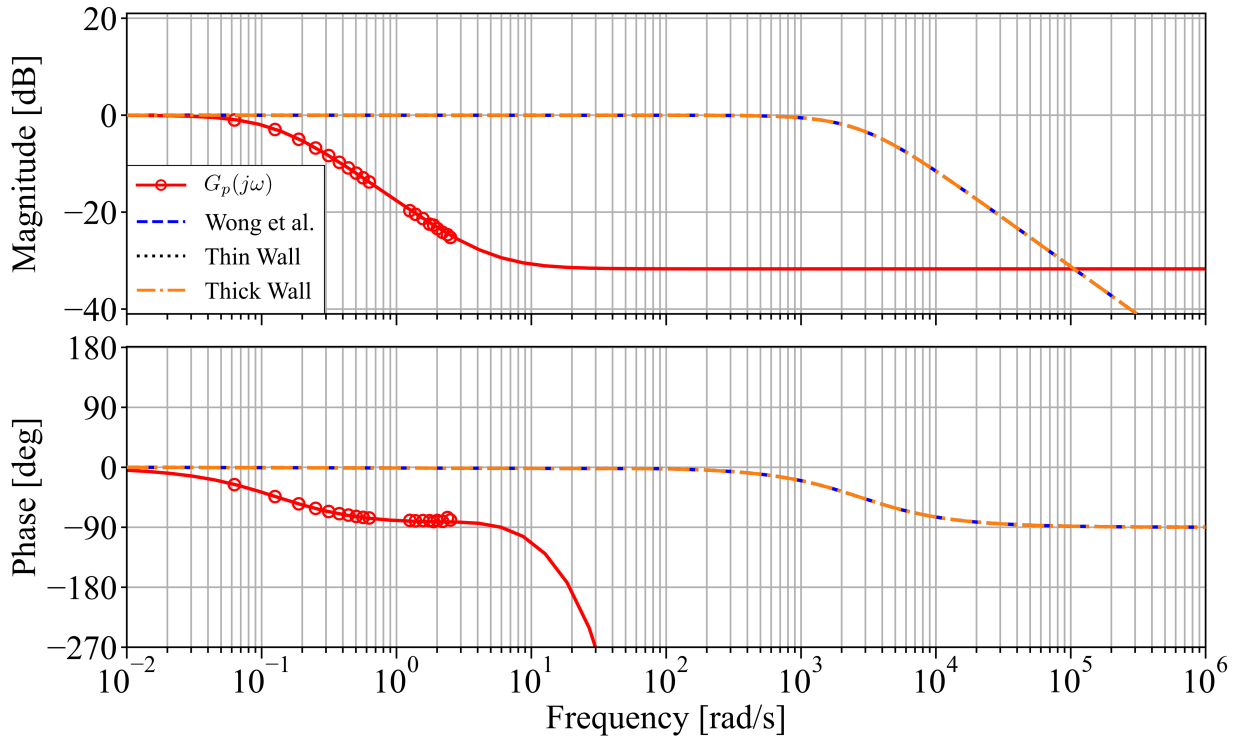


Figure 4.16: Comparison of FR of governing TF for first-order RL HECM, $G_R(s)$, and experimentally estimated TF, $G_p(s)$, for pressure transient dynamics across sample tubing. For FR of $G_R(s)$, Wong et al.'s (2.3), thin wall (2.4), and thick wall (2.5) compliance models were considered, but have no effect in this case. Uncertainties in experimental FR points are not shown for the purpose of visual clarity.

Limitations of the HECM

The assumption of steady-state flow inherent to the HECM derivation is hypothesised to be the primary reason for the HECM's unsatisfactory approximation of hydrodynamic transient dynamics in the sample tubing. Where, the control volume derivation is reliant on the assumption that a near constant pressure drop is present across the fluid element. In the case of control system operation, this assumption implies that a change in pressure across the tubing occurs nearly instantaneously, that is the pressure/velocity field of the fluid across the sample tubing almost instantaneously reaches steady-state [73]. However, it was observed experimentally that there is a significant transient time for the outlet sample tubing pressure to change with respect to a change of the inlet sample tubing pressure,

after which the fluid would reach a hydrodynamic steady-state. Thus, the assumption of steady-state flow used to derive the HECM, results in its inadequate modelling of the sample tubing dynamics by severely underestimating the time for the fluid within the sample tubing to reach a hydrodynamic steady-state.

4.3.2 Effect of Varying Tubing/Fluid Parameters

Although the HECM is unsuccessful at quantitatively approximating corner frequencies and transients in the sample tubing, it is still useful to determine if the HECM qualitatively presents the same change in corner frequencies/transients with variation of tubing/fluid parameters as was found experimentally. For if the HECM proves to be successful at modelling the qualitative effect of variation of parameters, then an empirical correction factor for the HECM could be developed, similar to what has been done for TFs modelling other physical processes [115, 116]. To explore these effects, $G_C(s)$, from the first-order RC HECM was used (3.33). The reasons for using (3.33) are that firstly, this form has the same governing first-order characteristics as the experimentally estimated TF's. This makes it easy to see if there is the same qualitative effect on the corner frequency and time constant with variation of parameters, where the effects of changing parameters on higher-order systems can be more nuanced. Secondly, to develop an empirical correction factor for the corner frequencies and time constants predicted by the HECM, it is pertinent that the analytical model has the same general form as the experimental model to ensure dynamic similarity is maintained. One should note that (3.34) could also be used for this discussion, but (3.33) was used instead to simulate the effect of the variation of E_{tens} .

Pressure Variation

Due to the assumption of steady-state flow prevalent in the derivation of the HECM, (3.33) has no dependency on input pressure, so this effect could not be studied in the model. However, as was discussed in Sections 4.2.2 and 4.2.3, the effect of the input (offset) pressure is not significant except for large changes in pressure, so it is reasonable for a model to neglect this. Similar arguments are made for pressure measurement line transient models [68].

Increasing Tubing Length

Increasing tubing length resulted in a decrease in the corner frequency (Figure 4.17) and an increase in the time constant (Figure 4.18). The same effect was found experimentally

(Section 4.2.4). Thus, (3.33) succeeds at qualitatively modelling the effect of changing the tubing length.

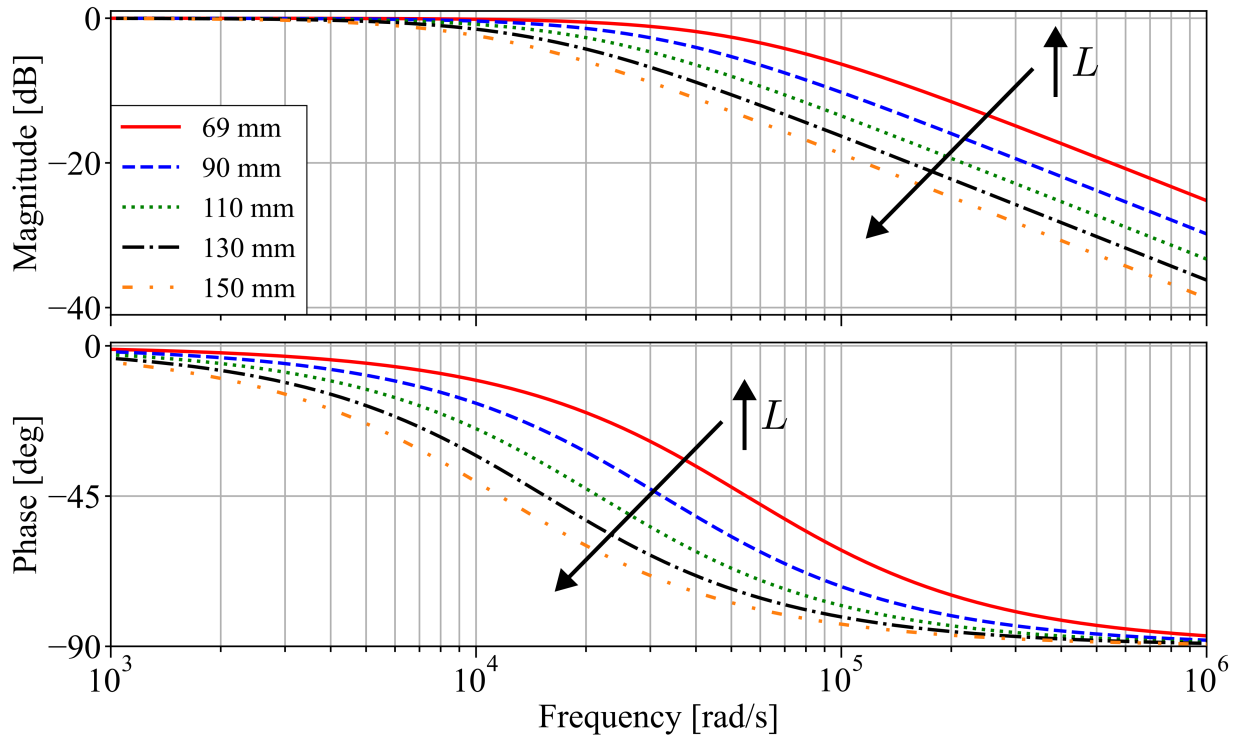


Figure 4.17: FR's of governing TF for first-order RC HECM, $G_C(s)$, for increasing tubing L . Wong et al.'s (2.3) compliance model considered.

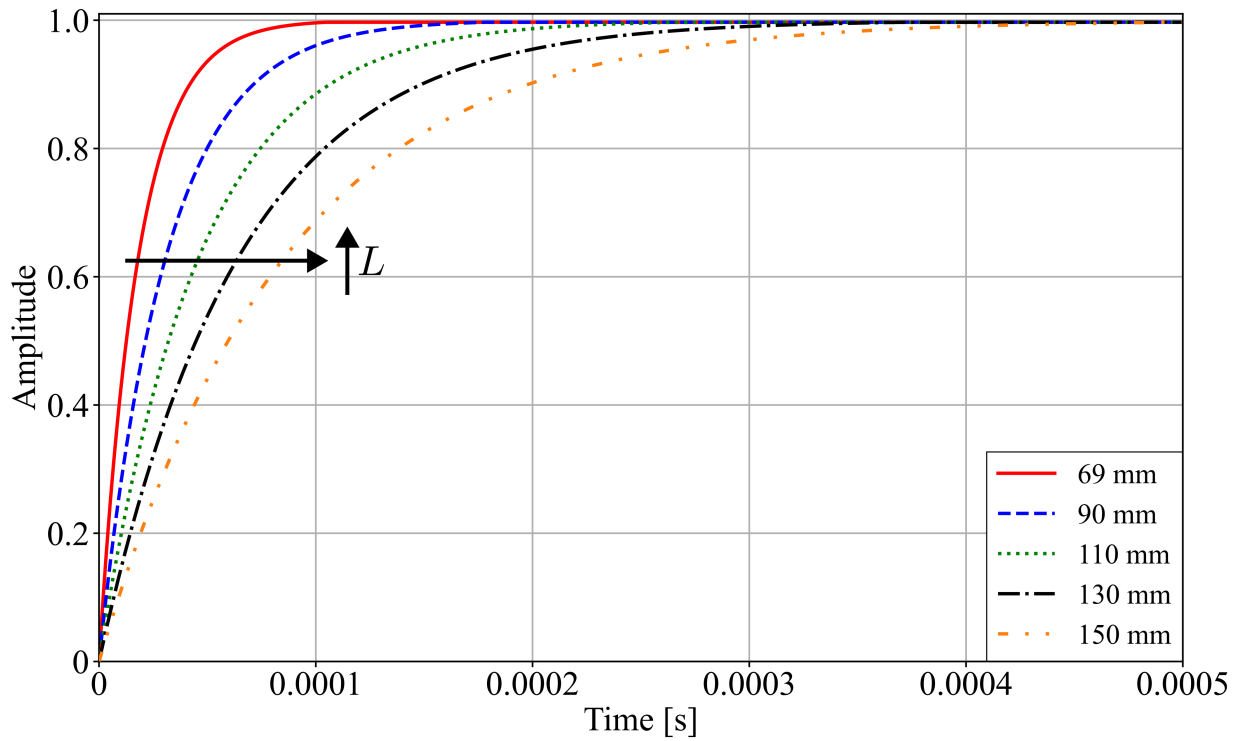


Figure 4.18: Simulated step responses for governing TF for first-order RC HECM, $G_C(s)$, for increasing tubing L . Wong et al.'s (2.3) compliance model considered.

Increasing Tubing Inner Diameter

Increasing D_i of the tubing resulted in an increase in the corner frequency (Figure 4.19) and a decrease in the time constant (Figure 4.20). The same effect was found experimentally (Section 4.2.4). Thus, (3.33) succeeds at qualitatively modelling the effect of changing D_i of the tubing.

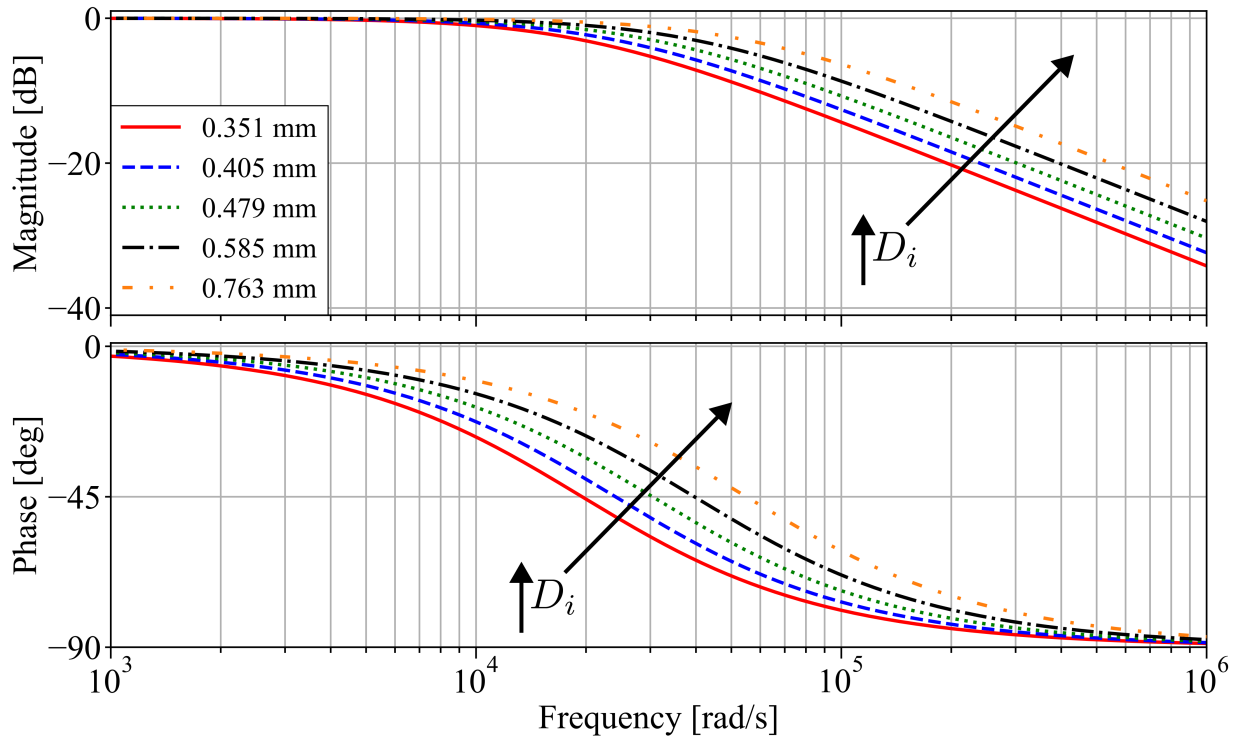


Figure 4.19: FR's of governing TF for first-order RC HECM, $G_C(s)$, for increasing tubing D_i . Wong et al.'s (2.3) compliance model considered.

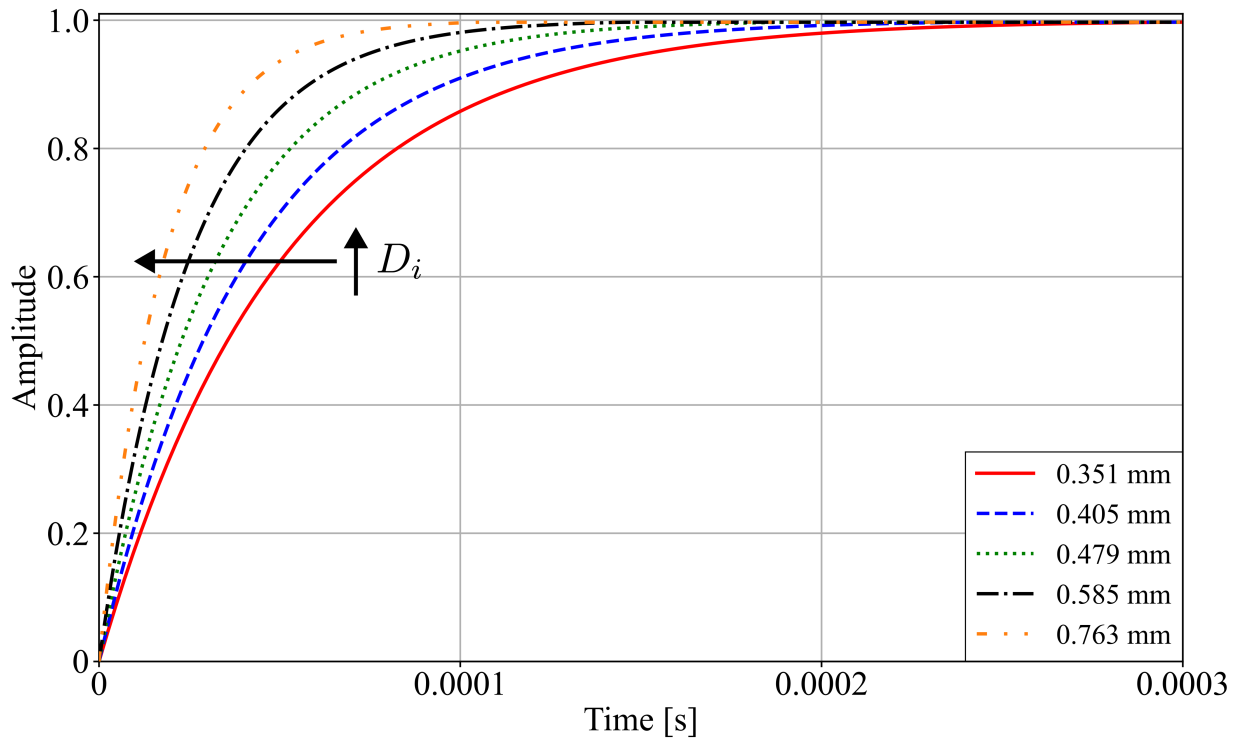


Figure 4.20: Simulated step responses for governing TF for first-order RC HECM, $G_C(s)$, for increasing tubing D_i . Wong et al.'s (2.3) compliance model considered.

Increasing Fluid Viscosity

Increasing fluid viscosity resulted in a decrease in the corner frequency (Figure 4.21) and an increase in the time constant (Figure 4.22). The same effect was found experimentally (Section 4.2.5). Thus, (3.33) succeeds at qualitatively modelling the effect of changing the fluid viscosity.

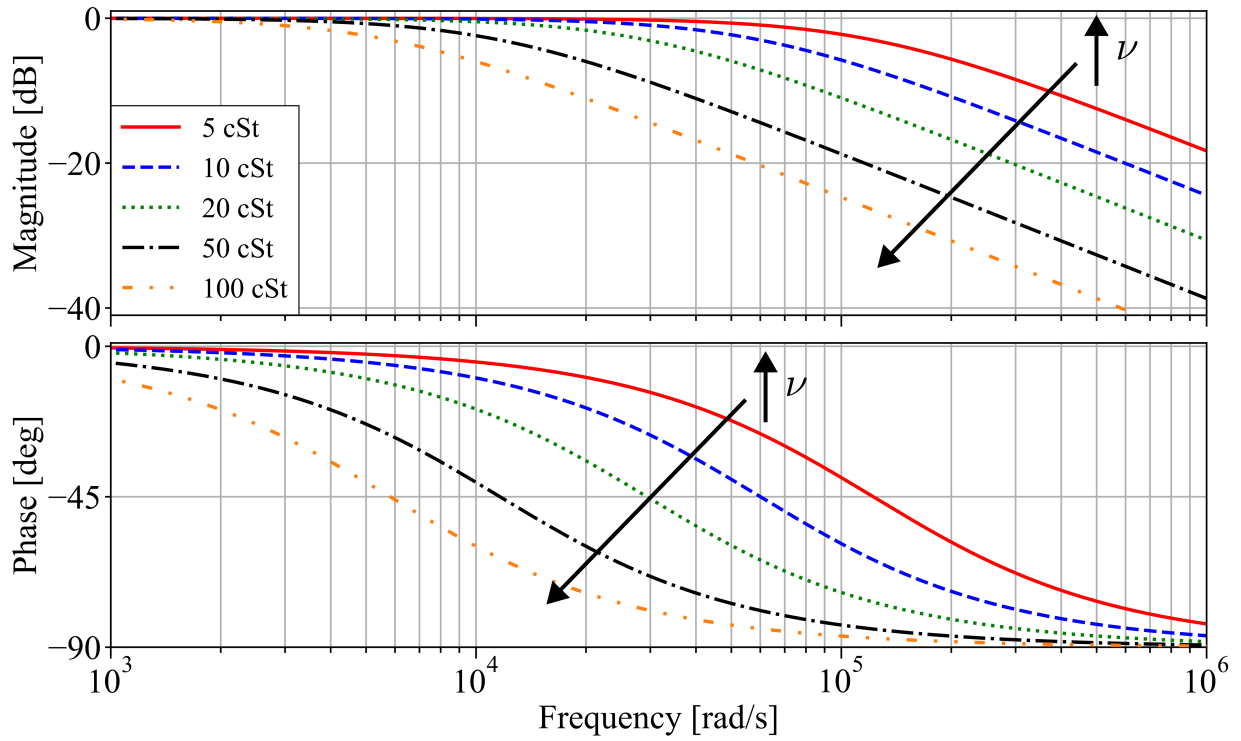


Figure 4.21: FR's of governing TF for first-order RC HECM, $G_C(s)$, for increasing fluid ν . Wong et al.'s (2.3) compliance model considered.

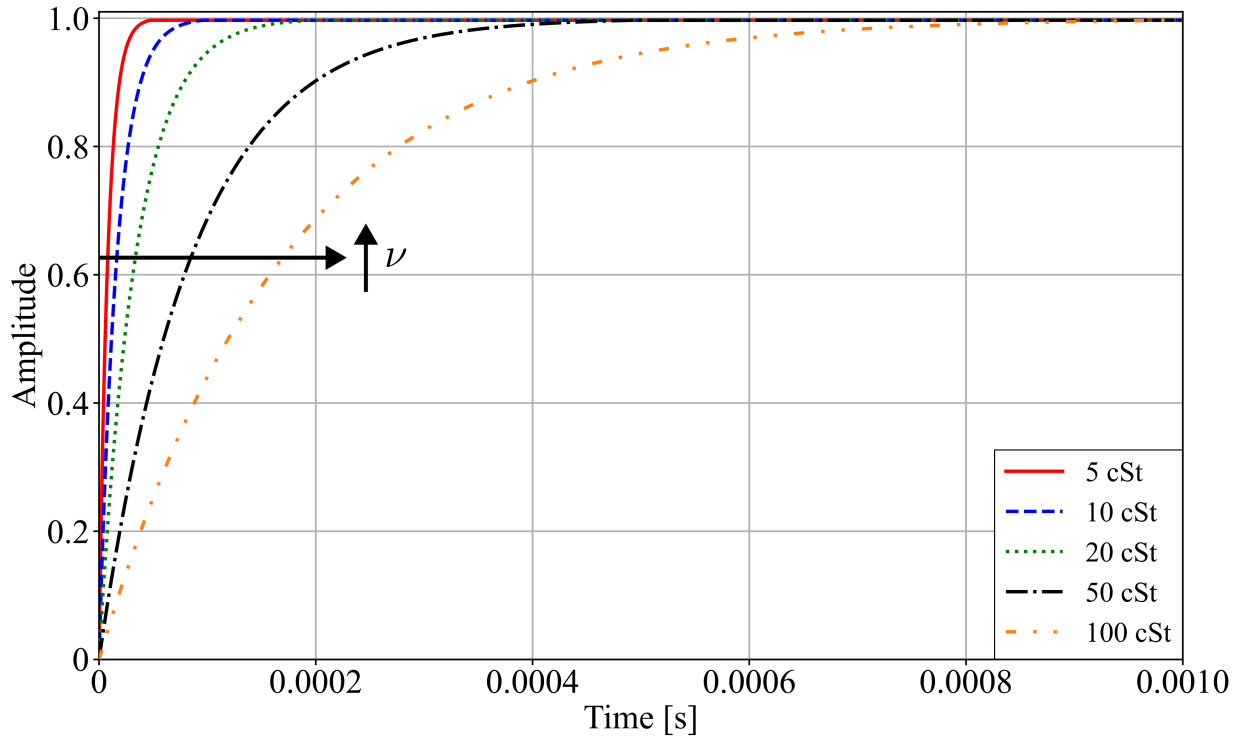


Figure 4.22: Simulated step responses for governing TF for first-order RC HECM, $G_C(s)$, for increasing tubing ν . Wong et al.'s (2.3) compliance model considered.

Increasing Tubing Material Stiffness

Increasing tubing stiffness resulted in a slight increase in the corner frequency (Figure 4.23) and a slight decrease in the time constant (Figure 4.24), but the effect is almost negligible. From the experiments, no clear effect of varying tubing stiffness was observed, but a definitive conclusion was not made due to limitations of the experimental setup creating significant expansion/contraction losses resulting in large uncertainties in the results, see Section 4.2.6. As such, the effectiveness of (3.33) at qualitatively modelling the effect of increasing tubing stiffness cannot be assessed until an improvement to the experimental setup is made, such that the effect of tubing material stiffness can be definitively quantified.

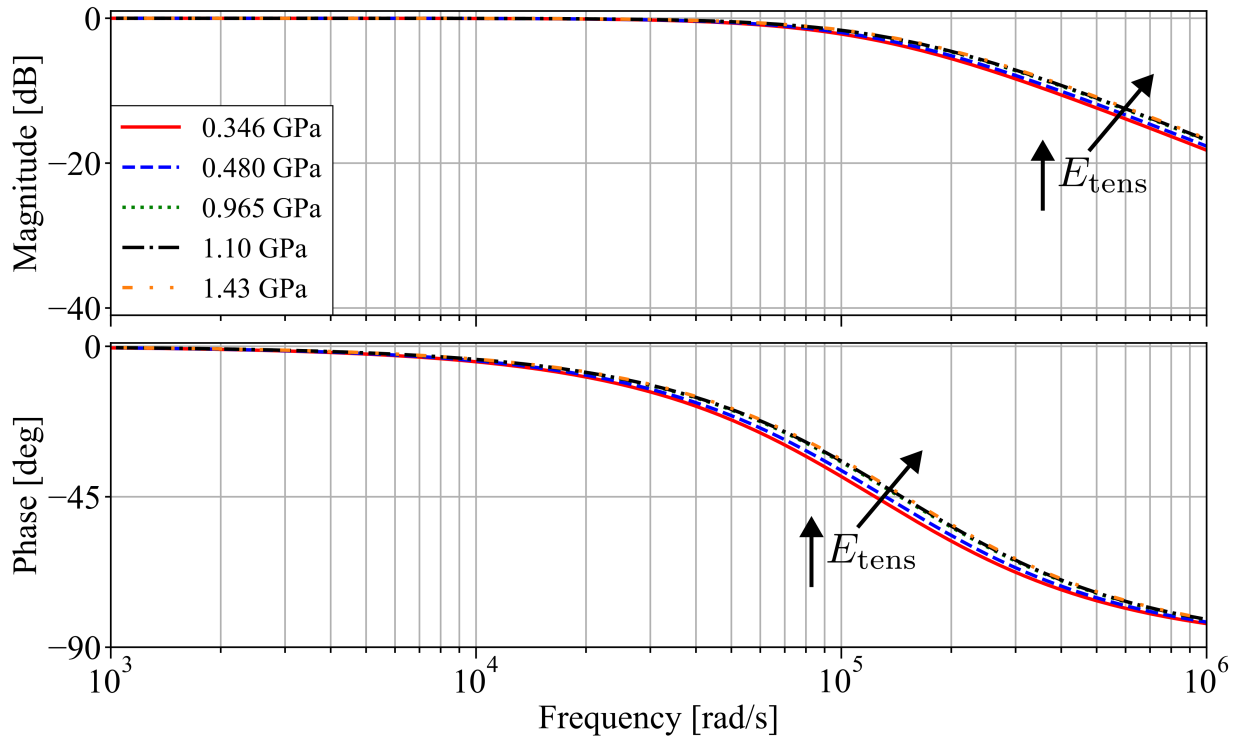


Figure 4.23: FR's of governing TF for first-order RC HECM, $G_C(s)$, for increasing E_{tens} . Wong et al.'s (2.3) compliance model considered.

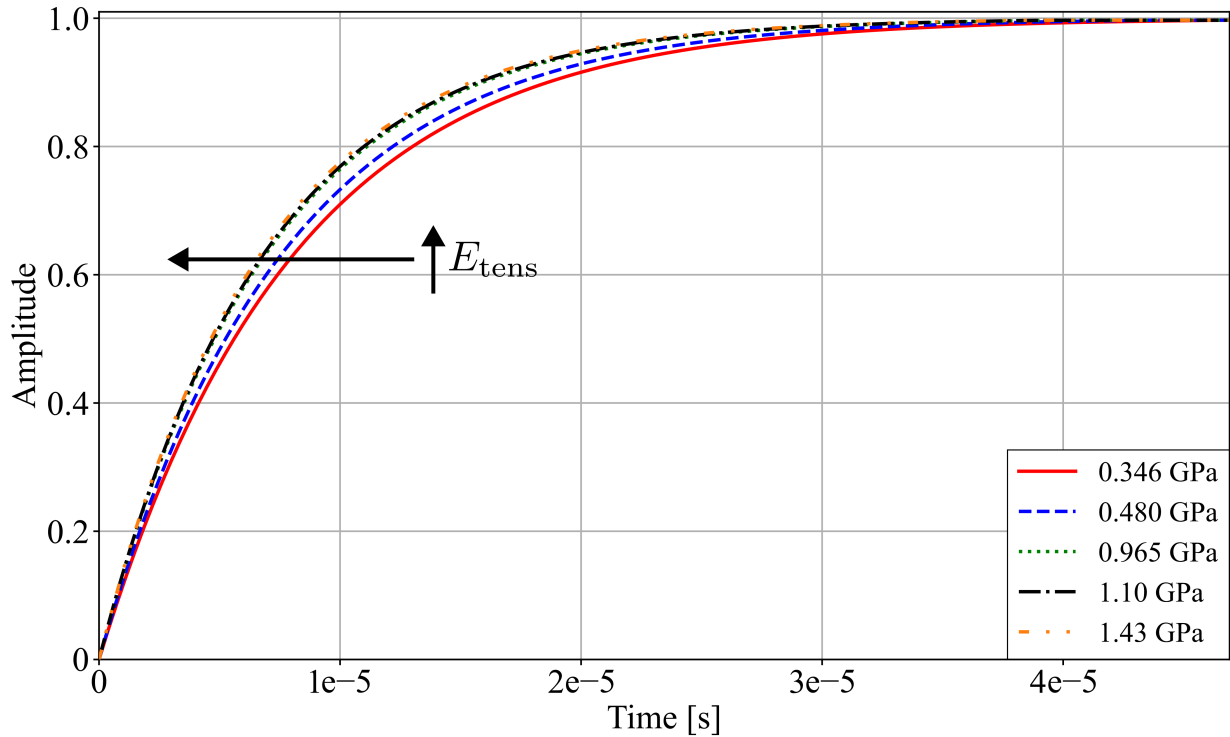


Figure 4.24: Simulated step responses for governing TF for first-order RC HECM, $G_C(s)$, for increasing tubing E_{tens} . Wong et al.’s (2.3) compliance model considered.

4.3.3 Summary

Quantitative Performance of the HECM

The HECM should not be used to quantitatively model the sample tubing dynamics in PDMFCS plant. As the assumption of steady-state flow inherent to its derivation results in the HECM significantly underestimating the time for the fluid within the sample tubing to reach a hydrodynamic steady-state. Dynamically, this manifests as considerably larger corner frequencies and faster transients than what were found in the experimental characterization of the pressure transient dynamics across the sample tubing. Therefore, the use of the HECM to approximate the sample tubing dynamics in the PDMFCS plant model results in inaccurate modelling of the sample tubing dynamics, which will cause significant difficulty in performing stability and transient response analysis of the system, impeding progress towards an informed and robust control system design methodology and modu-

larity for the PDMFCS. To allow for an informed and robust design, and the subsequent modularity, of the PDMFCS, the sample tubing dynamics should be approximated in the PDMFCS plant model using the experimentally estimated TF of (4.1), with its parameters estimated using the experimental methodology described in Chapter 3, such that more accurate stability and dynamic response analysis can be performed.

Qualitative Performance of the HECM

The first-order form of the HECM qualitatively models the experimentally observed dynamic effects of varying sample tubing and fluid parameters. The ability of the first-order HECM to qualitatively capture this variation within a first-order model presents an opportunity for future studies exploring the possibility of developing an empirical correction factor for the model from TF's experimentally estimated using the methodology outlined in Chapter 3. Given that the current experimental setup cannot effectively measure pressure waves across smaller ID tubing, improvements to the setup must be made to explore this research direction.

Chapter 5

Conclusion & Recommendations

5.1 Conclusion

Development of experimental methods to empirically characterize the dynamics associated with the plant components in the pressure-driven droplet microfluidic feedback control system (PDMFCS) will allow for the implementation of a more accurate plant model in the PDMFCS, which will result in increased accuracy in the stability and dynamic response analyses of the system. Improved system analysis accuracy allows for the development of an informed and robust control system design procedure, which will progress the PDMFCS towards modularity. Given that the sample tubing was yet to be experimentally characterized in the context of the PDMFCS, the objectives of this study were to develop a methodology to experimentally characterize the pressure transient dynamics across the sample tubing with a 95% confidence in the parameter values, quantify the effect of varying the tubing and fluid properties on the pressure transient dynamics, and compare the experimentally characterized dynamics to those predicted by the hydrodynamic equivalent circuit model (HECM) previously used to approximate the sample tubing dynamics.

To experimentally characterize the pressure transient dynamics across the sample tubing in the PDMFCS plant, sinusoidal pressure waves were measured using pressure sensors integrated at the inlet and outlet of the sample tubing to obtain an experimental frequency response (FR) of the input-output pressure transient dynamics, from which a transfer function (TF) was estimated. Uncertainties in the measured and calculated values were determined at the 95% confidence level using standard propagation of uncertainty techniques. With this methodology, it was found that the pressure transient dynamics across the sample tubing could be characterized as an approximately linear first-order TF with transport

lag. Comparing this experimentally estimated model to the HECM showed that the HECM fails to quantitatively approximate the sample tubing dynamics by overestimating the corner frequencies and underestimating the transient response characteristics present in the real system. Thus, the experimentally estimated TF should be used instead of the HECM to approximate the sample tubing dynamics in the PDMFCS plant model, as the use of the HECM for the sample tubing will result in inaccurate dynamic response and stability analyses of the PDMFCS, which hinders the advancement towards an informed and robust control system design and modularity for the PDMFCS. By assessing the effect of varying tubing and flow properties on the dynamic response, it was observed that decreasing the mean flow pressure, increasing the tubing length to diameter ratio, or increasing the fluid viscosity results in a decrease in the corner frequency and an increase in the time constant of the response. In comparison to the geometric and viscosity effects, the effect of mean pressure was not significant over small pressure changes. Similar qualitative observations were made with the first-order forms of the HECM, indicating that there is potential for a correction factor for the first-order forms of the HECM to be developed from a larger empirical dataset, similar to what has been done for TFs modelling other dynamic systems [115, 116]. A definitive conclusion could not be made on the effect of the tubing material stiffness, due to the low diameter ratio between the sample tubing and pressure sensor junctions present in this specific parameter test inducing significant expansion/contraction losses. Where the large magnitude of these losses resulted in physically unrealistic flow conditions and large uncertainties in the FR values.

Primary limitations of this study were related to the experimental setup. First, the use of standard size pressure sensors required the use of pressure sensor junctions to integrate the sensors with the sample tubing. Using these junctions resulted in expansion/contraction losses in the flow due to differences in the tubing and junction inner diameter. If these losses were not minimized, they had a detrimental effect on the physical realism of the flow resulting in an unrealistic characterization of the pressure transient dynamics across the sample tubing and larger measurement uncertainties. The other prominent limitation results from sampling the analog measurements of the pressure sensors for digital manipulation and storage. Where, the increased noise present in the measurements of the high-frequency waves, and the lack of additional low-pass filtering to these measurements, increased the uncertainty in the magnitude and phase FR at these frequencies, which affected the accuracy of the estimated TF's parameters.

5.2 Recommendations

Improvement to the experimental setup is necessary such that expansion/contraction losses are minimized, and the methodology can be effectively applied to microfluidic tubing with an inner diameter of size less than $764\ \mu\text{m}$ and tubing of various wall thickness. Minimizing expansion/contraction losses will improve the physical realism of the dynamic characterization. Meanwhile, widening the scope of the tubing that can be characterized with the setup will allow this methodology to be used for a wide range of PDMFCS designs across different applications which may differ in the tubing geometric properties. Further, this will allow the dynamic effect of wall thickness and material stiffness to be explored. As well, characterization of a range of tubing inner diameters, wall thicknesses, and materials, in conjunction with the length and viscosity characterizations, may allow the development of an empirical correction factor to the first-order HECM, and/or the quantification of uncertainty bounds for a robust control design [53]. Potential ways to improve the setup include purchasing/developing pressure sensors that are on the same scale as the microfluidic tubing, improving the manufacturing method of the pressure sensor junctions such that smaller diameter channels can be produced, manufacturing multiple junctions that together cover the range of possible tubing inner diameters and wall thicknesses, and quantifying the effect of the entrance and exit losses on the flow. Low pass-filtering can also be added to the setup to increase the accuracy of the FR estimation at higher frequencies.

A direct extension to this study would be to compare the experimental results to other pressure transient models present in the fluid mechanics literature. This would allow an assessment to be made on whether or not any of these previously developed analytical dynamic models can be used to approximate the empirical model quantified in this study. Another extension would be to explore the effect of the downstream microfluidic chip on the pressure transient dynamics of the sample tubing. Experiments designed to measure the dynamic effect of variation of the chip material and geometry with fixed tubing parameters should be executed, such that the effects of specific microfluidic setups on PDMFCS performance can be further evaluated.

In the broader context of experimentally characterizing the dynamics of other PDMFCS plant components, although briefly explored by Hébert et al. [57] and Zabloutny [48], rigorous experimental tests to assess the on-chip dynamics are yet to be performed. Ideally, experiments would be developed to empirically characterize the pressure-input displacement-output dynamics on the microfluidic chip. Notably, these dynamics are multi-input multi-output, so significant care and thought would have to be taken in the design of the experiments to assess these dynamics, where more advanced time and/or frequency domain system identification techniques would have to be employed [69]. Further, these

tests should quantify how variation in the chip geometry and material, as well as fluid properties, affects the on-chip dynamics, as microfluidic chip design is very application dependent.

Letters of Copyright Permission

Presented below are the letters of copyright permission granted by publishers to reprint Figures 1.1, 1.3, 1.4, 1.5, and 1.6. Permissions/licenses are printed in the same order as the figures appear in Chapter 1.

AAAS permits the use of content published in its journals *Science*, *Science Immunology*, *Science Robotics*, *Science Signaling*, and *Science Translational Medicine* to be used in a thesis or dissertation, but only provided the following criteria are met:

1. If you are using figure(s)/table(s), permission is granted for use in print and electronic versions of your dissertation or thesis.
2. A full-text article may be used only in print versions of a dissertation or thesis. AAAS does not permit the reproduction of full-text articles in electronic versions of theses or dissertations.
3. The following credit line must be printed along with the AAAS material: "From [Full Reference Citation]. Reprinted with permission from AAAS."
4. All required credit lines and notices must be visible any time a user accesses any part of the AAAS material and must appear on any printed copies that an authorized user might make.
5. The AAAS material may not be modified or altered, with the exception that figures and tables may be modified with permission from the author. Author permission for any such changes must be secured prior to your use.
6. AAAS must publish the full paper prior to your use of any of its text or figures.
7. If the AAAS material covered by this permission was published in *Science* during the years 1974–1994, you must also obtain permission from the author, who may grant or withhold permission, and who may or may not charge a fee if permission is granted. See original article for author's address. This condition does not apply to news articles.
8. If you are an original author of the AAAS article being reproduced, please refer to your License to Publish for rules on reproducing your paper in a dissertation or thesis.
9. Permission covers the distribution of your dissertation or thesis on demand by a third-party distributor (e.g., ProQuest/UMI), provided the AAAS material covered by this permission remains in situ and is not distributed by that third party outside of the context of your thesis/dissertation.
10. Permission does not apply to figures/photos/artwork or any other content or materials included in your work that are credited to non-AAAS sources. If the requested material is sourced to or references non-AAAS sources, you must obtain authorization from that source as well before using that material. You agree to hold harmless and indemnify AAAS against any claims arising from your use of any content in your work that is credited to non-AAAS sources.
11. By using the AAAS material identified in your request, you agree to abide by all the terms and conditions herein.
12. AAAS makes no representations or warranties as to the accuracy of any information contained in the AAAS material covered by this permission, including any warranties of merchantability or fitness for a particular purpose.

AIP PUBLISHING LICENSE TERMS AND CONDITIONS

Nov 05, 2024

This Agreement between Dylan Hahn ("You") and AIP Publishing ("AIP Publishing") consists of your license details and the terms and conditions provided by AIP Publishing and Copyright Clearance Center.

License Number	5821981313941
License date	Jul 04, 2024
Licensed Content Publisher	AIP Publishing
Licensed Content Publication	Applied Physics Letters
Licensed Content Title	Hydrodynamically mediated breakup of droplets in microchannels
Licensed Content Author	Che, Zhizhao; Nguyen, Nam-Trung
Licensed Content Date	Feb 4, 2011
Licensed Content Volume	98
Licensed Content Issue	5
Type of Use	Thesis/Dissertation
Requestor type	Student
Format	Electronic
Portion	Figure/Table
Number of figures/tables	1
Will you be translating?	No
Title of new work	Experimental Characterization of Sample Tubing Dynamics for the Improvement of Feedback Droplet Microfluidic Control Systems
Institution name	University of Waterloo
Expected presentation date	Sep 2024
Portions	Figure 1
The Requesting Person / Organization to Appear on the License	Dylan Hahn
Requestor Location	University of Waterloo [REDACTED] [REDACTED] [REDACTED]
Order reference number	10005678
Billing Type	Invoice
Billing Address	University of Waterloo [REDACTED] [REDACTED] [REDACTED]
Total	0.00 CAD

ELSEVIER LICENSE TERMS AND CONDITIONS

Nov 05, 2024

This Agreement between Dylan Hahn ("You") and Elsevier ("Elsevier") consists of your license details and the terms and conditions provided by Elsevier and Copyright Clearance Center.

License Number	5822021277616
License date	Jul 04, 2024
Licensed Content Publisher	Elsevier
Licensed Content Publication	Sensors and Actuators B: Chemical
Licensed Content Title	Selective droplet splitting using single layer microfluidic valves
Licensed Content Author	Mohammad Reza Raveshi, Sagar N. Agnihotri, Muhsincan Sesen, Rajneesh Bhardwaj, Adrian Neild
Licensed Content Date	Aug 1, 2019
Licensed Content Volume	292
Licensed Content Issue	n/a
Licensed Content Pages	8
Start Page	233
End Page	240
Type of Use	reuse in a thesis/dissertation
Portion	figures/tables/illustrations
Number of figures/tables/illustrations	1
Format	electronic
Are you the author of this Elsevier article?	No
Will you be translating?	No
Title of new work	Experimental Characterization of Sample Tubing Dynamics for the Improvement of Feedback Droplet Microfluidic Control Systems
Institution name	University of Waterloo
Expected presentation date	Sep 2024
Portions	Graphical Abstract
The Requesting Person / Organization to Appear on the License	Dylan Hahn
Requestor Location	University of Waterloo [REDACTED] [REDACTED] [REDACTED]
Order reference number	10007456
Publisher Tax ID	GB 494 6272 12
Total	0.00 CAD

Order Details

1. Lab on a chip

Article: Pillar-induced droplet merging in microfluidic circuits.

Billing Status:
Open

[Print License](#)

Order License ID	1538430-1	Type of Use	Republish in a thesis/dissert...
Order detail status	Completed	Publisher	ROYAL SOCIETY OF CHEMIS...
ISSN	1473-0189	Portion	Image/photo/illustration

0.00 CAD

Republication Permission

[Hide Details](#)

LICENSED CONTENT

Publication Title	Lab on a chip	Rightsholder	Royal Society of Chemistry
Article Title	Pillar-induced droplet mergi...	Publication Type	e-Journal
Author / Editor	Royal Society of Chemistry (...)	Start Page	1837
Date	01/01/2001	Issue	11
Language	English	Volume	8
Country	United Kingdom of Great Bri...	URL	http://www.rsc.org/loc

REQUEST DETAILS

Portion Type	Image/photo/illustration	Distribution	Worldwide
Number of Images / Photos / Illustrations	1	Translation	Original language of publica...
Format (select all that apply)	Print, Electronic	Copies for the Disabled?	Yes
Who Will Republish the Content?	Academic institution	Minor Editing Privileges?	Yes
Duration of Use	Life of current edition	Incidental Promotional Use?	No
Lifetime Unit Quantity	Up to 499	Currency	CAD
Rights Requested	Main product		

NEW WORK DETAILS

Title	Experimental Characterizati...	Institution Name	University of Waterloo
Instructor Name	Carolyn Ren	Expected Presentation Date	2024-10-23

ADDITIONAL DETAILS

Order Reference Number	098765	The Requesting Person / Organization to Appear on the License	Dylan Hahn
------------------------	--------	---	------------

REQUESTED CONTENT DETAILS

Title, Description or Numeric Reference of the Portion(s)	Figure 2 a)	Title of the Article / Chapter the Portion Is From	Pillar-induced droplet mergi...
Editor of Portion(s)	Niu, Xize; Gulati, Shelly; Edel...	Author of Portion(s)	Niu, Xize; Gulati, Shelly; Edel...
Volume / Edition	8	Issue, if Republishing an Article From a Serial	11
Page or Page Range of Portion	1837	Publication Date of Portion	2008-10-31

Total Items: 1

Subtotal: 0.00 CAD

Order Total: 0.00 CAD

This is a License Agreement between Dylan Hahn ("User") and Copyright Clearance Center, Inc. ("CCC") on behalf of the Rightsholder identified in the order details below. The license consists of the order details, the Marketplace Permissions General Terms and Conditions below, and any Rightsholder Terms and Conditions which are included below. All payments must be made in full to CCC in accordance with the Marketplace Permissions General Terms and Conditions below.

Order Date	22-Oct-2024	Type of Use	Republish in a thesis/dissertation
Order License ID	1538430-1	Publisher	ROYAL SOCIETY OF CHEMISTRY
ISSN	1473-0189	Portion	Image/photo/illustration

LICENSED CONTENT

Publication Title	Lab on a chip	Rightsholder	Royal Society of Chemistry
Article Title	Pillar-induced droplet merging in microfluidic circuits.	Publication Type	e-Journal
Author / Editor	Royal Society of Chemistry (Great Britain)	Start Page	1837
Date	01/01/2001	Issue	11
Language	English	Volume	8
Country	United Kingdom of Great Britain and Northern Ireland	URL	http://www.rsc.org/loc

REQUEST DETAILS

Portion Type	Image/photo/illustration	Distribution	Worldwide
Number of Images / Photos / Illustrations	1	Translation	Original language of publication
Format (select all that apply)	Print, Electronic	Copies for the Disabled?	Yes
Who Will Republish the Content?	Academic institution	Minor Editing Privileges?	Yes
Duration of Use	Life of current edition	Incidental Promotional Use?	No
Lifetime Unit Quantity	Up to 499	Currency	CAD
Rights Requested	Main product		

NEW WORK DETAILS

Title	Experimental Characterization of Sample Tubing Dynamics for the Improvement of Droplet Microfluidic Feedback Control Systems	Institution Name	University of Waterloo
Instructor Name	Carolyn Ren	Expected Presentation Date	2024-10-23

ADDITIONAL DETAILS

Order Reference Number	098765	The Requesting Person / Organization to Appear on the License	Dylan Hahn
------------------------	--------	---	------------

REQUESTED CONTENT DETAILS

Title, Description or Numeric Reference of the Portion(s)	Figure 2 a)	Title of the Article / Chapter the Portion Is From	Pillar-induced droplet merging in microfluidic circuits.
Editor of Portion(s)	Niu, Xize; Gulati, Shelly; Edel, Joshua B.; deMello, Andrew J.	Author of Portion(s)	Niu, Xize; Gulati, Shelly; Edel, Joshua B.; deMello, Andrew J.
Volume / Edition	8	Issue, if Republishing an Article From a Serial	11
Page or Page Range of Portion	1837	Publication Date of Portion	2008-10-31

Order Details

1. Lab on a chip

Article: EWOD (electrowetting on dielectric) digital microfluidics powered by finger actuation.

Billing Status:
Open

[Print License](#)

Order License ID	1538433-1	Type of Use	Republish in a thesis/dissert...
Order detail status	Completed	Publisher	ROYAL SOCIETY OF CHEMIS...
ISSN	1473-0189	Portion	Image/photo/illustration
			0.00 CAD
			Republication Permission

[Hide Details](#)

LICENSED CONTENT

Publication Title	Lab on a chip	Rights holder	Royal Society of Chemistry
Article Title	EWOD (electrowetting on di...	Publication Type	e-Journal
Author / Editor	Royal Society of Chemistry (...)	Start Page	1117
Date	01/01/2001	Issue	6
Language	English	Volume	14
Country	United Kingdom of Great Bri...	URL	http://www.rsc.org/loc

REQUEST DETAILS

Portion Type	Image/photo/illustration	Distribution	Worldwide
Number of Images / Photos / Illustrations	1	Translation	Original language of publica...
Format (select all that apply)	Print, Electronic	Copies for the Disabled?	Yes
Who Will Republish the Content?	Academic institution	Minor Editing Privileges?	Yes
Duration of Use	Life of current edition	Incidental Promotional Use?	No
Lifetime Unit Quantity	Up to 499	Currency	CAD
Rights Requested	Main product		

NEW WORK DETAILS

Title	Experimental Characterizati...	Institution Name	University of Waterloo
Instructor Name	Carolyn Ren	Expected Presentation Date	2024-10-23

ADDITIONAL DETAILS

Order Reference Number	098766	The Requesting Person / Organization to Appear on the License	Dylan Hahn
------------------------	--------	---	------------

REQUESTED CONTENT DETAILS

Title, Description or Numeric Reference of the Portion(s)	Figure 1	Title of the Article / Chapter the Portion Is From	EWOD (electrowetting on di...
Editor of Portion(s)	Peng, Cheng; Zhang, Zhong...	Author of Portion(s)	Peng, Cheng; Zhang, Zhong...
Volume / Edition	14	Issue, if Republishing an Article From a Serial	6
Page or Page Range of Portion	1117	Publication Date of Portion	2014-03-20

Total Items: 1

Subtotal: 0.00 CAD
Order Total: 0.00 CAD

This is a License Agreement between Dylan Hahn ("User") and Copyright Clearance Center, Inc. ("CCC") on behalf of the Rightsholder identified in the order details below. The license consists of the order details, the Marketplace Permissions General Terms and Conditions below, and any Rightsholder Terms and Conditions which are included below. All payments must be made in full to CCC in accordance with the Marketplace Permissions General Terms and Conditions below.

Order Date	22-Oct-2024	Type of Use	Republish in a thesis/dissertation
Order License ID	1538433-1	Publisher	ROYAL SOCIETY OF CHEMISTRY
ISSN	1473-0189	Portion	Image/photo/illustration

LICENSED CONTENT

Publication Title	Lab on a chip	Rightsholder	Royal Society of Chemistry
Article Title	EWOD (electrowetting on dielectric) digital microfluidics powered by finger actuation.	Publication Type	e-Journal
Author / Editor	Royal Society of Chemistry (Great Britain)	Start Page	1117
Date	01/01/2001	Issue	6
Language	English	Volume	14
Country	United Kingdom of Great Britain and Northern Ireland	URL	http://www.rsc.org/loc

REQUEST DETAILS

Portion Type	Image/photo/illustration	Distribution	Worldwide
Number of Images / Photos / Illustrations	1	Translation	Original language of publication
Format (select all that apply)	Print, Electronic	Copies for the Disabled?	Yes
Who Will Republish the Content?	Academic institution	Minor Editing Privileges?	Yes
Duration of Use	Life of current edition	Incidental Promotional Use?	No
Lifetime Unit Quantity	Up to 499	Currency	CAD
Rights Requested	Main product		

NEW WORK DETAILS

Title	Experimental Characterization of Sample Tubing Dynamics for the Improvement of Droplet Microfluidic Feedback Control Systems	Institution Name	University of Waterloo
Instructor Name	Carolyn Ren	Expected Presentation Date	2024-10-23

ADDITIONAL DETAILS

Order Reference Number	098766	The Requesting Person / Organization to Appear on the License	Dylan Hahn
------------------------	--------	---	------------

REQUESTED CONTENT DETAILS

Title, Description or Numeric Reference of the Portion(s)	Figure 1	Title of the Article / Chapter the Portion Is From	EWOD (electrowetting on dielectric) digital microfluidics powered by finger actuation.
Editor of Portion(s)	Peng, Cheng; Zhang, Zhongning; Kim, Chang-jin "CJ"; Ju, Y. Sungtaek	Author of Portion(s)	Peng, Cheng; Zhang, Zhongning; Kim, Chang-jin "CJ"; Ju, Y. Sungtaek
Volume / Edition	14	Issue, if Republishing an Article From a Serial	6
Page or Page Range of Portion	1117	Publication Date of Portion	2014-03-20

References

- [1] P. Tabeling, *Introduction to Microfluidics*. Oxford University Press, 2023. [Online]. Available: <https://books.google.ca/books?id=uEXGEAAAQBAJ>
- [2] G. M. Whitesides, “The origins and the future of microfluidics,” *Nature*, vol. 442, pp. 368–373, 5/3/06 2006, 960.
- [3] A. Manz, N. Graber, and H. Widmer, “Miniaturized total chemical analysis systems: A novel concept for chemical sensing,” *Sensors and Actuators B: Chemical*, vol. 1, no. 1, pp. 244–248, 1990. [Online]. Available: <https://www.sciencedirect.com/science/article/pii/092540059080209I>
- [4] Y. Sun and Y. C. Kwok, “Polymeric microfluidic system for dna analysis,” *Analytica Chimica Acta*, vol. 556, no. 1, pp. 80–96, 2006, young Analytical Faculty in Asia. [Online]. Available: <https://www.sciencedirect.com/science/article/pii/S0003267005015370>
- [5] M. A. Burns, B. N. Johnson, S. N. Brahmasandra, K. Handique, J. R. Webster, M. Krishnan, T. S. Sammarco, P. M. Man, D. Jones, D. Heldsinger, C. H. Mastrangelo, and D. T. Burke, “An integrated nanoliter dna analysis device,” *Science*, vol. 282, no. 5388, pp. 484–487, 1998. [Online]. Available: <https://www.science.org/doi/abs/10.1126/science.282.5388.484>
- [6] M. L. Kovarik, D. M. Orloff, A. T. Melvin, N. C. Dobes, Y. Wang, A. J. Dickinson, P. C. Gach, P. K. Shah, and N. L. Allbritton, “Micro total analysis systems: Fundamental advances and applications in the laboratory, clinic, and field,” *Analytical Chemistry*, vol. 85, no. 2, pp. 451–472, 2013, PMID: 23140554. [Online]. Available: <https://doi.org/10.1021/ac3031543>
- [7] E. Gal-Or, Y. Gershoni, G. Scotti, S. M. E. Nilsson, J. Saarinen, V. Jokinen, C. J. Strachan, G. Boije af Gennäs, J. Yli-Kauhaluoma, and T. Kotiaho, “Chemical

- analysis using 3d printed glass microfluidics,” *Anal. Methods*, vol. 11, pp. 1802–1810, 2019. [Online]. Available: <http://dx.doi.org/10.1039/C8AY01934G>
- [8] M. E. Warkiani, B. L. Khoo, L. Wu, A. K. P. Tay, A. A. S. Bhagat, J. Han, and C. T. Lim, “Ultra-fast, label-free isolation of circulating tumor cells from blood using spiral microfluidics,” *Nature Protocols*, vol. 11, no. 1, pp. 134–148, Jan 2016. [Online]. Available: <https://doi.org/10.1038/nprot.2016.003>
- [9] A. Jaber, A. Monemian Esfahani, F. Aghabaglou, J. S. Park, S. Ndao, A. Tamayol, and R. Yang, “Microfluidic systems with embedded cell culture chambers for high-throughput biological assays,” *ACS Applied Bio Materials*, vol. 3, no. 10, pp. 6661–6671, Oct 2020. [Online]. Available: <https://doi.org/10.1021/acsabm.0c00439>
- [10] B. Xiong, K. Ren, Y. Shu, Y. Chen, B. Shen, and H. Wu, “Recent developments in microfluidics for cell studies,” *Advanced Materials*, vol. 26, no. 31, pp. 5525–5532, 2014. [Online]. Available: <https://onlinelibrary.wiley.com/doi/abs/10.1002/adma.201305348>
- [11] M. Hébert, J. Huissoon, and C. L. Ren, “A perspective of active microfluidic platforms as an enabling tool for applications in other fields,” *Journal of Micromechanics and Microengineering*, vol. 32, no. 4, p. 043001, mar 2022. [Online]. Available: <https://dx.doi.org/10.1088/1361-6439/ac545f>
- [12] S.-Y. Teh, R. Lin, L.-H. Hung, and A. P. Lee, “Droplet microfluidics,” *Lab Chip*, vol. 8, pp. 198–220, 2008. [Online]. Available: <http://dx.doi.org/10.1039/B715524G>
- [13] T. Moragues, D. Arguijo, T. Beneyton, C. Modavi, K. Simutis, A. R. Abate, J.-C. Baret, A. J. deMello, D. Densmore, and A. D. Griffiths, “Droplet-based microfluidics,” *Nature Reviews Methods Primers*, vol. 3, no. 1, p. 32, Apr 2023. [Online]. Available: <https://doi.org/10.1038/s43586-023-00212-3>
- [14] H. Gu, M. H. G. Duits, and F. Mugele, “Droplets formation and merging in two-phase flow microfluidics,” *International Journal of Molecular Sciences*, vol. 12, no. 4, pp. 2572–2597, 2011. [Online]. Available: <https://www.mdpi.com/1422-0067/12/4/2572>
- [15] G. F. Christopher and S. L. Anna, “Microfluidic methods for generating continuous droplet streams,” *Journal of Physics D: Applied Physics*, vol. 40, no. 19, p. R319, sep 2007. [Online]. Available: <https://dx.doi.org/10.1088/0022-3727/40/19/R01>

- [16] Q. Kang, D. Zhang, and S. Chen, “Displacement of a two-dimensional immiscible droplet in a channel,” *Physics of Fluids*, vol. 14, no. 9, pp. 3203–3214, 09 2002. [Online]. Available: <https://doi.org/10.1063/1.1499125>
- [17] J. D. Tice, H. Song, , A. D. Lyon, and R. F. Ismagilov, “Formation of droplets and mixing in multiphase microfluidics at low values of the reynolds and the capillary numbers,” *Langmuir*, vol. 19, pp. 9127–9133, 2003. [Online]. Available: <https://api.semanticscholar.org/CorpusID:6867150>
- [18] T. Glawdel, “Droplet production and transport in microfluidic networks with pressure driven flow control,” 2012.
- [19] M. Hébert and C. L. Ren, “4 - droplet microfluidics for biomedical devices,” in *Microfluidic Devices for Biomedical Applications (Second Edition)*, second edition ed., ser. Woodhead Publishing Series in Biomaterials, X. J. Li and Y. Zhou, Eds. Woodhead Publishing, 2021, pp. 163–204. [Online]. Available: <https://www.sciencedirect.com/science/article/pii/B9780128199718000019>
- [20] H. Lee, “Droplet-based microfluidic platform for immunoassay applications using magnetic particles,” United States – New York, p. 140, 2015, copyright - Database copyright ProQuest LLC; ProQuest does not claim copyright in the individual underlying works. [Online]. Available: <https://proxy.lib.uwaterloo.ca/login?url=https://www.proquest.com/dissertations-theses/droplet-based-microfluidic-platform-immunoassay/docview/1709470026/se-2?accountid=14906>
- [21] P. Zhu and L. Wang, “Passive and active droplet generation with microfluidics: a review,” *Lab Chip*, vol. 17, pp. 34–75, 2017. [Online]. Available: <http://dx.doi.org/10.1039/C6LC01018K>
- [22] M. Hebert, “Expanding the droplet microfluidic community—towards a modular active platform,” 2020.
- [23] Z. Che, N.-T. Nguyen, and T. N. Wong, “Hydrodynamically mediated breakup of droplets in microchannels,” *Applied Physics Letters*, vol. 98, no. 5, p. 054102, 02 2011. [Online]. Available: <https://doi.org/10.1063/1.3552680>
- [24] X. Niu, S. Gulati, J. B. Edel, and A. J. deMello, “Pillar-induced droplet merging in microfluidic circuits,” *Lab Chip*, vol. 8, pp. 1837–1841, 2008. [Online]. Available: <http://dx.doi.org/10.1039/B813325E>

- [25] M. R. Raveshi, S. N. Agnihotri, M. Sesen, R. Bhardwaj, and A. Neild, "Selective droplet splitting using single layer microfluidic valves," *Sensors and Actuators B: Chemical*, vol. 292, pp. 233–240, 2019. [Online]. Available: <https://www.sciencedirect.com/science/article/pii/S0925400519306483>
- [26] S. C. C. Shih, R. Fobel, P. Kumar, and A. R. Wheeler, "A feedback control system for high-fidelity digital microfluidics," *Lab Chip*, vol. 11, pp. 535–540, 2011. [Online]. Available: <http://dx.doi.org/10.1039/C0LC00223B>
- [27] G.-P. Zhu, Q.-Y. Wang, Z.-K. Ma, S.-H. Wu, and Y.-P. Guo, "Droplet manipulation under a magnetic field: A review," *Biosensors*, vol. 12, no. 3, 2022. [Online]. Available: <https://www.mdpi.com/2079-6374/12/3/156>
- [28] P. Li, Z. Ma, Y. Zhou, D. J. Collins, Z. Wang, and Y. Ai, "Detachable acoustophoretic system for fluorescence-activated sorting at the single-droplet level," *Analytical Chemistry*, vol. 91, no. 15, pp. 9970–9977, 2019, pMID: 31179691. [Online]. Available: <https://doi.org/10.1021/acs.analchem.9b01708>
- [29] Z. Wang, R. Chen, X. Zhu, Q. Liao, D. Ye, B. Zhang, X. He, and W. Li, "Control of the droplet generation by an infrared laser," *AIP Advances*, vol. 8, no. 1, p. 015302, 01 2018. [Online]. Available: <https://doi.org/10.1063/1.5007127>
- [30] C. Peng, Z. Zhang, C.-J. im, and Y. S. Ju, "Ewod (electrowetting on dielectric) digital microfluidics powered by finger actuation," *Lab Chip*, vol. 14, pp. 1117–1122, 2014. [Online]. Available: <http://dx.doi.org/10.1039/C3LC51223A>
- [31] A. Ray, V. B. Varma, Z. Wang, Z. Wang, P. J. Jayaneel, N. M. Sudharsan, and R. V. Ramanujan, "Magnetic droplet merging by hybrid magnetic fields," *IEEE Magnetics Letters*, vol. 7, pp. 1–5, 2016.
- [32] D. Cheng, X. Li, G. Zhang, and H. Shi, "Morphological effect of oscillating magnetic nanoparticles in killing tumor cells," *Nanoscale Research Letters*, vol. 9, no. 1, p. 195, Apr 2014. [Online]. Available: <https://doi.org/10.1186/1556-276X-9-195>
- [33] G. Yesiloz, M. S. Boybay, and C. L. Ren, "Effective thermo-capillary mixing in droplet microfluidics integrated with a microwave heater," *Analytical Chemistry*, vol. 89, no. 3, pp. 1978–1984, 2017, pMID: 28029032. [Online]. Available: <https://doi.org/10.1021/acs.analchem.6b04520>
- [34] D. R. Link, E. Grasland-Mongrain, A. Duri, F. Sarrazin, Z. Cheng, G. Cristobal, M. Marquez, and D. A. Weitz, "Electric control of droplets in microfluidic

- devices,” *Angewandte Chemie International Edition*, vol. 45, no. 16, pp. 2556–2560, 2006. [Online]. Available: <https://onlinelibrary.wiley.com/doi/abs/10.1002/anie.200503540>
- [35] D. Wong and C. L. Ren, “Microfluidic droplet trapping, splitting and merging with feedback controls and state space modelling,” *Lab Chip*, vol. 16, pp. 3317–3329, 2016. [Online]. Available: <http://dx.doi.org/10.1039/C6LC00626D>
- [36] D. Wong, K. Erkorkmaz, and C. L. Ren, “Robodrop: A multi-input multi-output control system for on-demand manipulation of microfluidic droplets based on computer vision feedback,” *IEEE/ASME Transactions on Mechatronics*, vol. 25, no. 2, pp. 1129–1137, 2020.
- [37] Y. H. Wong, “Feedback controls in droplet microfluidics,” Master’s thesis, University of Waterloo, 2016.
- [38] D. A. Rubenstein, W. Yin, and M. D. Frame, “Chapter 2 - fundamentals of fluid mechanics,” in *Biofluid Mechanics (Second Edition)*, second edition ed., ser. Biomedical Engineering, D. A. Rubenstein, W. Yin, and M. D. Frame, Eds. Boston: Academic Press, 2015, pp. 15–62. [Online]. Available: <https://www.sciencedirect.com/science/article/pii/B9780128009444000020>
- [39] G. Franklin, J. Powell, and A. Emami-Naeini, *Feedback Control of Dynamic Systems*. Pearson Prentice Hall, 2006. [Online]. Available: <https://books.google.ca/books?id=NhAoAQAAMAAJ>
- [40] Einst. ”Andor Zyla 5.5 SCMOS Camera” www.einstinc.com. [Online]. Available: <https://www.einstinc.com/wpcproduct/andor-zyla-5-5-scmos-camera/>
- [41] Nikon. ”ECLIPSE Ti Series” www.microscope.healthcare.nikon.com. [Online]. Available: <https://www.microscope.healthcare.nikon.com/products/inverted-microscopes/eclipse-ti-series>
- [42] Fluigent. ”Microfluidic Flow Control System MFCS series” www.fluigent.com. [Online]. Available: <https://www.fluigent.com/research/instruments/pressure-flow-controllers/mfcs-series/#spec>
- [43] M. Hébert, M. Courtney, and C. L. Ren, “Semi-automated on-demand control of individual droplets with a sample application to a drug screening assay,” *Lab Chip*, vol. 19, pp. 1490–1501, 2019. [Online]. Available: <http://dx.doi.org/10.1039/C9LC00128J>

- [44] M. Hébert, W. Baxter, J. P. Huissoon, and C. L. Ren, “A quantitative study of the dynamic response of soft tubing for pressure-driven flow in a microfluidics context,” *Microfluidics and Nanofluidics*, vol. 24, pp. 1–13, 2020.
- [45] R. Z. Gao, M. Hébert, J. Huissoon, and C. L. Ren, “ μ pump: An open-source pressure pump for precision fluid handling in microfluidics,” *HardwareX*, vol. 7, p. e00096, 2020. [Online]. Available: <https://www.sciencedirect.com/science/article/pii/S2468067220300043>
- [46] T. Zabloutny, M. Courtney, J. P. Huissoon, and C. L. Ren, “Lensless imaging for droplet identification towards visual feedback-based pressure controlled droplet microfluidic platforms,” *Sensors and Actuators A: Physical*, vol. 334, p. 113338, 2022.
- [47] H. Chen, “Enabling practical and accessible automatic droplet microfluidics platforms,” Master’s thesis, University of Waterloo, 2023.
- [48] T. Zabloutny, “Towards feedback controlled droplet microfluidic platforms,” Master’s thesis, University of Waterloo, 2021.
- [49] N. Nise, *Control Systems Engineering, 8e Enhanced eText with Abridged Print Companion*. Wiley, 2019.
- [50] G. F. Franklin, J. D. Powell, and M. L. Workman, *Digital Control of Dynamic Systems*, 2nd ed., ser. Electrical and Computer Engineering; Control Engineering. Reading Massachusetts: Addison-Wesley, 1990, a SRL reference.
- [51] K. Ogata, *Modern Control Engineering*, 5th ed. Prentice Hall, 2010.
- [52] R. Dorf and R. Bishop, *Modern Control Systems*. Pearson, 2011. [Online]. Available: <https://books.google.ca/books?id=Y11EbwAACAAJ>
- [53] S. Skogestad and I. Postlethwaite, *Multivariable Feedback Control: Analysis and Design*. Wiley, 2005. [Online]. Available: <https://books.google.ca/books?id=97iAEAAAQBAJ>
- [54] C.-T. Chen, *Linear System Theory and Design*, 3rd ed. USA: Oxford University Press, Inc., 1998.
- [55] C. Paige, “Properties of numerical algorithms related to computing controllability,” *IEEE Transactions on Automatic Control*, vol. 26, no. 1, pp. 130–138, 1981.

- [56] S. M. Recktenwald, C. Wagner, and T. John, “Optimizing pressure-driven pulsatile flows in microfluidic devices,” *Lab Chip*, vol. 21, pp. 2605–2613, 2021. [Online]. Available: <http://dx.doi.org/10.1039/D0LC01297A>
- [57] M. Hébert, J. Huissoon, and C. L. Ren, “A quantitative study of the dynamic response of compliant microfluidic chips in a microfluidics context,” *Journal of Micromechanics and Microengineering*, vol. 32, no. 8, p. 085004, jun 2022. [Online]. Available: <https://dx.doi.org/10.1088/1361-6439/ac7844>
- [58] *Closed-Loop Pressure Feedback Control of a Pressure-Driven Microdroplet Generator*, ser. Fluid Power Systems Technology, vol. 9th FPNI Ph.D. Symposium on Fluid Power, 10 2016. [Online]. Available: <https://doi.org/10.1115/FPNI2016-1524>
- [59] S. Vedel, “Millisecond dynamics in microfluidics: Equivalent circuit theory and experiment,” 2009.
- [60] H. Bruus, *Theoretical Microfluidics*, ser. Oxford Master Series in Physics. OUP Oxford, 2008. [Online]. Available: <https://books.google.ca/books?id=FZz3j46Fq2sC>
- [61] K. W. Oh, K. Lee, B. Ahn, and E. P. Furlani, “Design of pressure-driven microfluidic networks using electric circuit analogy,” *Lab Chip*, vol. 12, pp. 515–545, 2012. [Online]. Available: <http://dx.doi.org/10.1039/C2LC20799K>
- [62] M. S. Ghidaoui, M. Zhao, D. A. McInnis, and D. H. Axworthy, “A Review of Water Hammer Theory and Practice ,” *Applied Mechanics Reviews*, vol. 58, no. 1, pp. 49–76, 03 2005. [Online]. Available: <https://doi.org/10.1115/1.1828050>
- [63] A. S. Iberall, “Attenuation of Oscillatory Pressures in Instrument Lines,” *Transactions of the American Society of Mechanical Engineers*, vol. 72, no. 5, pp. 689–695, 07 2022. [Online]. Available: <https://doi.org/10.1115/1.4016800>
- [64] S. Tavoularis and J. Nedić, *Measurement in Fluid Mechanics*, 2nd ed. Cambridge University Press, 2024.
- [65] J. Holman, *Experimental Methods for Engineers*, ser. Economia e discipline aziendali. McGraw-Hill/Connect Learn Succeed, 2012. [Online]. Available: <https://books.google.ca/books?id=olfzygAACAAJ>
- [66] D. N. Ku, “Blood flow in arteries,” *Annual Review of Fluid Mechanics*, vol. 29, no. Volume 29, 1997, pp. 399–434, 1997. [Online]. Available: <https://www.annualreviews.org/content/journals/10.1146/annurev.fluid.29.1.399>

- [67] S. Schmid, B. Hamrock, and B. Jacobson, *Fundamentals of Machine Elements*. CRC Press, 2013. [Online]. Available: <https://books.google.ca/books?id=ypzNBQAAQBAJ>
- [68] E. Doebelin, *Measurement Systems: Application and Design*, ser. McGraw-Hill series in mechanical engineering. McGraw-Hill, 2004. [Online]. Available: <https://books.google.ca/books?id=44ORPwAACAAJ>
- [69] L. Ljung, *System identification: theory for the user*, 2nd ed. USA: Prentice Hall PTR, 1999.
- [70] A. V. Oppenheim, A. S. Willsky, and S. H. Nawab, *Signals & systems (2nd ed.)*. USA: Prentice-Hall, Inc., 1996.
- [71] J. Zhang, S. Yan, D. Yuan, G. Alici, N.-T. Nguyen, M. Ebrahimi Warkiani, and W. Li, “Fundamentals and applications of inertial microfluidics: a review,” *Lab Chip*, vol. 16, pp. 10–34, 2016. [Online]. Available: <http://dx.doi.org/10.1039/C5LC01159K>
- [72] D. Di Carlo, “Inertial microfluidics,” *Lab Chip*, vol. 9, pp. 3038–3046, 2009. [Online]. Available: <http://dx.doi.org/10.1039/B912547G>
- [73] F. White and R. Chul, *Fluid Mechanics*, ser. McGraw-Hill series in mechanical engineering. McGraw-Hill Education, 2016. [Online]. Available: <https://books.google.ca/books?id=7AEzjwEACAAJ>
- [74] Fluigent. “Microfluidic Flow Control System: MFCS series” www.fluigent.com. [Online]. Available: <https://www.fluigent.com/research/instruments/pressure-flow-controllers/mfcs-series/>
- [75] VWR. “Masterflex® Ismatec® Pump Tubing, Tygon® LMT-55, 1.30 mm ID; 33 ft” sg.vwr.com. [Online]. Available: <https://sg.vwr.com/store/item/EU7098082/masterflex-ismatec-microbore-pump-tubing-tygon-lmt-55-avantor>
- [76] Fluigent. “Fluiwell 4-Channel 2 mL Low Pressure” store.fluigent.com. [Online]. Available: <https://store.fluigent.com/products/fluiwell-4-channel-2-ml-low-pressure/>
- [77] T. Connectivity, *U5300 Industrial Pressure Transducer*. TE Connectivity, 2022.
- [78] N. Instruments. “USB-6003 Specifications” www.ni.com. [Online]. Available: <https://www.ni.com/docs/en-US/bundle/usb-6003-specs/resource/374372a.pdf>

- [79] Fluigent. "FEP Capillary Tubing (10 m)" [store.fluigent.com](https://store.fluigent.com/products/fep-capillary-tubing-10-m/). [Online]. Available: <https://store.fluigent.com/products/fep-capillary-tubing-10-m/>
- [80] W. Callister and D. Rethwisch, *Materials Science and Engineering*. Wiley, 2014. [Online]. Available: <https://books.google.ca/books?id=99UeMAEACAAJ>
- [81] IDEX. "Materials Guid" www.idex-hs.com. [Online]. Available: <https://www.idex-hs.com/resources/resources-detail/materials-guide>
- [82] SciPro. "Tubing " www.scipro.com. [Online]. Available: <https://scipro.com/product-category/idex-fluidics/tubing/>
- [83] S. Park, C. Su Jeon, N. Choi, J.-I. Moon, K. Min Lee, S. Hyun Pyun, T. Kang, and J. Choo, "Sensitive and reproducible detection of sars-cov-2 using sers-based microdroplet sensor," *Chemical Engineering Journal*, vol. 446, p. 137085, 2022. [Online]. Available: <https://www.sciencedirect.com/science/article/pii/S1385894722025773>
- [84] A. I. Segaliny, G. Li, L. Kong, C. Ren, X. Chen, J. K. Wang, D. Baltimore, G. Wu, and W. Zhao, "Functional tcr t cell screening using single-cell droplet microfluidics," *Lab Chip*, vol. 18, pp. 3733–3749, 2018. [Online]. Available: <http://dx.doi.org/10.1039/C8LC00818C>
- [85] J. Jeon, N. Choi, H. Chen, J.-I. Moon, L. Chen, and J. Choo, "Sers-based droplet microfluidics for high-throughput gradient analysis," *Lab Chip*, vol. 19, pp. 674–681, 2019. [Online]. Available: <http://dx.doi.org/10.1039/C8LC01180J>
- [86] L. M. Wilder, J. R. Thompson, and R. M. Crooks, "Electrochemical ph regulation in droplet microfluidics," *Lab Chip*, vol. 22, pp. 632–640, 2022. [Online]. Available: <http://dx.doi.org/10.1039/D1LC00952D>
- [87] N. Garg, R. Tona, P. Martin, P. M. Martin-Soladana, G. Ward, N. Douillet, and D. Lai, "Seeded droplet microfluidic system for small molecule crystallization," *Lab Chip*, vol. 20, pp. 1815–1826, 2020. [Online]. Available: <http://dx.doi.org/10.1039/D0LC00122H>
- [88] C.-M. Huang, Y. Zhu, D.-Q. Jin, R. T. Kelly, and Q. Fang, "Direct surface and droplet microsampling for electrospray ionization mass spectrometry analysis with an integrated dual-probe microfluidic chip," *Analytical Chemistry*, vol. 89, no. 17, pp. 9009–9016, 2017, pMID: 28780855. [Online]. Available: <https://doi.org/10.1021/acs.analchem.7b01679>

- [89] IDEX. "Tubing Sleeves" www.idex-hs.com. [Online]. Available: https://www.idex-hs.com/store/products/fluidics/fluidic_connections/fittings/tubing_sleeves/3
- [90] MilliporeSigma. "Silicone Oil — Sigma-Aldrich" www.sigmaaldrich.com. [Online]. Available: <https://www.sigmaaldrich.com/CA/en/search/silicone-oil?focus=products&page=1&perpage=30&sort=relevance&term=silicone%20oil&type=product>
- [91] Y. Xia and G. M. Whitesides, "Soft lithography," *Angewandte Chemie International Edition*, vol. 37, no. 5, pp. 550–575, 1998. [Online]. Available: <https://onlinelibrary.wiley.com/doi/abs/10.1002/%28SICI%291521-3773%2819980316%2937%3A5%3C550%3A%3AAID-ANIE550%3E3.0.CO%3B2-G>
- [92] N. Instruments. "Multiplexed vs. Simultaneous Sampling" www.ni.com. [Online]. Available: <https://www.ni.com/docs/en-US/bundle/ni-daqmx/page/multisimulsamp.html>
- [93] IDEX. "NanoTight™ PEEK Headless, Short, 10-32 Coned, for 1/16" OD Single" www.idex-hs.com. [Online]. Available: https://www.idex-hs.com/store/product-detail/nanotight_peek_headless_short_10_32_coned_for_1_16_od_single/f-333n
- [94] ULINE. "Thread Sealing Tape - 1/2 x 520 in" www.uline.ca. [Online]. Available: https://www.uline.ca/Product/Detail/S-14666/Thread-Sealing-Tape/Thread-Sealing-Tape-1-2-x-520?pricode=YG014&gadtype=pla&id=S-14666&gad_source=1&gclid=CjwKCAjw2dG1BhB4EiwA998cqPgJ8r5M94SYY8BXuoYZ44LXyiKeCjqeXQJgWESMdOQJrB_jBZyU3hoCwigQAvD_BwE
- [95] B. A. Finlayson, P. W. Drapala, M. Gebhardt, M. D. Harrison, B. Johnson, M. Lukman, S. Kunaridtipol, T. Plaisted, Z. Tyree, J. Vanburen, and A. Witarasa, *Microcomponent Flow Characterization*. John Wiley Sons, Ltd, 2007, ch. 8, pp. 181–208. [Online]. Available: <https://onlinelibrary.wiley.com/doi/abs/10.1002/9783527610624.ch8>
- [96] P. Oliveira, F. Pinho, and A. Schulte, "A general correlation for the local loss coefficient in newtonian axisymmetric sudden expansions," *International Journal of Heat and Fluid Flow*, vol. 19, no. 6, pp. 655–660, 1998. [Online]. Available: <https://www.sciencedirect.com/science/article/pii/S0142727X98100371>
- [97] R. Adams and C. Essex, *Calculus: A Complete Course*. Pearson, 2013. [Online]. Available: <https://books.google.ca/books?id=5aaEMAEACAAJ>

- [98] G. Casella and R. Berger, *Statistical Inference*, ser. Duxbury advanced series in statistics and decision sciences. Thomson Learning, 2002. [Online]. Available: https://books.google.ca/books?id=0x_vAAAAMAAJ
- [99] C. Wu and M. Hamada, *Experiments: Planning, Analysis, and Optimization*, ser. Wiley Series in Probability and Statistics. Wiley, 2011. [Online]. Available: <https://books.google.ca/books?id=SBgehORJ7hkC>
- [100] K. Ogata, *System Dynamics*, 4th ed. Upper Saddle River, NJ: Prentice Hall, 2004.
- [101] MathWorks. "Transfer function model" www.mathworks.com. [Online]. Available: <https://www.mathworks.com/help/control/ref/tf.html>
- [102] ——. "Bode plot of frequency response, or magnitude and phase data" www.mathworks.com. [Online]. Available: <https://www.mathworks.com/help/control/ref/dynamicsystem.bode.html>
- [103] ——. "Step response of dynamic system" www.mathworks.com. [Online]. Available: <https://www.mathworks.com/help/control/ref/dynamicsystem.step.html>
- [104] ——. "Rise time, settling time, and other step-response characteristics" www.mathworks.com. [Online]. Available: <https://www.mathworks.com/help/control/ref/dynamicsystem.stepinfo.html>
- [105] W. Navidi, *Statistics for Engineers and Scientists*. McGraw-Hill, 2011. [Online]. Available: <https://books.google.ca/books?id=9yA8PwAACAAJ>
- [106] J. Cundiff, *Fluid Power Circuits and Controls: Fundamentals and Applications*, ser. Mechanical and Aerospace Engineering Series. CRC Press, 2001. [Online]. Available: <https://books.google.ca/books?id=TIg2wx6cAYwC>
- [107] P. H. Corporation. "The TexLoc Library: FEP Properties" www.texloc.com. [Online]. Available: http://www.texloc.com/closet/cl_fep_properties.html
- [108] Tef-Cap. "FEP Properties" www.tefcap.com. [Online]. Available: <https://tefcap.com/fep-properties-fluoropolymer-tubing/>
- [109] Zeus. "Material Introduction: PFA Polymer" www.zeusinc.com. [Online]. Available: <https://www.zeusinc.com/wp-content/uploads/2023/03/PFA-Material-V2R1.pdf>

- [110] Saint-Gobain. "Norton ETFE Fluoropolymer Film" www.pronatindustries.com. [Online]. Available: <https://pronatindustries.com/wp-content/uploads/2015/03/Norton-ETFE.pdf>
- [111] L. Polymer Plastics Company. "Data Sheet: PEEK" www.polymerplastics.com. [Online]. Available: <https://www.polymerplastics.com/images/dataSheets/DSPEEK.pdf>
- [112] DuPont. "Product and Properties Handbook: Teflon FEP fluoropolymer resin" www.rjchase.com. [Online]. Available: http://rjchase.com/teflon_information.htm
- [113] F. White, *Viscous Fluid Flow*, ser. McGraw-Hill series in mechanical engineering. McGraw-Hill, 1991. [Online]. Available: <https://books.google.ca/books?id=G6IeAQAIAAJ>
- [114] R. Hawkes, J. Iqbal, F. Mansour, M. Milner-Bolotin, and P. Williams, *Physics for Scientists and Engineers*. Nelson Education Limited, 2018. [Online]. Available: <https://books.google.ca/books?id=KjKCAQAACAAJ>
- [115] K. A. Remley, R. J. Pirkl, C.-M. Wang, D. Senić, A. C. Homer, M. V. North, M. G. Becker, R. D. Horansky, and C. L. Holloway, "Estimating and correcting the device-under-test transfer function in loaded reverberation chambers for over-the-air tests," *IEEE Transactions on Electromagnetic Compatibility*, vol. 59, no. 6, pp. 1724–1734, 2017.
- [116] R. A. Bentler and C. V. Pavlovic, "Transfer functions and correction factors used in hearing aid evaluation and research," *Ear and Hearing*, vol. 10, no. 1, 1989. [Online]. Available: https://journals.lww.com/ear-hearing/fulltext/1989/02000/transfer_functions_and_correction_factors_used_in.10.aspx
- [117] IDEX. "Plug Delrin® - 10-32 Coned Black" www.idex-hs.com. [Online]. Available: https://www.idex-hs.com/store/product-detail/plug_delrin_10_32_coned_black/u-467blk
- [118] McMaster-Carr. "Plastic Quick-Turn Tube Couplings for Air and Water" www.mcmaster.com. [Online]. Available: <https://www.mcmaster.com/products/plastic-quick-turn-tube-fittings/>
- [119] D. Lay, *Linear Algebra and Its Applications*. Pearson Education, 2003. [Online]. Available: <https://books.google.ca/books?id=v8Zls26Y0wkC>

APPENDICES

Appendix A

Dimensional Analysis

Within this appendix is the derivation of the dimensionless parameters presented in Section 3.1.4.

Considering the analytical representation of the frequency response (FR) of the pressure transient dynamics across the sample tubing as

$$G_p(j\omega) = |G_p(j\omega)|\angle G_p(j\omega) \quad (\text{A.1})$$

From Section 3.1.3, it was concluded that

$$G_p(j\omega) \sim f(D_i, L, E, \mu, P_{\text{off}}, P_A, \omega) \quad (\text{A.2})$$

Listing the primary dimensions of each variable in terms of $ML_{\text{dim}}T\theta$ [73] gives

Table A.1: Primary dimensions of variables

Variables	$G_p(j\omega)$	D_i	L	E, P_{off}, P_A	μ	ω
Primary Dimension	none	L_{dim}	L_{dim}	$ML_{\text{dim}}^{-1}T^{-2}$	$ML_{\text{dim}}^{-1}T^{-1}$	T^{-1}

Selecting μ , D_i , and P_{off} as the scaling parameters since they are unable to form a dimensionless Π group, and are the easiest parameters to keep constant in the practical implementation of the experiments, results in the following Π groups:

Dimensionless Frequency (Π_1)

$$\Pi_1 = \mu^a D_i^b P_{\text{off}}^c \omega = (ML_{\text{dim}}^{-1} T^{-1})^a (L_{\text{dim}})^b (ML_{\text{dim}}^{-1} T^{-2})^c (T^{-1}) = M^0 L_{\text{dim}}^0 T^0 \quad (\text{A.3})$$

From equating exponents and performing algebra, it can be shown that $a = 1$, $b = 0$, $c = -1$, which results in

$$\Pi_1 = \frac{\omega \mu}{P_{\text{off}}} \quad (\text{A.4})$$

This is verified as

$$\Pi_1 = \frac{\omega \mu}{P_{\text{off}}} = \frac{(T^{-1})(ML_{\text{dim}}^{-1} T^{-1})}{(ML_{\text{dim}}^{-1} T^{-2})} = 1$$

Dimensionless Pressure Amplitude (Π_2)

$$\Pi_2 = \mu^a D_i^b P_{\text{off}}^c P_A = (ML_{\text{dim}}^{-1} T^{-1})^a (L_{\text{dim}})^b (ML_{\text{dim}}^{-1} T^{-2})^c (ML_{\text{dim}}^{-1} T^{-2}) = M^0 L_{\text{dim}}^0 T^0 \quad (\text{A.5})$$

From equating exponents and performing algebra, it can be shown that $a = 0$, $b = 0$, $c = -1$, which results in

$$\Pi_2 = \frac{P_A}{P_{\text{off}}} \quad (\text{A.6})$$

This is verified as

$$\Pi_2 = \frac{P_A}{P_{\text{off}}} = \frac{ML_{\text{dim}}^{-1} T^{-2}}{ML_{\text{dim}}^{-1} T^{-2}} = 1$$

Dimensionless Length (Π_3)

$$\Pi_3 = \mu^a D_i^b P_{\text{off}}^c L = (ML_{\text{dim}}^{-1} T^{-1})^a (L_{\text{dim}})^b (ML_{\text{dim}}^{-1} T^{-2})^c (L_{\text{dim}}) = M^0 L_{\text{dim}}^0 T^0 \quad (\text{A.7})$$

From equating exponents and performing algebra, it can be shown that $a = 0$, $b = -1$, $c = 0$, which results in

$$\Pi_3 = \frac{L}{D_i} \quad (\text{A.8})$$

This is verified as

$$\Pi_3 = \frac{L}{D_i} = \frac{L_{\text{dim}}}{L_{\text{dim}}} = 1$$

Dimensionless Material Stiffness (Π_4)

$$\Pi_4 = \mu^a D_i^b P_{\text{off}}^c E = (ML_{\text{dim}}^{-1}T^{-1})^a (L_{\text{dim}})^b (ML_{\text{dim}}^{-1}T^{-2})^c (ML_{\text{dim}}^{-1}T^{-2}) = M^0 L_{\text{dim}}^0 T^0 \quad (\text{A.9})$$

From equating exponents and performing algebra, it can be shown that $a = 0$, $b = 0$, $c = -1$, which results in

$$\Pi_4 = \frac{E}{P_{\text{off}}} \quad (\text{A.10})$$

This is verified as

$$\Pi_4 = \frac{E}{P_{\text{off}}} = \frac{ML_{\text{dim}}^{-1}T^{-2}}{ML_{\text{dim}}^{-1}T^{-2}} = 1$$

From the dimensionless parameters given by (A.4), (A.6), (A.8), and (A.10), the dimensionless form of (A.2) is given by

$$G_p(j\omega) \sim f\left(\frac{\omega\mu}{P_{\text{off}}}, \frac{P_A}{P_{\text{off}}}, \frac{L}{D_i}, \frac{E}{P_{\text{off}}}\right) \quad (\text{A.11})$$

This concludes this appendix detailing the derivation of the dimensionless parameters presented in Section 3.1.4.

Appendix B

Measurement System Characterization

In this appendix, the characterization of the measurement setup is presented. The static calibration of the pressure sensors is outlined in Section B.1 and the dynamic characterization of the pressure sensor junction setup is presented in Section B.2. Uncertainty in the measurements and estimated/calculated parameters was determined at a 95% confidence level using standard propagation of uncertainty techniques [65, 105]

B.1 Pressure Sensor Static Calibration

For the calibration of the TE Connectivity U536D-H000015-001BG pressure sensors [77] to relate the measured voltage to a pressure, the experimental setup detailed in Figure B.1 was used. The pressure sensor to be calibrated was attached to a machined pressure sensor junction, see Section 3.2.3 and Appendix C, with the outlet of the junction plugged (IDEX U-667BLK [117]) and the inlet connected to air tubing (SG-Tygon LMT-55, 1.30 mm ID, 65 mm length [75]) with a 10-32 coned male fitting (McMaster-Carr Plastic Quick-Turn Tube Coupling for 1/16" Tube ID, Nylon 51525K121 [118]). The inlet of the air tubing was connected to an air pressure pump (MFCS-EZ [0-1 bar] [74]) which was used to set the steady-state pressure. The analog voltage signal from the pressure sensor at a given steady-state pressure was sampled at a rate of 1kHz for 10 seconds using a data acquisition system (DAQ) (NI USB-6003 [78]) and computer setup with LabVIEW.

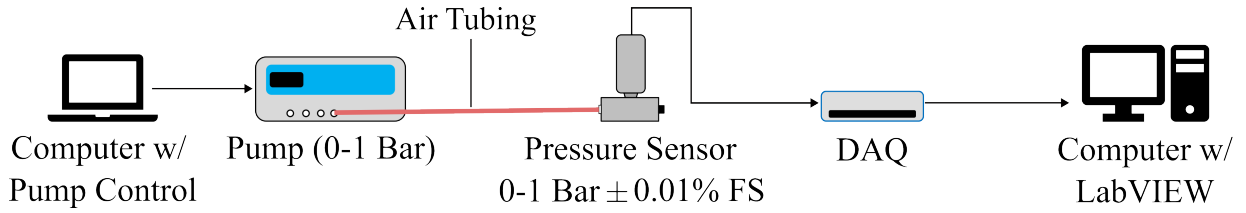


Figure B.1: Apparatus used to calibrate pressure sensors.

The sensors were calibrated over their entire input range, that being 0 to 1000 mbar. The pressure calibration curve was linear for both sensors, see Figures B.2 and B.3. From ordinary least squares (OLS) fits of the data the linear calibration equations were obtained, where the calibration equations for the pressure sensors are given as

$$P_{\text{cal}_1}[\text{mbar}] = (201.09)V[V] - 1.9532[\text{mbar}] \quad (\text{B.1})$$

for PS_1 , and

$$P_{\text{cal}_2}[\text{mbar}] = (200.75)V[V] - 1.3837[\text{mbar}] \quad (\text{B.2})$$

for PS_2 . Note that PS_1 is the sensor that was used at the inlet of the sample tubing and PS_2 was the sensor that was used at the outlet of the sample tubing in the experiments to determine the frequency response of the pressure transient dynamics across the sample tubing.

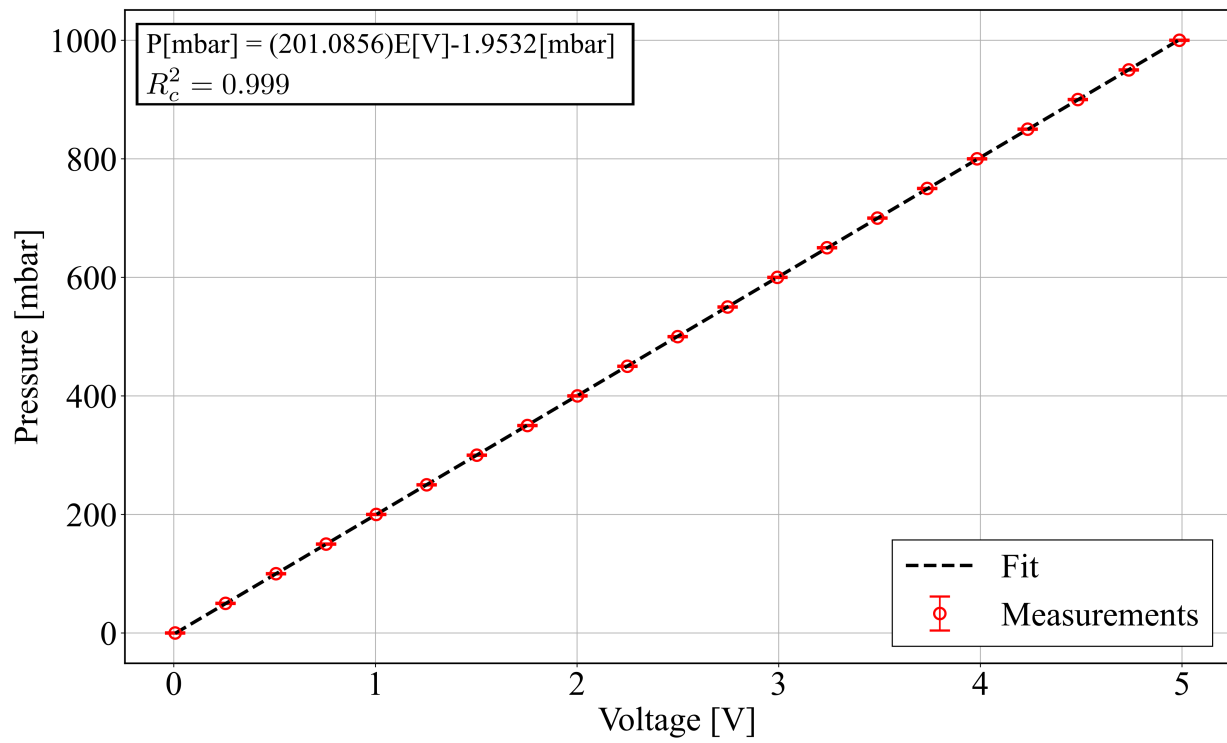


Figure B.2: Calibration plot of PS_1 with OLS fit.

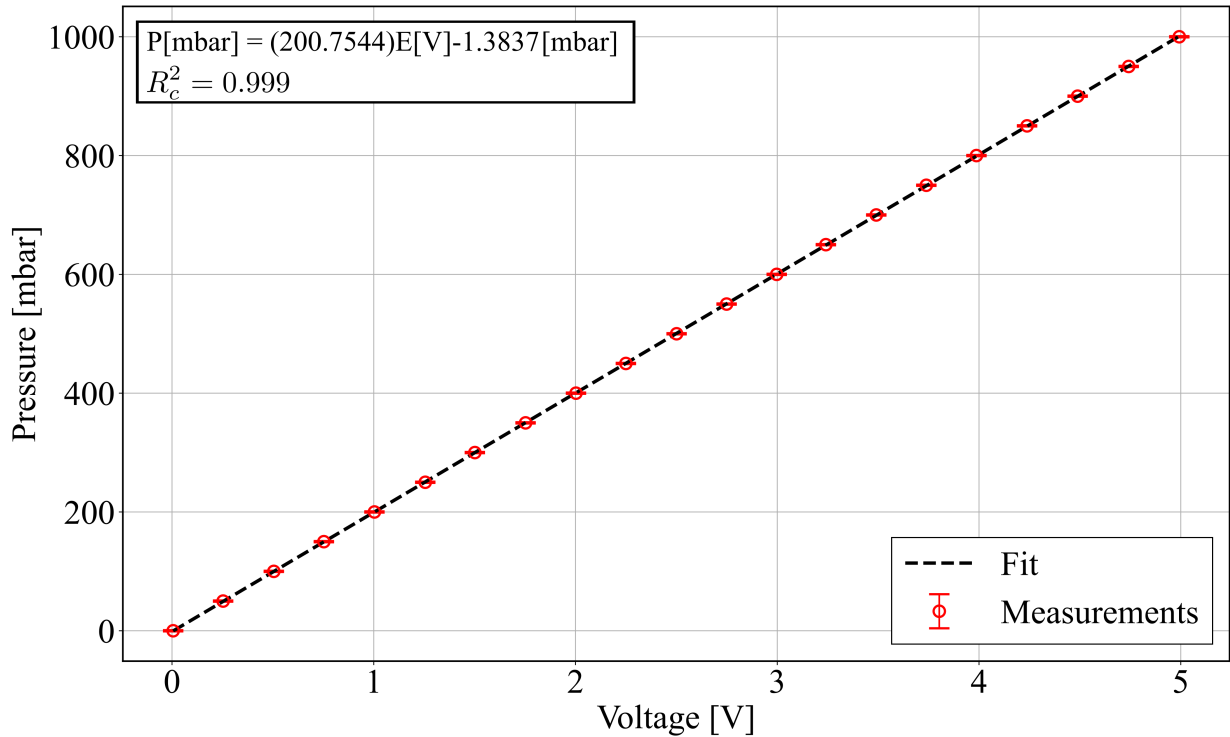


Figure B.3: Calibration plot of PS_2 with OLS fit.

B.2 Dynamic Characterization of Pressure Sensor Setup

Since the pressure sensor setup was used to obtain dynamic measurements, it was important to experimentally characterize the effect that this setup would have on the frequency response (FR) measurements of the pressure transient dynamics across the sample tubing in the pressure-driven droplet microfluidic control system (PDMFCS) [64, 68]. To assess the pressure sensor setup dynamics, a step response of the pressure sensor setup was obtained by using the experimental apparatus detailed in Figure B.4. The junction inlet was connected to air tubing (SG-Tygon LMT-55, 1.30 mm ID, 115 mm length [75]) with a 10-32 coned male fitting (McMaster-Carr Plastic Quick-Turn Tube Coupling for 1/16" Tube ID, Nylon 51525K121 [118]). The inlet of the air tubing was connected to an air pressure pump (MFCS-EZ [0-1 bar] [74]) which was used to set the steady-state pressure. Attached to the outlet of the junction was an IDEX F-333NX fitting [93] covered by a balloon. To obtain the step response, the pump was set to a steady-state pressure, then

once a constant pressure was noted in the sensor setup, the balloon was popped using a scalpel. This type of test is suitable for characterizing systems with natural frequencies ≤ 1000 Hz (6283 rad/s) [68]. The analog voltage signal from the pressure sensor was sampled, before the balloon was popped up until the step response reached steady-state, at a rate of 10kHz using a DAQ (NI USB-6003 [78]) and computer setup with LabVIEW.

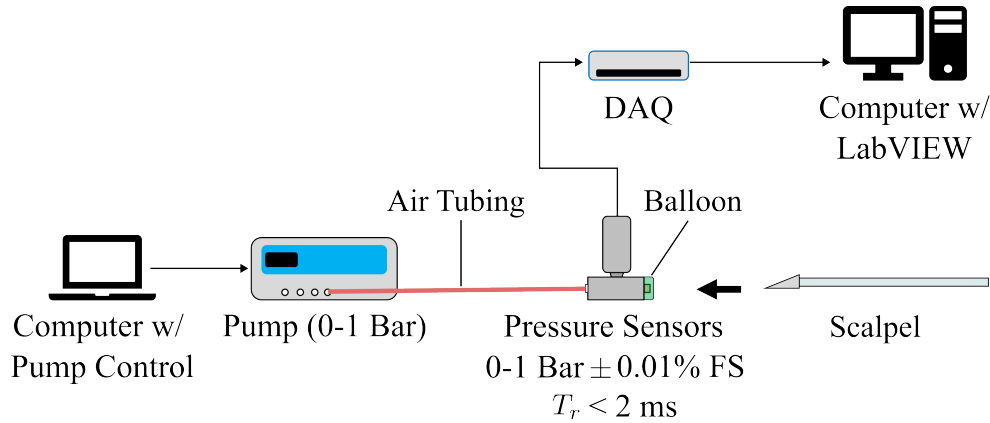


Figure B.4: Apparatus used to dynamically characterize pressure sensor setup.

Tests were performed at 25, 50, 100, 200, and 250 mbar. The step response could be approximated from the time-domain data as a general second-order system, which is in agreement with prior pressure transient line models [64, 65, 68]. The damping ratio was estimated from the percent overshoot and the natural frequency was estimated from the estimate of the damping ratio and the determination of the rise time of the response [49]. Approximating the response as second-order showed reasonable fits to the data as can be seen in Figure B.5 below. Note that the average error between the measured and modelled output was calculated using root-mean square error (RMSE).

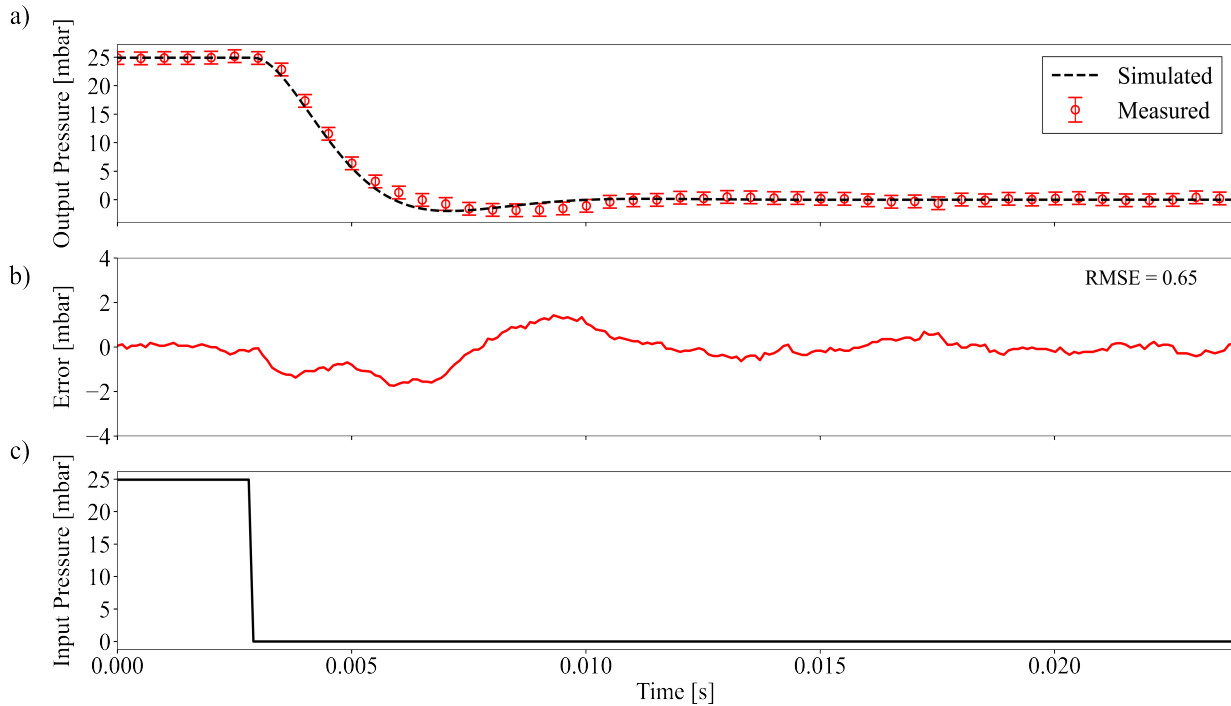


Figure B.5: a) Response of second-order model overlapped with experimental time-domain step response data for an input pressure of 25 mbar, every 5th point shown for clarity, b) Error between simulated output and measured output at each time step, c) Input step signal.

Increasing the pressure at which the step response was taken resulted in a decrease in the natural frequency and an increase of the damping ratio, see Table B.2. However, for all pressures tested, the natural frequency was much greater than the frequency range over which the pressure transient dynamics across the sample tubing are characterized [0.06, 2.5] rad/s, see Figure B.6. Thus, it can be concluded that the pressure sensor setup will not significantly attenuate or phase shift the pressure waves for the experimental FR measurements of the pressure transient dynamics across the sample tubing, assuming minor losses due to the junction-tubing connections are kept to a minimum. If this requirement is met, any attenuation or phase shift noted in the main FR experiments will be primarily due to the tubing and fluid properties.

Table B.1: Natural frequency, ω_n , and damping ratio, ζ , of pressure sensor setup second-order model with increasing pressure.

P_{step} [mbar]	ω_n [rad/s]	ζ [unitless]
25 ± 0.3	964 ± 158	0.63 ± 0.08
50 ± 0.3	783 ± 73	0.70 ± 0.05
100 ± 0.3	633 ± 47	0.78 ± 0.04
200 ± 0.3	510 ± 33	0.87 ± 0.05
250 ± 0.3	473 ± 48	0.93 ± 0.18

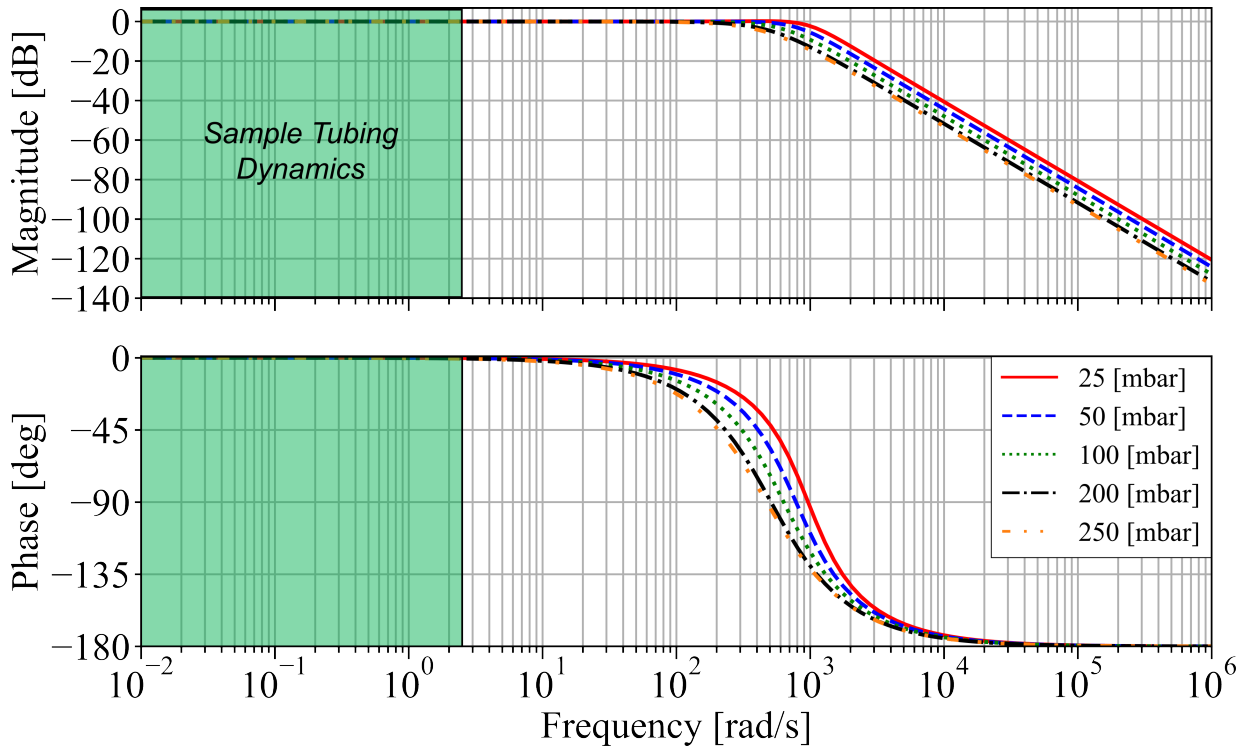


Figure B.6: Estimated FR for pressure measurement setup for increasing pressure, frequency region over which pressure transient dynamics across sample tubing is characterized highlighted in green.

This concludes this appendix detailing the static calibration and dynamic characterization of the measurement system.

Appendix C

Pressure Junction Drawings

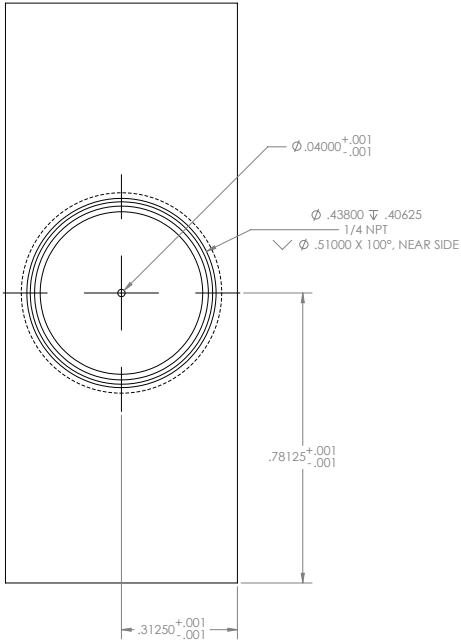
This appendix presents the detailed drawings used to manufacture the pressure sensor junctions to employ the experimental methodology outlined in Chapter 3 for the experimental characterization of pressure transient dynamics across sample tubing in the pressure-driven droplet microfluidic feedback control system. IDEX F-333N fittings for 1/16 in OD tubing [93] were used to connect the sample tubing to the junctions. As such, the technical drawing for the bore hole for these fittings is also needed. This information can be obtained from IDEX technical support, but cannot be reprinted in this thesis.

4

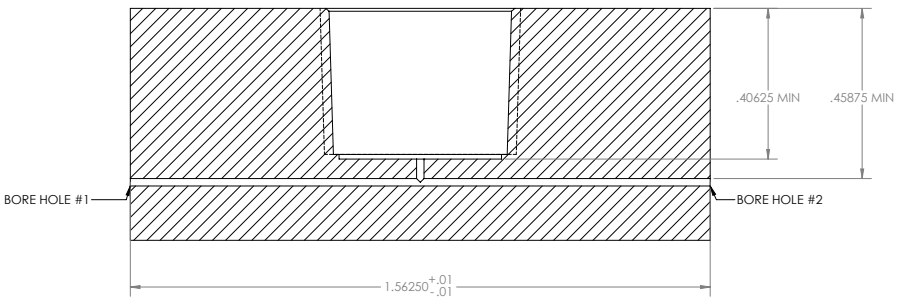
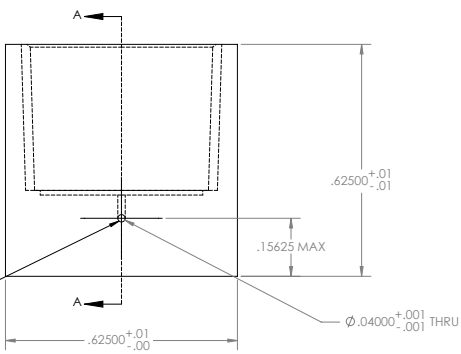
3

2

1



NOTE: LOCATION OF BORE HOLE FOR FITTING. HOLE TO BE CONCENTRIC WITH 0.04 IN THRU HOLE. BORE HOLE TO BE PLACED ON BOTH FRONT AND BACK FACE. SEE TECHNICAL DRAWING FROM IDEX FOR HOLE SPECIFICATION.



SECTION A-A

UNLESS OTHERWISE SPECIFIED: DIMENSIONS ARE IN INCHES				DO NOT SCALE DRAWING	REVISION
NAME	DATE	MATERIAL	TITLE		
DRAWN DYLAN HAHN	01/16/23	316 SS	JUNCTION (REV1)		
WEIGHT			SCALE: 1:1	SHEET 1 OF 1	

4

3

2

1

D

C

B

A

C

This concludes this appendix detailing the technical drawings for the pressure sensor junctions.

Appendix D

Data Analysis Code

The Python and MATLAB scripts used to automate the data selection, curve fitting, frequency response, and uncertainty analysis can be found at the following link:

`https://github.com/d2hahn/FR_analysis.git`

This concludes this appendix detailing the location of the data analysis code.

Appendix E

Hydrodynamic Equivalent Circuit Model Transfer Function Derivation

This appendix presents the derivation of the hydrodynamic equivalent circuit model (HECM) transfer functions (TFs) for the symmetric (Section 3.4.1), second-order, and first-order (Section 3.4.4), model forms. Derivations were performed using the Laplace domain impedances [49] for the circuit components with Kirchoff's voltage (KVL) and current laws (KCL).

E.1 Symmetric HECM

Considering the symmetric form of the HECM presented in below Figure E.1

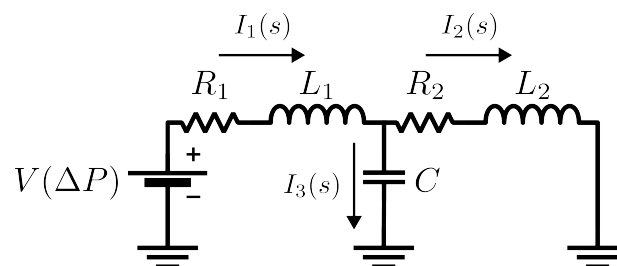


Figure E.1: Symmetric HECM.

Applying KCL gives

$$I_3(s) = I_1(s) - I_2(s) \quad (\text{E.1})$$

Recalling that in the symmetric HECM $R_1 = R_2 = \frac{R}{2}$ and $L_1 = L_2 = \frac{L_{\text{hyd}}}{2}$, if loop 1 and loop 2 for the circuit are designated as in Figure E.2 below

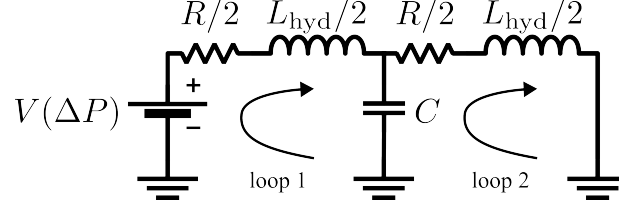


Figure E.2: KVL loops for symmetric HECM.

Applying KVL to loop 1 gives

$$-V(s) + \frac{R}{2}I_1(s) + \frac{L_{\text{hyd}}}{2}sI_1(s) + \frac{1}{C_s}(I_1(s) - I_2(s)) = 0$$

which can be simplified to

$$\left(\frac{L_{\text{hyd}}}{2}s + \frac{R}{2} + \frac{1}{C_s}\right)I_1(s) - \frac{1}{C_s}I_2(s) = V(s) \quad (\text{E.2})$$

Similarly, applying KVL to loop 2 gives

$$-\frac{1}{C_s}I_1(s) + \left(\frac{L_{\text{hyd}}}{2}s + \frac{R}{2} + \frac{1}{C_s}\right)I_2(s) = 0 \quad (\text{E.3})$$

Applying Cramer's rule [119] to solve for $I_1(s)$ and $I_2(s)$ gives

$$I_1(s) = \frac{2V(s)(CL_{\text{hyd}}s^2 + CRs + 2)}{(L_{\text{hyd}}s + R)(CL_{\text{hyd}}s^2 + CRs + 4)} \quad (\text{E.4})$$

and

$$I_2(s) = \frac{4V(s)}{(L_{\text{hyd}}s + R)(CL_{\text{hyd}}s^2 + CRs + 4)} \quad (\text{E.5})$$

Substituting (E.4) and (E.5) into (E.1) gives

$$I_3(s) = \frac{2V(s)(CL_{\text{hyd}}s^2 + CRs)}{(L_{\text{hyd}}s + R)(CL_{\text{hyd}}s^2 + CRs + 4)} \quad (\text{E.6})$$

From Laplace domain impedance, $Z(s) = \frac{V(s)}{I(s)}$, voltage across the symmetric HECM components is given by

$$V_{R_1}(s) = \frac{R}{2}I_1(s) \quad (\text{E.7})$$

$$V_{R_2}(s) = \frac{R}{2}I_2(s) \quad (\text{E.8})$$

$$V_{L_1}(s) = \frac{L_{\text{hyd}}}{2}sI_1(s) \quad (\text{E.9})$$

$$V_{L_2}(s) = \frac{L_{\text{hyd}}}{2}sI_2(s) \quad (\text{E.10})$$

$$V_C(s) = \frac{1}{C_s}I_3(s) \quad (\text{E.11})$$

Subbing (E.4) into (E.7) and (E.9), and dividing both sides by $V(s)$ gives the voltage TF for R_1

$$G_{R_1}(s) = \frac{V_{R_1}(s)}{V(s)} = \frac{R(CL_{\text{hyd}}s^2 + CRs + 2)}{(L_{\text{hyd}}s + R)(CL_{\text{hyd}}s^2 + CRs + 4)} \quad (\text{E.12})$$

and L_1

$$G_{L_1}(s) = \frac{V_{L_1}(s)}{V(s)} = \frac{L_{\text{hyd}}s(CL_{\text{hyd}}s^2 + CRs + 2)}{(L_{\text{hyd}}s + R)(CL_{\text{hyd}}s^2 + CRs + 4)} \quad (\text{E.13})$$

Subbing (E.5) into (E.8) and (E.10), and dividing both sides by $V(s)$ gives the voltage TF for R_2

$$G_{R_2}(s) = \frac{V_{R_2}(s)}{V(s)} = \frac{2R}{(L_{\text{hyd}}s + R)(CL_{\text{hyd}}s^2 + CRs + 4)} \quad (\text{E.14})$$

and L_2

$$G_{L_2}(s) = \frac{V_{L_2}(s)}{V(s)} = \frac{2L_{\text{hyd}}s}{(L_{\text{hyd}}s + R)(CL_{\text{hyd}}s^2 + CRs + 4)} \quad (\text{E.15})$$

Subbing (E.6) into (E.11) and dividing by $V(s)$ gives the voltage TF across C

$$G_C(s) = \frac{V_C(s)}{V(s)} = \frac{2}{CL_{\text{hyd}}s^2 + CRs + 4} \quad (\text{E.16})$$

This concludes the derivation of the voltage TFs across the components of the symmetric HECM.

E.2 Second-Order HECM

Considering the second-order HECM in Figure E.3 below

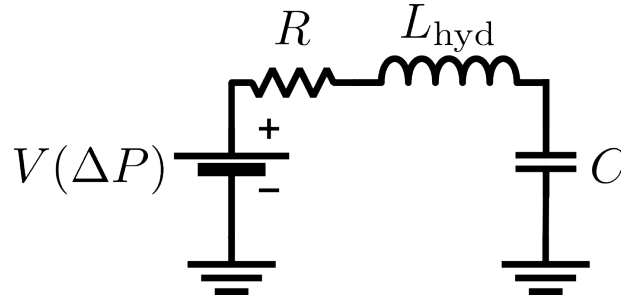


Figure E.3: Second-order HECM.

Applying KVL in the counterclockwise direction gives

$$-V(s) + RI(s) + L_{\text{hyd}}sI(s) + \frac{1}{Cs}I(s) = 0 \quad (\text{E.17})$$

Solving for $I(s)$ and multiplying by $\frac{s}{s}$ gives

$$I(s) = \frac{sV(s)}{L_{\text{hyd}}s^2 + Rs + \frac{1}{C}} \quad (\text{E.18})$$

In Laplace domain, voltage across the HECM components is given by

$$V_R(s) = RI(s) \quad (\text{E.19})$$

$$V_L(s) = L_{\text{hyd}}sI(s) \quad (\text{E.20})$$

$$V_C(s) = \frac{1}{Cs}I(s) \quad (\text{E.21})$$

Subbing (E.18) into (E.19), (E.20), and (E.21) and simplifying the resulting equations gives the TFs across the circuit components of the second-order HECM as

$$G_R(s) = \frac{V_R(s)}{V(s)} = \frac{RCs}{L_{\text{hyd}}Cs^2 + RCs + 1} = \frac{\frac{R}{L_{\text{hyd}}}s}{s^2 + \frac{R}{L_{\text{hyd}}}s + \frac{1}{L_{\text{hyd}}C}} \quad (\text{E.22})$$

$$G_L(s) = \frac{V_L(s)}{V(s)} = \frac{L_{\text{hyd}}Cs^2}{L_{\text{hyd}}Cs^2 + RCs + 1} = \frac{s^2}{s^2 + \frac{R}{L_{\text{hyd}}}s + \frac{1}{L_{\text{hyd}}C}} \quad (\text{E.23})$$

$$G_C(s) = \frac{V_C(s)}{V(s)} = \frac{1}{L_{\text{hyd}}Cs^2 + RCs + 1} = \frac{\frac{1}{L_{\text{hyd}}C}}{s^2 + \frac{R}{L_{\text{hyd}}}s + \frac{1}{L_{\text{hyd}}C}} \quad (\text{E.24})$$

This concludes the derivation of the voltage TFs across the components of the second-order HECM.

E.3 First-Order HECM

E.3.1 RC Circuit

Considering the first-order RC HECM in Figure E.4 below

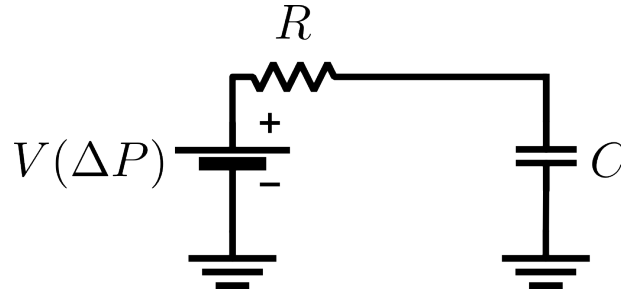


Figure E.4: First-order RC HECM.

Applying KVL in counterclockwise direction gives

$$-V(s) + RI(s) + \frac{1}{C_s}I(s) = 0 \quad (\text{E.25})$$

Rearranging (E.25) for $I(s)$ gives

$$I(s) = \frac{V(s)}{\frac{1}{C_s} + R} \quad (\text{E.26})$$

Subbing (E.26) into (E.19) and (E.21) and simplifying the resulting equations gives the TFs across the circuit components of the first-order RC HECM as

$$G_R(s) = \frac{V_R(s)}{V(s)} = \frac{RCs}{1 + RCs} \quad (\text{E.27})$$

$$G_C(s) = \frac{V_C(s)}{V(s)} = \frac{1}{1 + RCs} \quad (\text{E.28})$$

This concludes the derivation of the voltage TFs across the components of the first-order RC HECM.

E.3.2 RL Circuit

Considering the first-order RL HECM in Figure E.5 below

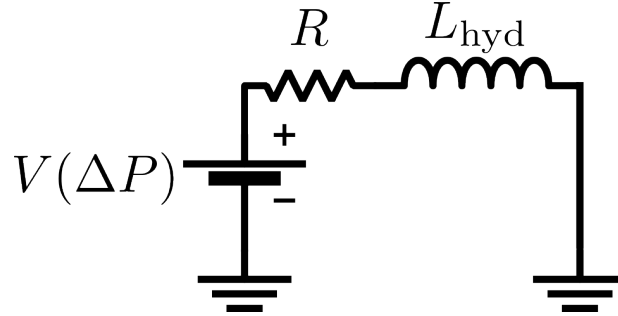


Figure E.5: First-order RL HECM.

Applying KVL in counterclockwise direction gives

$$-V(s) + RI(s) + L_{\text{hyd}}sI(s) = 0 \quad (\text{E.29})$$

Rearranging (E.29) for $I(s)$ gives

$$I(s) = \frac{V(s)}{L_{\text{hyd}}s + R} \quad (\text{E.30})$$

Subbing (E.30) into (E.19) and (E.20) and simplifying the resulting equations gives the TFs across the circuit components of the first-order RC HECM as

$$G_R(s) = \frac{V_R(s)}{V(s)} = \frac{1}{1 + \frac{L_{\text{hyd}}}{R}s} \quad (\text{E.31})$$

$$G_L(s) = \frac{V_L(s)}{V(s)} = \frac{\frac{L_{\text{hyd}}}{R}s}{1 + \frac{L_{\text{hyd}}}{R}s} \quad (\text{E.32})$$

This concludes the derivation of the voltage TFs across the components of the first-order RL HECM, and this appendix detailing the TF derivations for the various forms of the HECM.

Appendix F

Supplementary Results

Within this appendix is the supplementary results for the experimental data presented in Section 4.2. Specifically, the Bode plots showing all experimental and estimated frequency responses (FRs), as well as the step response plots for each test within a given experimental case are provided. These were omitted from the main body of the report as they are visually cluttered and do not add anything to the discussion. Also, the tabulated values for the non-dimensional parameters in the $\frac{L}{D_i}$ experimental case are provided. Data is organized in same order as Section 4.2.

F.1 Increasing Pressure Offset

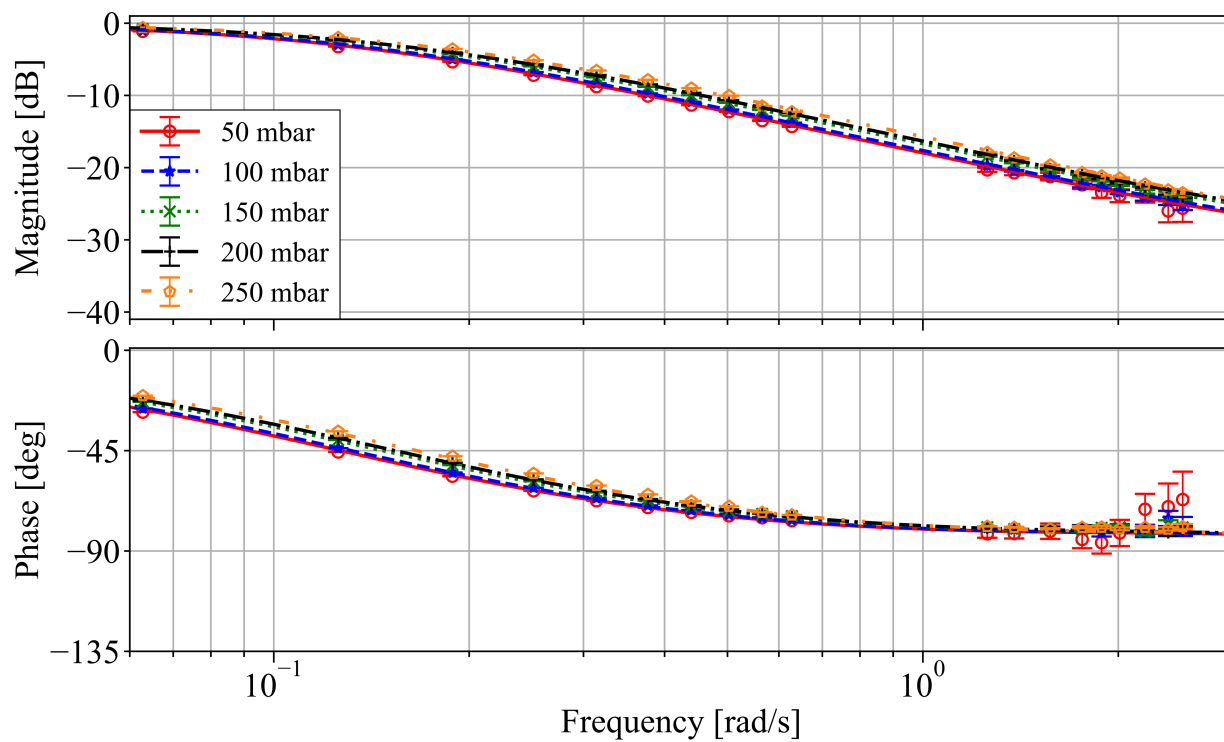


Figure F.1: Experimental (points) and estimated (lines) FR for increasing P_{off} .

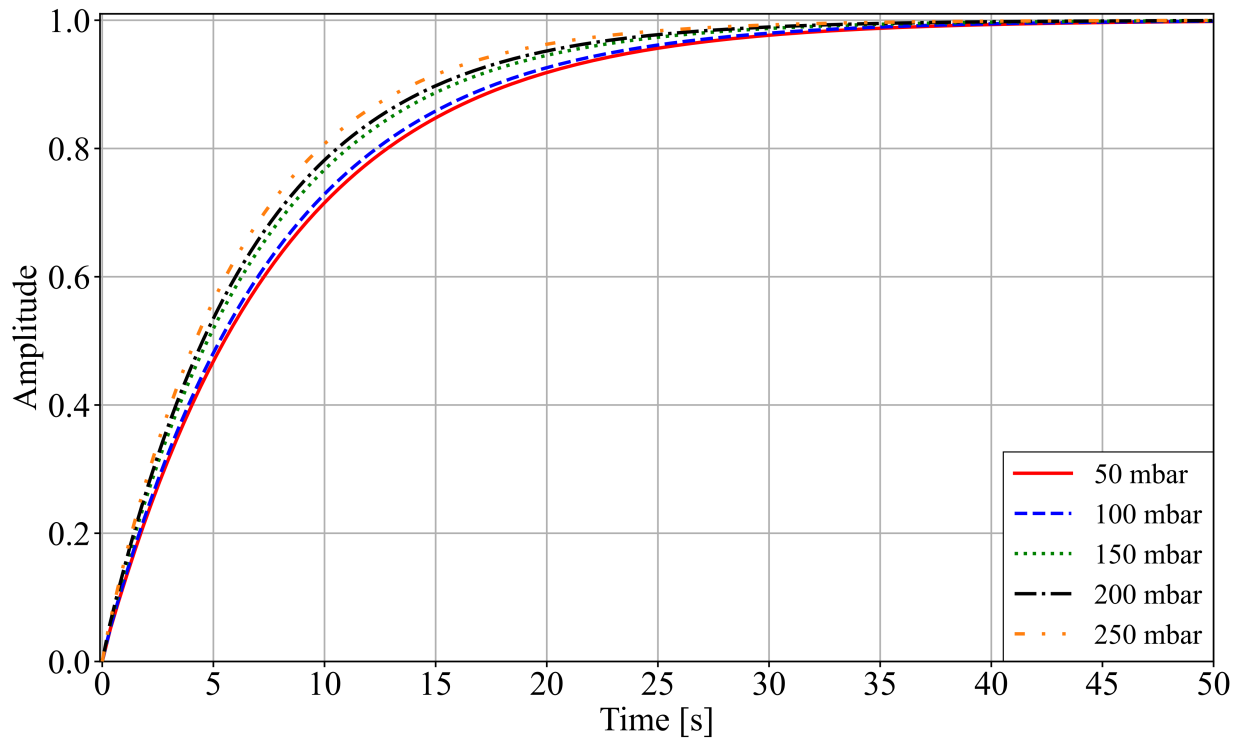


Figure F.2: Simulated step responses for estimated TF from experimental FR for increasing P_{off} .

F.2 Increasing Length-Diameter Ratio

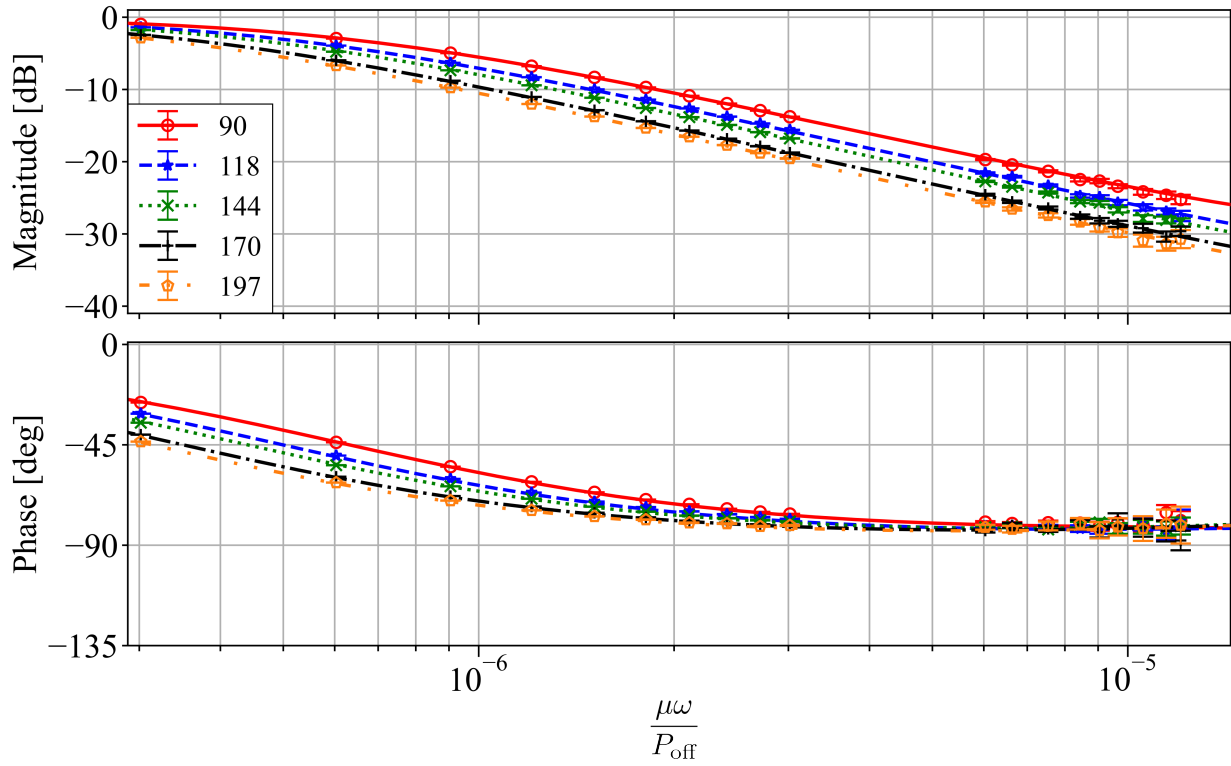


Figure F.3: Experimental (points) and estimated (lines) FR for increasing $\frac{L}{D_i}$.

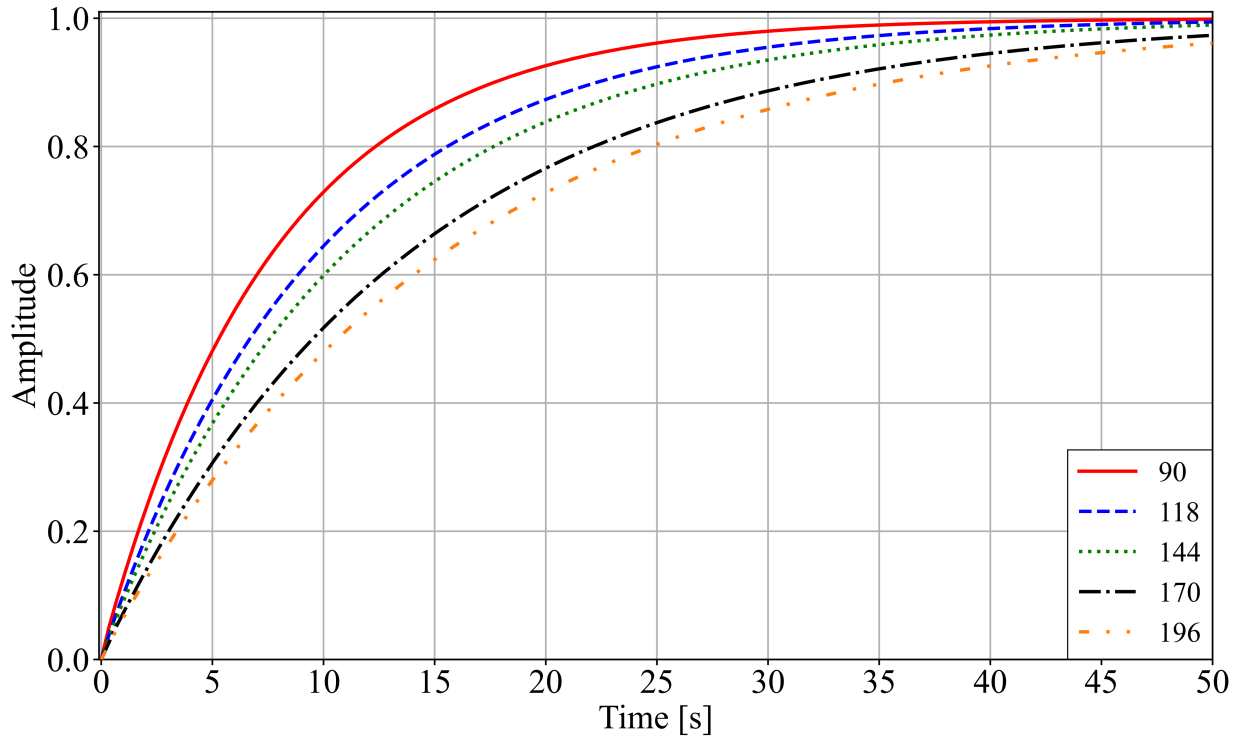


Figure F.4: Simulated step responses for estimated TF from experimental FR for increasing $\frac{L}{D_i}$.

Table F.1: Parameters for estimated TF's from dimensionless experimental FR's investigating the effect of varying $\frac{L}{D_i}$. Note that absolute uncertainties are given.

$\frac{L}{D_i}$	$\frac{P_{\text{off}}}{\mu} a \cdot 10^4$	$\frac{P_{\text{off}}}{\mu} b \cdot 10^6$	$\frac{P_{\text{off}}}{\mu} d \cdot 10^4$
90	4.2 ± 0.8	1.60 ± 0.02	3.1 ± 0.7
118	2.9 ± 0.5	2.02 ± 0.02	2.1 ± 0.2
144	2.7 ± 0.6	2.29 ± 0.01	1.7 ± 0.1
170	2.7 ± 0.1	2.88 ± 0.02	1.7 ± 0.1
197	2.7 ± 0.5	3.21 ± 0.02	1.7 ± 0.3

F.3 Increasing Fluid Viscosity

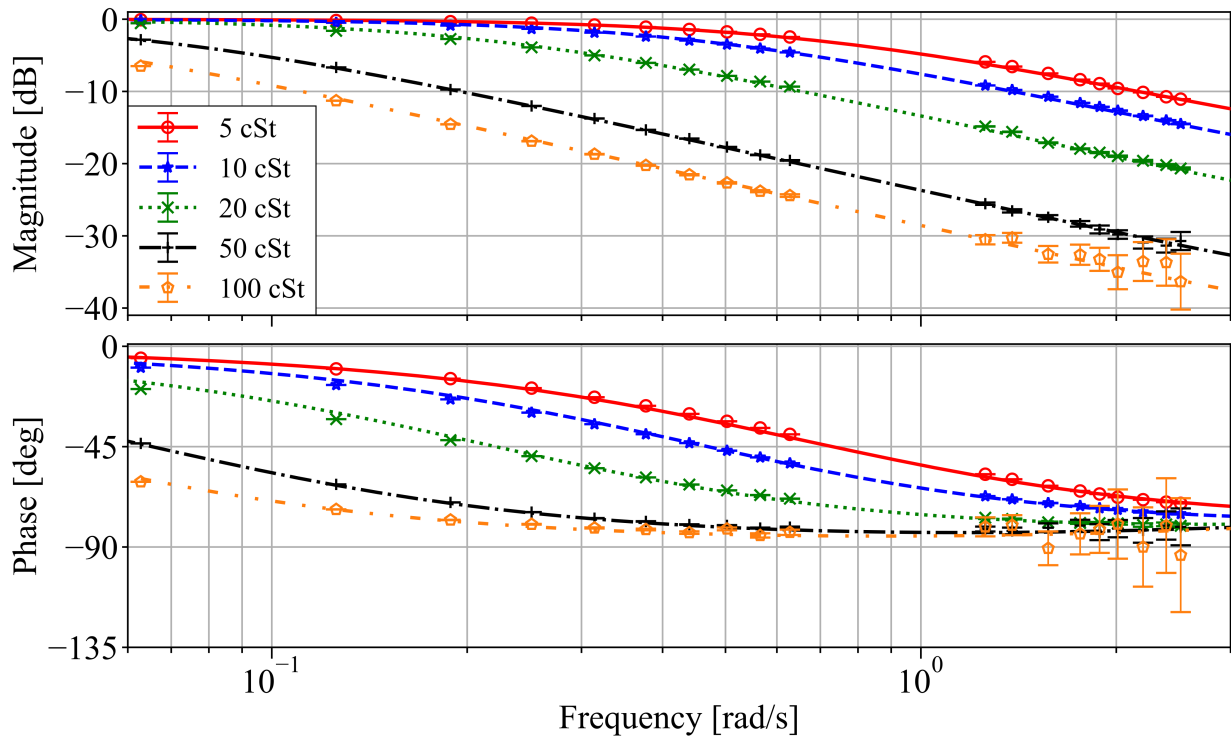


Figure F.5: Experimental (points) and estimated (lines) FR for increasing ν .

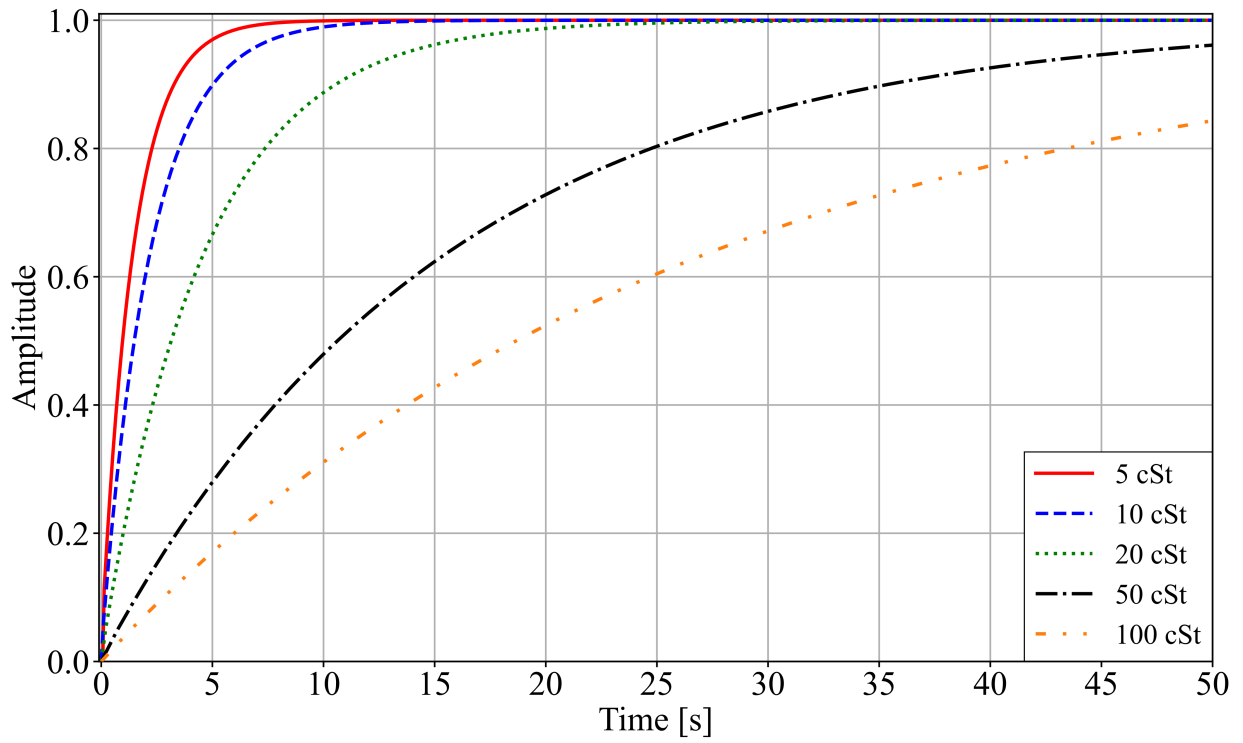


Figure F.6: Simulated step responses for estimated TF from experimental FR for increasing ν .

F.4 Increasing Tubing Material Stiffness

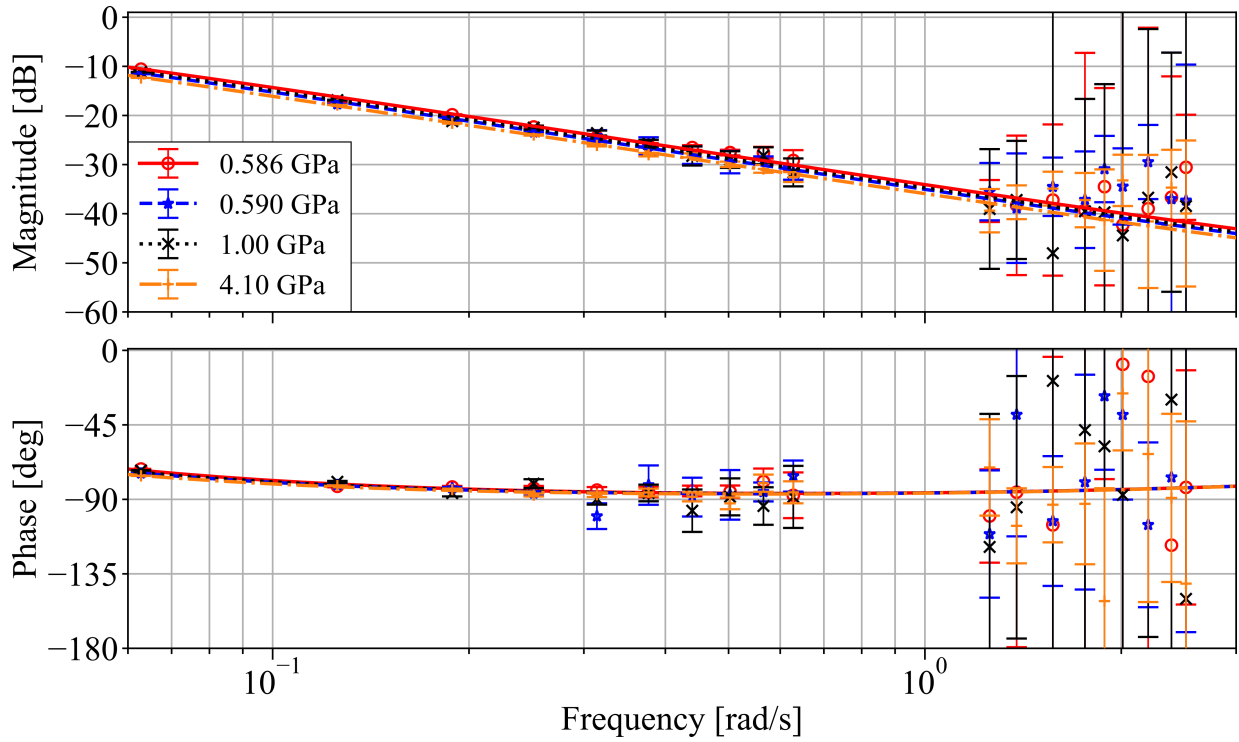


Figure F.7: Experimental (points) and estimated (lines) FR for increasing E_{flex} .

This concludes this appendix detailing the supplemental experimental results.